AD-A134 101 HIGH RESOLUTION 3-D TOMOGRAPHIC IMAGING BY WAVELENGTH 1/2
AND POLARIZATION DI..(U) MOORE SCHOOL OF ELECTRICAL
ENGINEERING PHILADELPHIA PA ELECTR.. N H FARHAT
UNCLASSIFIED 05 JUL 83 EO/MO-6 AFOSR-TR-83-0797 F/G 14/5 NL

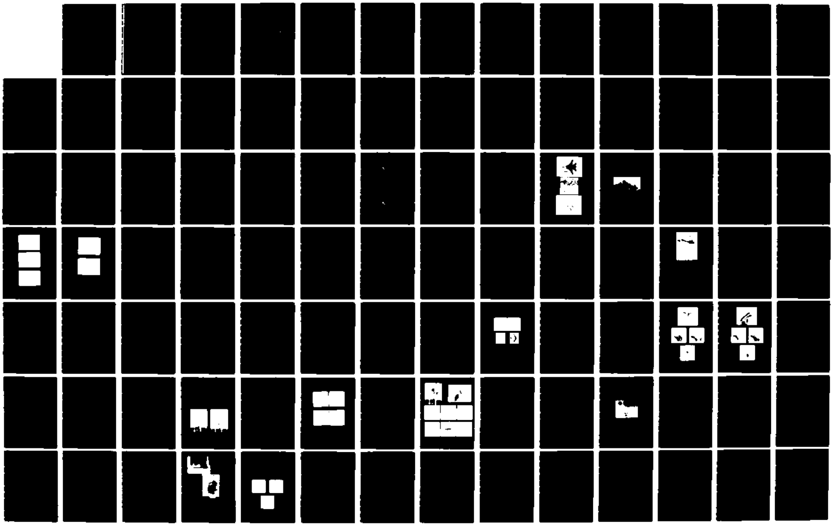

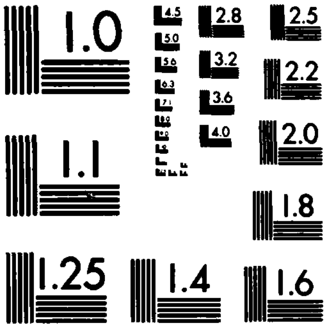

MICROCOPY RESOLUTION TEST CHART
NATIONAL BUREAU OF STANDARDS-1963-A

AFOSR-TR- 83-0797

AD-A134101

UNIVERSITY of PENNSYLVANIA
The Moore School of Electrical Engineering
PHILADELPHIA, PENNSYLVANIA 19104

Approved for public release;
distribution unlimited.

UNIVERSITY OF PENNSYLVANIA
THE MOORE SCHOOL OF ELECTRICAL ENGINEERING
ELECTRO-OPTICS AND MICROWAVE-OPTICS LABORATORY
PHILADELPHIA, PENNSYLVANIA 19104

ANNUAL REPORT

HIGH RESOLUTION 3-D TOMOGRAPHIC IMAGING BY WAVELENGTH AND POLARIZATION DIVERSITY

Prepared for the

AIR FORCE OFFICE OF SCIENTIFIC RESEARCH N/E
BUILDING 410, BOLLING AIR FORCE BASE
WASHINGTON, D.C. 20332

Under Grant

AFOSR-81-0240B
Covering the Period:
6/30/82 to 6/29/83

Prepared by

N.H. Farhat

July 5, 1983

EO/MO Report No. 6

REPORT DOCUMENTATION PAGE

READ INSTRUCTIONS
BEFORE COMPLETING FORM

1. REPORT NUMBER
AFOSR-TR- 83-0797

2. GOVT ACCESSION NO.

3. RECIPIENT'S CATALOG NUMBER
5-27423

4. TITLE (and Subtitle)
HIGH RESOLUTION 3-D TOMOGRAPHIC IMAGING
BY WAVELENGTH AND POLARIZATION DIVERSITY

5. TYPE OF REPORT & PERIOD COVERED
ANNUAL
6/30/82-6/29/83

6. PERFORMING ORG. REPORT NUMBER
EO/MO 6

7. AUTHOR(s)
N.H. FARHAT

8. CONTRACT OR GRANT NUMBER(s)
AFOSR 81-0240

9. PERFORMING ORGANIZATION NAME AND ADDRESS
University of Pennsylvania
The Moore School of Electrical Engineering
200 S. 33rd St., Phila., PA 19104

10. PROGRAM ELEMENT, PROJECT, TASK AREA & WORK UNIT NUMBERS
61102F
2305/B1

11. CONTROLLING OFFICE NAME AND ADDRESS
United States Air Force
Air Force Office of Scientific Research
Building 410, Bolling A.F.B., D.C., 20332

12. REPORT DATE
July 5, 1983

13. NUMBER OF PAGES
137

14. MONITORING AGENCY NAME & ADDRESS (if different from Controlling Office)

15. SECURITY CLASS. (of this report)
UNCLASSIFIED

15a. DECLASSIFICATION/DOWNGRADING SCHEDULE

16. DISTRIBUTION STATEMENT (of this Report)
Approved for public release;
distribution unlimited.

17. DISTRIBUTION STATEMENT (of the abstract entered in Block 20, if different from Report)

18. SUPPLEMENTARY NOTES
Three-dimensional imaging, tomography, wavelength diversity, polarization diversity, 3-D impulse response, speckle suppression, target derived reference, projection imaging, true 3-D display.

19. KEY WORDS (Continue on reverse side if necessary and identify by block number)

20. ABSTRACT (Continue on reverse side if necessary and identify by block number)

Our research in high resolution microwave imaging has to date concentrated broadly on the study and development of efficient and cost-effective data acquisition and image reconstruction methods for use in λ and polarization diversity 3-D tomographic imaging. The techniques developed, combine angular, spectral, and polarization diversity measurements with a unique *target derived reference* (TDR) technique to produce images of the scattering centers on complex-shaped bodies with unprecedented resolution and quality that exceed by

far anything reported to this date. Analytical studies of information content, speckle suppression and resolution show however that image quality can further be enhanced and made to approach and even exceed the resolution of optical systems when the imaging of remote objects specially through the earth's atmosphere is desired.

During this period image retreival from incomplete data i.e., from Fourier space data accessed over curved closed or open surfaces was investigated. It was shown that for the circular array geometry, the 3-D image detail retrieved from Fourier space data accessed over the surface of a truncated cone is nearly the same as that obtained from data accessed within the volume contained by the truncated cone. This result is of practical significance because the cost of a sampled circular array is considerably lower than the cost of a sampled circular aperture needed to access the contained volume.

Also during the period of this report a numerical study of speckle reduction by wavelength diversity was undertaken. This was accomplished by considering the impulse response of several monochromatic and λ-diversity imaging systems in the (2-96) GHz range. To simplify the analysis an idealized situation in which angular diversity over 4π[Sr] is utilized was assumed. This allows accessing the Fourier space in the monochromatic case over the surface of sphere and over a ball of the same radius in the λ-diversity case. By computing the 3-D Fourier transforms of the spherical shell and the ball, the 3-D impulse response of the idealized systems were obtained and compared. The results clearly demonstrate the role of λ - diversity in suppressing sidelobe level and in making the impulse response unipolar which factors are directly responsible fo reducing speckle noise. The results are also useful in demonstrating the advantages of extremely broad spectral windows in enhancing information content and resolution.

In the experimental component of the program our *Experimental Microwave Imaging Facility* was utilized to access a slice in the Fourier space of metalized scale models of a B-52 and the Space Shuttle using (6-17) GHz illumination and centimeter resolution projection images of the visible centers on these targetswa obtained. The 3-D resolution of the system was also determined and found to be about 1.5cm for a (6-17)GHz spectral window and a 90° angular aperture. A novel TDR technique capable of synthesizing a phase reference on the target to produce a highly desirable 3-D *Lensless Fourier Transform* recording arrangement is also demonstrated for the first time in the above work.

In another aspect of the program the first projection images of noise-like sources were obtained. Acoustical rather than microwave radiation was utilized for economical reasons in this verification. The results are the first experimental indication of the feasibility of 3-D imaging of incoherent objects utilizing frequency selective cross-correlation measurements.

To realize the full potential of the 3-D imaging capabilities of λ and polarization diversity imaging, our research has continued to address the problem of achieving a true 3-D display tomographically. The advantages of true 3-D displays is their ability to exploit the full potential of the eye-brain system for identification and classification of objects. To date results obtained with an intensified PROM spatial light modulator indicate that the high Fourier transform frame rates needed for 3-D display may be difficult to achieve with this device. Techniques for increasing the frame rate of this device have, however, been identified. Work started on high frame hybrid (opto-digital) Fourier transforms using incoherent radiation is showing greater promise at this

Report Documentation Page - Continued

time and will therefore be pursued in our future research.

Real-time true 3-D microwave imaging of distant objects with near optical resolution or better will provide a very valuable tool in several applications of interest to the Air Force. These include: damage assessment for remote aerospace targets, identification and classification of unidentified aerospace objects including space debris, radar cross-section reduction (*diaphonization*) nondestructive evaluation (NDE) of dielectric and composite materials that do not lend themselves to ultrasound inspection such as solid propellent grains, and 3-D analysis and mapping of storm centers.

TABLE OF CONTENTS

Page

Abstract

Appendix I: The Projection-Slice Theorem

Table of Contents - Continued

RESEARCH IN IMAGE UNDERSTANDING AS APPLIED TO 3-D MICROWAVE TOMOGRAPHIC IMAGING WITH NEAR OPTICAL RESOLUTION

1. INTRODUCTION

The implementation of high resolution longwave (microwave and acoustic) inverse scattering or holographic imaging systems involves measurement of the object scattered field over extended recording apertures that subtend sufficiently large solid angles at the object. Because of the discrete nature of longwave sensors, only a sampled version of the scattered field distribution over the recording aperture can be recorded. Sampling considerations ordinarily require dense sampling to avoid retrieved image degradation through deterioration of the impulse response and aliasing. The cost of implementing such densely sampled apertures is at present quite prohibitive because of the large number and high cost of the coherent sensors required to form the aperture specially for the imaging of remote scattering objects where the extent of the aperture required to yield high resolution is quite large. Obviously *aperture thinning* by reducing the number of elements can be employed to cut cost. However a systematic study of ordered and random aperture thinning [1],[2] indicates rapid deterioration in resolution and image quality with degree of thinning. The effect of aperture thinning is best described by its influence on the shape and side-lobe level of the impulse response or point spread function of the aperture [2]. It is generally true that even with an acceptable degree of thinning, where the deterioration of image quality is still tolerable, the cost of longwave apertures remains generally high. To overcome this constraint we have proposed to use a target derived reference [3]-[6] and demonstrated the utility of wavelength diversity [3],[4] as a means of making a highly thinned (sparse) aperture collect more information about a scattering conducting or nondispersive object thus imparting to the aperture a resolution capability better than would be possible monochromatically at the shortest operational wavelength case. The effect of wavelength diversity can be explained in terms of spectral aperture synthesis or as trade-off between costly spatial degrees of freedom associated with the number of elements and the less costly spectral degrees of freedom associated with wavelength diversity. Specifically one can show from inverse scattering theory [3]-[8] that coherent multiaspect monostatic or bistatic measurements of the far field scattered by a plane wave illuminated nondispersive object as a function of frequency, can be used to access the 3-D Fourier space $\Gamma(\bar{p})$ of the object scattering function $\gamma(\bar{r})$, $\bar{r}$ and $\bar{p}$ being 3-D position vectors in object space and Fourier space respectively. The scattering function represents the 3-D geometrical distribution and strength of those object scattering centers that contribute to the measured field. Normalization of the measured field for range-phase, clutter, and system frequency response leads in principle to accessing a finite volume $\Gamma_m(\bar{p})$ of the Fourier space $\Gamma(\bar{p})$. It is possible then as shown by computer simulation in references [3] and [4] to retrieve a *diffraction and noise limited* version $\gamma_d(\bar{r})$ of the object scattering function $\gamma(\bar{r})$ by 3-D Fourier inversion.

Our research program in λ and polarization diversity imaging has involved the careful analysis and numerical and experimental evaluation of the potential and utility of the concepts briefly outlined above for developing the foundations of a new generation of cost-effective imaging radar capable of providing 3-D image information about distant scatterers either *tomographically* or *projectively* with near optical resolution or even better. Such capability will be valuable in remote object identification and classification, in developing criteria for radar-cross section management, in nondestructive evaluation (NDE), and remote imaging for damage assessment.

During the current period, our research has focused on the study and assessment of efficient and "smart" procedures for data acquisition employing novel TDR techniques. These techniques applied in the (6-17) GHz have enabled the accessing of a single slice in the 3-D Fourier space of a test object and subsequent reconstruction of a projection image of the 3-D distribution of scattering centers on a complex shaped test target. Unprecedented centimeter resolution has been demonstrated using realistic data collected in our *Experimental Microwave Imaging Facility*. Despite their excellent quality, these microwave images indicate several avenues for improvement that have the potential of making them approach and perhaps exceed the resolution and quality of optical imagers attempting to image a remote aerospace target through the turbulent atmosphere realizing thus the full potential of λ and polarization diversity imaging techniques predicted by theory.

The complexity of accessing the Fourier space over the extended volumes required for the study of true 3-D tomographic imaging and the limitations on the volume of data that can be stored in and handled by our present MINC 11/03 computer have prompted us to examine the concept of tomographic (and projective) image retrieval from incomplete Fourier space data whereby the fourier space of the scatterer is accessed over a curved surface instead of over a volume as would ordinarily be needed in order to retrieve 3-D object detail. The results (see Appendix II) pave the way for a realistic way of studying 3-D tomographic imaging of scale models of aerospace and other man made objects from actual data collected in our anechoic chamber measurement facility.

During the preceeding period of our present program the emphasis has mainly been on the development of static frequency stepped measurement techniques suitable fur use in automated measurements of objects that are stationary while the data [illegible] collected. Dynamic frequency swept data acquisition techniques are needed in the imaging of moving targets. We have started the study of such dynamic methods and these will be receiving increased attention in our work. These are being developed for use in demonstrating near optical microwave imagery of a passing aircraft.

The thrust of our research in λ and polarization diversity in the future will therefore be aimed at the study and development of efficient dynamic data acquisition techniques that can be applied outside the confines of the laboratory and on the detailed study of methods of improving image quality which include the use of *a priori* knowledge and robust (noise tolerant) deconvolution for image enhancement and restoration. The fact that the 3-D accessed Fourier space data can be reduced in dimensionality to 2-D or 1-D through the application of the projection-slice theorem will permit the study and comparison of the effectiveness of 1-D and 2-D enhancement and restoration methods. In fact, reduction of dimensionality is proving to be a most useful and powerful tool in our research in image understanding and processing.

An analysis of the point-spread function (PSF) of idealized λ-diversity imaging systems shows that considerable advantages of improved resolution and speckle suppression can be obtained by increasing the spectral range beyond the (6-17) GHz range utilized so far in our experimental studies. This is expected however to lead in practice to situations where spectral information can be collected only over separate bands of the overall spectral window desired where high power sources, receivers and other gear are available. A segmented spectral window will then result leading to the accessing of the Fourier space in discontinuous unconnected regions. The feasibility of using robust interpolation methods to "fill in" the data in the missing bands will therefore be considered in our future research. The experimental counterpart of this future research requires extending the lower frequency bound of our measurement system down to 2 GHz or lower and the upper bound initially to 40 GHz. (A proposal to extend the operation of our experimental microwave imaging facility well into the millimeter wave range up to 110 GHz has been submitted for consideration under the DoD-University Research Instrumentation Grants Program). Reducing the lower bound of our system from 6 GHz to 2 GHz is particularly important for supressing certain resonance effects apparent in the images retrieved so far, while increasing the upper bound will lead to visualization of finer detail of the test objects utilized in our studies. The net effect is expected to be a dramatic improvement of image quality beyond the good images already obtained.

To fully utilize the 3-D imaging capabilities of λ and polarization diversity imaging we have been also concerned with the study of high speed hybrid (opto-digital) computing as a means for true 3-D image reconstruction and display. The ability to display a true 3-D image is extremely important for exploiting the full potential of the human eye-brain system in recognition specially when the number of the 3-D distributed microwave scattering centers on a visualized target is limited. One hybrid computing scheme being studied is based on carrying out a series of 2-D optical Fourier transforms at very high frame rates employing incoherent light. The ability to perform a 2-D fourier transforms of natural scenes at high speed with this scheme provides a new means of 3-D image formation based again on the projection-slice theorem which will be considered also in our future work in addition to our research in 3-D incoherent imaging techniques that employ spectrally selective cross-correlation measurements.

2. THEORETICAL CONSIDERATIONS

Presented in this chapter are the theoretical considerations on which the proposed research program is based. Although some of the material in this chapter appeared in preceeding reports, it is included here for completion.

2.1 Vector Formulation of 3-D Tomographic Imaging by λ and Polarization Diversity

The aim of this formulation is to provide the basic vector equations for the far field scattered by a metallic obstacle whose size is much larger than the wavelength of the incident illumination. The approach adopted in the formulation was based on reviewing first the derivation of the expressions for the field radiated by a bounded three dimensional sinusoidal current distribution. The results were then used to formulate scattering from a perfectly conducting obstacle in terms of surface current distributions induced by the incident illumination. As compared to other treatments of electromagnetic scattering, based on Green's Theorem [9]-[11], our treatment [12] has the advantage of avoiding the complexities of introducing line current sources on the shadow boundary of an illuminated scatterer that are needed in order to make the scattering field obey Maxwell's equations.

The vector formulation yielded the following results, which we summarize here since they will be referred to in subsequent discussion in this report.

The field scattered from a conducting object under plane wave illumination is given by

$$\bar{E}(\bar{r},\bar{p}) = \frac{j\omega\mu e^{-jkr}}{2\pi r} \int \bar{O}(\bar{r}')\, e^{j\bar{p}\cdot\bar{r}'} d\bar{r}' . \qquad (1)$$

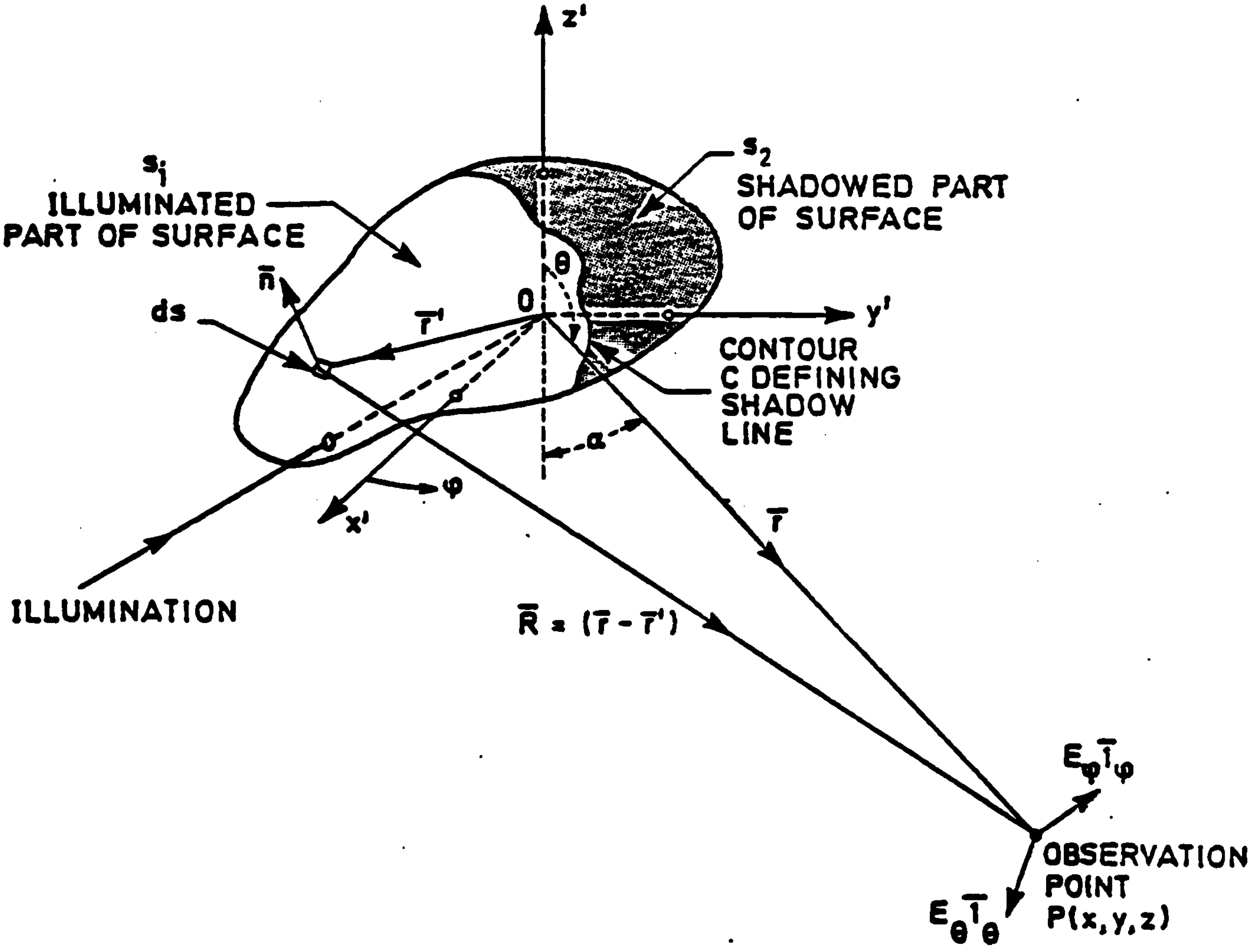

Fig. 1. Scattering geometry.

in which referring to Fig. 1 the integral

$$\overline{\Gamma}(\overline{p}) = \int \overline{O}(\overline{r}') \, e^{j\overline{p}\cdot\overline{r}'} \, d\overline{r}' = -j \, \frac{2\pi r}{\omega\mu} \, e^{jkr} \, \overline{E}(\overline{r},\overline{p}) \tag{2}$$

extends over all $\overline{r}'$ space and is therefore recognized as the three dimensional Fourier transform of the object characteristic function

$$\overline{O}(\overline{r}') = \begin{cases} \overline{n}(\overline{r}') \times \overline{H}_o^i - \{\overline{n}(\overline{r}') \times \overline{H}_o^i \cdot \overline{1}_r\} \, \overline{1}_r \ \ldots\ldots \ \overline{r}' \text{ on } s_i \\ \\ 0 \ \ldots\ldots\ldots\ldots\ldots\ldots\ldots\ldots\ldots\ldots \text{elsewhere} \end{cases} \tag{3}$$

Note that $\overline{O}(\overline{r}')$ is a function of the shape of the illuminated surface of the scatterer (through the specification that $\overline{r}'$ is on s_i) and on the state of polarization of the incident illumination through the magnetic field $\overline{H}_o^i$ of the incident plane wave illumination. Note $\overline{H}_o^i$ is the value of magnetic field vector at the origin of Fig. 1. In eqs. (1) and (2)

$$\overline{p} = k \, (\overline{1}_r - \overline{1}_i) \tag{3a}$$

$$p = 2k \cos \frac{\beta}{2} \tag{3b}$$

where $\overline{1}_r$ and $\overline{1}_i$ are unit vectors in the direction of observation and illumination in Fig. 1 and β is the angle between $\overline{1}_r$ and $-\overline{1}_i$. In addition to being dependent on the shape of the object the integral in eq. (2) is dependent on the state of polarization of the incident field provided the direction of the observation points $\overline{1}_r$ does not equal $-\overline{1}_i$.

The object characteristic function can thus be determined by means of a three dimensional inverse Fourier transform of $\overline{\Gamma}(\overline{p})$ i.e.

$$\overline{O}(\overline{r}_i) = \int \overline{\Gamma}(\overline{p}) \, e^{-j\overline{p}\cdot\overline{r}_i} \, d\overline{p} \tag{4a}$$

or

$$\overline{O}(\overline{r}_i) = \int j\frac{2\pi r}{\omega\mu} e^{jkr} \; \overline{E}(\overline{r},\overline{p}) \; e^{-j\overline{p}\cdot\overline{r}_i} \; d\overline{p} \qquad (4b)$$

where $\overline{r}_i$ is a three dimensional position vector in "image" space.

Multiaspect complex frequency response measurement with polarization discrimination can be used to effect the measurement of $\overline{\Gamma}(\overline{p})$ over a finite region of $\overline{p}$ space specified by a sampling function $H(\overline{p})$ representing the values assumed by the vector $\overline{p}$. Thus what we measure is $\Gamma_m(\overline{p}) = \Gamma(\overline{p})\ H(\overline{p})$. Such measurement carried with a finite number of widely dispersed receivers permit therefore the accessing of a finite sampled volume of the three dimensional Fourier space or $\overline{p}$ space of the scattering object. The size and shape of $H(\overline{p})$, the volume in $\overline{p}$ space in which the acquired portion of $\Gamma_m(\overline{p})$ is stored depends on the receiver array size and geometry relative to the scatterer and on the spectral window utilized.

Equations (1), (2) and (4) form the basis for three-dimensional imaging of distant perfectly conducting scatterers by wavelength and polarization diversity. The result in equation (4) shows that it is possible to access a finite volume in the three-dimensional Fourier space of the object characteristic function by complex multistatic polarization discriminating measurement of the scattered field $\overline{E}(\overline{r},\overline{p})$ as a function of wavelength for as many scattering directions $\overline{1}_r$ as practically possible. This step is followed by correction of the $\overline{E}(r,\overline{p})$ data by multiplication by the factor $(j\ \frac{2\pi r}{\omega\mu}\ e^{jkr})$ to obtain $\overline{\Gamma}(\overline{p})$. This requires as pointed out earlier knowledge of the range r between the scatterer and each observation point involved in the multistatic scattered field measurement. The complex (amplitude and phase) nature of the required field measurements calls for the availability of a common reference signal at each receiver in order to synchronize the recording array elements while storage of the range corrected data $\bar{\Gamma}(\bar{p})$ in the appropriate locations in $\bar{p}$ space requires knowledge of the vector $\bar{p} = k(\bar{1}_r - \bar{1}_i)$ for each receiver. Coherent wavelength and polarization measurements of the scattered field is realized in practice with the aid of broadband coherent receivers with polarization discriminating antennas. Referring to Fig. 1 we see that a dual polarization antenna at point P(x,y,z) aimed at the scattering object can measure the orthogonal complex field amplitudes E_θ and E_ϕ in the θ and ϕ directions of a spherical coordinate system, r,θ,ϕ centered at 0. Measurement of E_θ and E_ϕ in amplitude and phase will completely characterize, the state of polarization of the scattered field and would double the amount of information recorded as compared to "scalarized" measurements where the vector nature of the scattered field is ignored and only one measurement of the field is made. Once E_θ and E_ϕ have been measured corresponding cartesian components can be computed from,

$$\left.\begin{aligned} E_x &= E_\theta \cos\psi \cos\alpha + E_\psi \sin\psi \\ E_y &= -E_\theta \sin\psi \cos\alpha + E_\psi \cos\psi \\ E_z &= -E_\theta \sin\alpha \end{aligned}\right\} \qquad (5)$$

In this fashion, regardless of state of polarization, all field measurements irrespective of scattering direction are reduced each to three cartesian components of $\bar{E}(\bar{r},\bar{p})$. Accordingly eq. (4) can be separated into three corresponding components $0_x(\bar{r}_i)$, $0_y(\bar{r}_i)$ $0_z(\bar{r}_i)$ with the final polarization diversity image being given by,

$$|\bar{0}(\bar{r}_i)|^2 = |0_x|^2 + |0_y|^2 + |0_z|^2 \qquad (6)$$

i.e. by incoherent superposition of the component images.

The imaging formulation described above accounts fully for the vector nature of the field. Therefore it furnishes a more precise and attractive approach to the implementation of 3-D imaging by wavelength and polarization diversity than a scalar formulation because of its greater utilization the information content in the scattered field.

2.2 Three-Dimensional Tomographic Image Reconstruction From λ and Polarization Diversity Data.

As a result of the electronic mode of detection employed in wavelength and polarization diversity imaging the measured or accessed Fourier domain data $\Gamma_m(\bar{p})$ will most probably be stored in computer memory. It is logical then to carry out the image reconstruction procedure outlined above by means of digital computation using a three-dimensional fast Fourier Transform algorithm. This approach can however be quite cumbersome if we are to preserve polarization information because of the vector natures of $\bar{\Gamma}(\bar{p})$ and the reconstruction operations indicated in eqs. (4) and (6). There are advantages to carrying out the image retrieval operation in part digitally and in part optically i.e. in a hybrid (opto-digital) computing mode. One advantage of this hybrid approach is a potential for true 3-D display of image detail [13] which is not possible in a purely digital image reconstruction approach because of the inherent two-dimensionality of present day computer displays. A second advantage is the possibility of high throughput because of the parallel processing capabilities of optical computing especially when a rapid recyclable spatial light modulator is employed to introduce the data in the optical processor instead of the usual photographic transparency in order to achieve real-time operation [13]. A third advantage is the provision of a simple way in which the operation in eq. (6) is realized. The basis for the hybrid processing scheme are the *Fourier Domain Projection*

Theorems which were discussed elsewhere [3],[4],[14]-[19] for the case of scalar Fourier space data and are extended below to the case of a vector Fourier space. In accordance to these theorems central (or parallel) slices of the object characteristic function, (or more precisely in our case of cross-sectional outlines since the object is perfectly reflecting, can be reconstructed from two-dimensional Fourier transforms of directional projections (or weighted projections taken in the one direction) of the 3-D Fourier space data. Both the directional and the weighted projections yield two-dimensional data manifolds which can be regarded as *projection holograms* that lend themselves readily to 2-D Fourier transformation. Although the required 2-D Fourier transform of such projection holograms may be carried out digitally, optical implementation employing the 2-D Fourier transforming property of the simple lens in coherent (laser) light [20] may be preferable in some instances.

The preceeding remarks can be placed on a more quantitative basis by considering the weighted projection of $\overline{\Gamma}(\overline{p})$ for example on the p_x-p_y plane i.e.

$$\overline{\Gamma}^{\alpha}_{proj}(p_x,p_y) = \int \overline{\Gamma}(p_x,p_y,p_z)\, e^{-j\alpha p_z}\, dp_z \tag{7}$$

where α is a real weighting constant. In accordance to eq. (4a) we can express $\overline{\Gamma}(\overline{p})$ as

$$\overline{\Gamma}(\overline{p}) = \int \overline{O}(\overline{r}_i)\, e^{j\overline{p}\cdot\overline{r}_i}\, d\overline{r}_i \tag{8}$$

Combining eqs. (7) and (8) and carrying out the integration first with respect to p_z, assuming that the extent of $\overline{\Gamma}(\overline{p})$ in $\overline{p}$-space in the direction of projection is sufficiently large to yield $\delta(z_i-\alpha)$ then with respect to z_i we obtain,

$$\overline{\Gamma}^{\alpha}_{proj}\ (p_x,p_y) = \int_{x_i}\int_{y_i} \overline{O}(x_i,y_i,z_i = \alpha)\, e^{-j(p_x x_i + p_y y_i)}\ dx_i dy_i \qquad (9)$$

which means that the weighted projection $\overline{\Gamma}^{\alpha}_{proj}$ of $\overline{\Gamma}(\overline{p})$ on the p_x-p_y plane and a slice or cross-sectional outline though the object function made by the plane $z_i = \alpha$ are a two-dimensional Fourier transform pair. Consequently by varying the weighting factor α one can obtain weighted projection holograms that can be 2-D Fourier transformed to yield a series of parallel slices through the object that lie in our example normal to the z_i direction. Parallel slices normal to any other direction can also be readily obtained by projecting $\overline{\Gamma}(\overline{p})$ on a plane normal to the desired direction. Futhermore central or meridional slices through the object at different orientations can be obtained by setting $\alpha = 0$ and forming a series of projections of $\overline{\Gamma}(p)$ on a set of planes in p-space with differing orientations. The orientations of each plane defines the orientation of the image slice obtained from 2-D Fourier transformation of the corresponding projection hologram. A more formal derivation of the above results often referred to as the projection-slice theorem is given in Appendix I.

Because $\overline{\Gamma}(\overline{p})$ is a vector function each of its projections will actually consist in accordance to eqs. (4a) and (9) of three cartesian components corresponding to the cartesian components of $\overline{O}(\overline{r}_i)$. To retrieve any slice through $\overline{O}(\overline{r}_i)$ we must compute the three cartesian components of each projection obtaining thereby three projection holograms, Fourier transform each of these to obtain the values of O_x,O_y and O_z corresponding to the particular slice then use eq. (6) to reconstruct the intensity image of the slice. Obviously this procedure can be quite lengthy if it is to be carried out entirely by digital computing. The advantage of hybrid processing is that once the cartesian components of any projection hologram have been digitally computed, they can be introduced to the optical bench as described in [3] and [4] either photographically or by means of an optically addressed SLM in the form of a randomly multiplexed array of holograms [13]. The 2-D optical Fourier transformation of such a composite hologram will yield the desired image intensity of the slice directly provided that the coherence area of the interrogating light falling on the composite hologram plane is the same as the size of the individual holograms forming the composite hologram. The reduced coherence properties of the interrogating light helps suppress image granularity caused by speckle and coherent noise. The ability to select the coherence properties of interrogating light by controlling spectral bandwidth and size of the source represent an additional important advantage of hybrid processing over an entirely digital approach where the amount of digital computations needed to realize the effect of reconstruction with a finite bandwidth source increases in proportion to the number of wavelengths involved. It is worthwhile to keep in mind however that the precision and high dynamic range of digital processing have not been approached yet by the most elaborate coherent optical computing schemes. Digital methods furthermore can handle complex inputs readily while optical computing utilizes ordinarily a holographic intensity record of the function being processed and consequently conjugate images result. These will overlap causing image degradation unless they are spatially separated through the introduction of a spatial carrier in the data being processed.

The preceeding discussion illustrates the great advantage of wavelength diversity techniques in gaining access to the 3-D Fourier space of the object function. Once the Fourier space data $\overline{\Gamma}(\overline{p})$ is obtained one can reconstruct tomographically 3-D image detail of the object characteristic function for any of a wide range of viewing direction by hybrid opto-digital computing based on versatile Fourier domain projection theorems.

2.3 Image Resolution, Structural Degrees of Freedom, and Information Content

Three-dimensional image resolution in wavelength and polarization diversity imaging can be determined following the standard method of evaluating the 3-D impulse response of the system. The larger the volume of the accessed p-space volume ($H(\bar{p})$) occupied by $\bar{\Gamma}_m(\bar{p})$ the finer will be the resolution. The size and shape $H(\bar{p})$ of the accessed volume depends however, in accordance to eqs. (1) and (2), on the values assumed by the vector $\bar{p} = k\,(\bar{1}_r - \bar{1}_i)$ which depend in turn on the number and angular distribution, relative to the object, of the observation points or receiving stations (through the unit vector $\bar{1}_r$) and on the spectral range (through k) over which the scattered field $\bar{E}(\bar{r},\bar{p})$ is measured. Thus with $\Gamma(\bar{p})$ representing the 3-D Fourier transform of the object characteristic function $\bar{O}(\bar{r}')$, we express the Fourier space data $\bar{\Gamma}_m(\bar{p})$ measured in practice as a truncated version of $\Gamma(\bar{p})$ that is,

$$\bar{\Gamma}_m(\bar{p}) = H(\bar{p})\bar{\Gamma}(\bar{p}) \tag{10}$$

where $H(\bar{p})$ as stated already is a sampling function defining the points in $\bar{p}$-space over which measurements were made. When wavelength diversity by discrete frequency stepping is employed, we can express the sampling function as,

$$H(\bar{p}) = \sum_m \sum_n \delta(\bar{p} - \bar{p}_{mn}) \tag{11}$$

where $\delta(.)$ is the Dirac delta "function", m designates the observation point, n designates the frequency point and $\bar{p}_{mn}$ indicates the position vector of points in $\bar{p}$-space assumed by the m-th observation point as one steps through the available frequency points. If rapid frequency stepping in equal increments is employed, as would probably be the case in practice, we can express $\bar{p}_{mn}$ as,

$$\bar{p}_{mn} = \bar{p}_{mo} + n\Delta\bar{p}_m \quad , \qquad n = \begin{cases} 0, \pm 1, \pm 2, \ldots \pm (N-1)/2 & \text{for N odd} \\ \pm\frac{1}{2}, \pm\frac{3}{2}, \ldots \pm (N-1)/2 & \text{for N even} \end{cases} \tag{12}$$

where

$$\Delta\bar{p}_m = \Delta k \, (\bar{1}_{r_m} - \bar{1}_i) \tag{13}$$

with $\Delta k = \Delta\omega/c$, $\Delta\omega$ being the angular frequency increment and c is the velocity of light.

Three-dimensional Fourier transformation of $\bar{\Gamma}(\bar{p})$, to retrieve a 3-D image of the object characteristic function, will therefore yield in accordance to eq. (10) a diffraction limited or degraded image,

$$O_d(\bar{r}_i) = h(\bar{r}_i) *** \bar{O}(\bar{r}_i) \tag{14}$$

where the triple asterisks designate a three dimensional convolution operation, $\bar{r}_i$ is a position vector in image space, $\bar{O}(\bar{r}_i)$ is the object characteristic function and

$$h(\bar{r}_i) = \int H(\bar{p}) e^{j\bar{p}\cdot\bar{r}_i} \, d\bar{p} \tag{15}$$

is within a constant $(\frac{1}{2\pi})^3$ the 3-D Fourier transform of the sampling function. In accordance to linear system theory $h(\bar{r}_i)$ in eqs. (14) and (15) represents the 3-D *impulse response* of the imaging system. Making use of eqs. (11) to (13) in (15) and carrying out the integration yields,

$$h(\overline{r}_i) = \sum_m \sum_n e^{j(\overline{p}_{mo} + n\Delta\overline{p}_m)\cdot\overline{r}_i} \tag{16}$$

which can be reduced to,

$$h(\overline{r}_i) = \sum_m e^{j\overline{p}_{mo}\cdot\overline{r}_i} \frac{\sin(\frac{1}{2} N\Delta\overline{p}_m\cdot\overline{r}_i)}{\sin(\frac{1}{2} \Delta p_m\cdot\overline{r}_i)} \tag{17}$$

We note that in the arguments of the sin(.) functions in eq. (17) the term $\Delta\overline{p}_m\cdot\overline{r}_i$ = const. describes a plane in the 3-D image space $\overline{r}_i$ that is normal to $\Delta\overline{p}_m$. The ratio of the two sin(.) terms, which is similar to that encountered in the analysis of gratings, describes a set of parallel "fuzzy" planes of finite thickness that are normal to $\Delta\overline{p}_m$ or to the direction of $\overline{p}_m$ with the spacing between adjacent planes being,

$$D_m = \frac{2\pi}{\Delta p_m} = \frac{C}{2\Delta f \cos(\frac{\beta_m}{2})} \tag{18}$$

where in accordance to eq. (3b) we made use of $\Delta p_m = 2\Delta k \cos(\frac{\beta_m}{2}) = \frac{4\pi}{c} \Delta f \cos(\frac{\beta_m}{2})$ with β_m being the *bistatic angle* between the transmitter (illuminator) and the m-th receiver or observation point as seen from the object. For large values of $N\Delta p_m$ the "half-width" or thickness of each of the fuzzy planes can be shown to be of the order of,

$$d_m = \frac{2.76}{N\Delta p_m} = \frac{2.76\ C}{4\pi\ N\Delta f \cos(\frac{\beta_m}{2})} \tag{19}$$

We note that $N\Delta f$ is the total width of the spectral window available for data acquisition. It is useful to obtain an idea of a typical value of d_m.

For this purpose we assume a microwave spectral range $N\Delta f = 10$ GHz and $\beta_m = 30°$ to find $d_m = 6.8$ mm. The values of d_m are important since the impulse response given by eq. (17) is formed by the addition of planes of this order of thickness that are at various inclination to each other.

When the directions assumed by $\Delta\overline{p}_m$ or $\overline{p}_m$ for the various observation points or receiver stations are sufficiently varied, the M zero order fuzzy planes in eq. (17) to which these directions are normal, will add at the origin to form a sort of fuzzy 3-D peak of strength (MxN) from which in addition to the planes themselves of strength N, a pattern of fuzzy lines defining the intersection of pairs of inclined planes will be radiating outward in a complicated 3-D spoke-like manner. The strength of these lines will depend on the relative phase of the intersecting planes (note the phase term in eq. (17)) and will range from zero (terms out of phase) to a maximum of 2N (terms in phase). In a like manner, the superposition of the higher order terms of the sin(NX)/sinx term in eq. (17) will give rise to complicated clusters of planes normal to the $\overline{p}_m$ directions and to associated intersection lines. These will form at radial distances from the origin equal to multiples of the distance D_m and represent the various side lobes of the 3-D impulse response $h(\overline{r}_i)$. It is worthwhile to note that when the bistatic scattering angle β_m is nearly the same for all observation points, as would occur in the case of a circular or annular array of observation points or receiving stations surrounding a central illuminator,for a wide range of distant object locations, the values of D_m will be nearly the same and the side-lobe structure formed by each of the higher order terms in $h(\overline{r}_i)$ will be more tightly grouped giving rise to a more well defined side-lobe structure at radial intervals $D_m \simeq$ const. This is the first advantage for using a circular (annular) array of receivers in wavelength and polarization diversity imaging. Other advantages will emerge in the course of this discussion and in Appendix III.

It is clear from the preceeding discussion that the ratio of the central peak in the 3-D impulse response to any other outlying side-lobe structure of $h(\overline{r}_i)$ is of the order of M, the number of observation points. Being however semi-quantitative in nature, the preceeding discussion cannot furnish exact information on the 3-D size and shape of the central peak of the impulse response which would determine the resolution capability of the system. It can be seen however that this shape and size will depend on values of $\Delta\overline{p}_m$ or $\overline{p}_m$ i.e. on the angular positions of the observation points relative to the object. The 3-D impulse response in wavelength and polarization diversity imaging is *not* therefore *spatially invariant* as in most conventional imaging systems. It also can be seen that the 3-D shape and size of the central peak is determined by the superposition at the origin $\overline{r}_i = 0$ of M inclined planes each normal to a direction $\overline{p}_m$ and all passing through the origin. Since the thickness of these planes as estimated from eq. (19) can be quite small the dimensions of the central peak is expected to be roughly several times the value of d_m.

In practice one is often more interested in the lateral and longitudinal resolutions. In particular when tomographic reconstruction of 3-D image detail is obtained as described earlier. The 2-D lateral resolution of these slices is of practical interest then together with the longitudinal resolution in the direction of slicing which determines the minimum distance between parallel slices. In this case one would proceed by computing the projection of the 3-D sampling function $H(\overline{p})$ of eq. (11) on a plane parallel to the direction of the desired parallel slices then calculate the 2-D Fourier transform of these projections to obtain the lateral resolution in the plane of the slices. The longitudinal resolution in the direction of slicing is roughly equal to the extent of $H(\overline{p})$ in that direction. An example of this procedure for computing *tomographic resolution* is given in [4].

Classically the concept of resolution is a measure of image information content in the absence of noise. In the presence of noise the actual resolution and image information content must be treated differently. One would begin by counting the *structural degrees of freedeom* $\mathcal{F}$ of the measured wavefield [21]-[23]. A straight forward extension of a formula derived by Gabor [21] (see also Appendix II) to the three-dimensional case yields,

$$\mathcal{F} = 2x2x2x \ \{\text{Object volume}\} \times \{\text{Accessed volume of Fourier space}\} \quad (20a)$$

or

$$\mathcal{F} = 8 \times V_{obj} \times V_{p\text{-space}} \quad (20b)$$

with V standing for volume. The first factor of 2 is used when coherent heterodyne detection in which the amplitude and phase of the field is measured. The second factor of 2 accounts for the complex nature of the Fourier transform data of the object defining the accessed volume in Fourier space. The third factor of 2 is used when two orthogonal components of the vector wavefield are measured to account for polarization of the scattered far field as discussed in Section 1. Note that $\mathcal{F}$ is a dimensionless quantity. The number of degrees of freedom $\mathcal{F}$ represents the number of independent real parameters needed to describe the wavefield measured or collected by the imaging system completely. Each degree of freedom consists of an infinite number of values if it can be measured with infinite precision. We know however that in practice this is not possible. The number of distinguishable values of each of the independent parameters $\mathcal{F}$ will depend on signal-to-noise ratio (SNR). Thus if the mean energies of the signal and noise are P_s and P_n respectively, the number of distinguishable levels is $(1 + P_s/P_n)$. The number of bits needed to indicate a measured parameter is therefore $\log_2(1 + P_s/P_n)$. If we assume each degree of freedom is handled by the imaging system independently, the imaging system can be considered as F parallel communication channels to each of which we can apply Shannon's well known formula for information capacity namely,

$$C = B \log_2 \left(1 + \frac{P_s}{P_n} \right) \quad [\text{bits/sec}] \tag{21}$$

where B is the electronic or temporal bandwidth of the channel which in our case is the bandwidth of a tunable receiver employed in coherent detection of the field. The overall information capacity of the F channels is therefore

$$C_F = F \; B \log_2 \left(1 + \frac{P_s}{P_n} \right) \quad [\text{bits/sec}] \tag{22}$$

Each coherent measurement of amplitude and phase takes a time $\tau \simeq 1/B$. The information content of the resultant image is therefore

$$C_i = C_F \tau = F \log_2 \left(1 + \frac{P_s}{P_n}\right) \quad [\text{bits}] \tag{23}$$

This is the maximum information content in the image when both the signal and noise have Gaussian statistics. Equation (23) gives a better measure of image quality than a mere knowledge of the classical diffraction limited resolution. We see from eqs. (20) and (24) that it is desirable in practice to maximize F and to employ a sufficiently high SNR. The great advantage of using wavelength and polarization diversity to increase the value of F by adding spectral and polarization degrees of freedom is now apparent. The spectral degrees of freedom enter eq. (28) through the Fourier space volume term which is the volume occupied by the sampling function $H(\overline{p})$ discussed earlier. As pointed out repeatedly before, the size of this volume depends on the values assumed by the vector $\overline{p}$ which depend in turn on the frequency or wavelength range employed and on the angular distribution of observation points relative to the object. As long as the sampling in $\overline{p}$-space specified by $H(\overline{p})$ obeys the Nyquist criterion the volume occupied by $H(\overline{p})$ can be used directly in eq. (20). It is worthwhile to note that because of the nature of the vector $\overline{p}$, and the finite frequency range, the sampling volume $H(\overline{p})$ will usually resemble a truncated cone especially for the case of the circular array. The Nyquist rate required to avoid aliasing or image overlap when the image of the characteristic function $O(\overline{r}_i)$ is convolved with the 3-D impulse response $h(\overline{r}_i)$ in eq. (14) will be realized when the spacing D_m between the central peak and the first side-lobe structure of the 3-D impulse response described earlier is larger than the size ℓ of the object. Then by setting $D_m = \ell$ and using eq. (18) we can obtain an expression for the incremental frequency step Δf_m required to avoid aliasing namely,

$$\Delta f_m = \frac{c}{2\ell \cos\left(\frac{\beta_m}{2}\right)} \quad . \tag{24}$$

The value of Δf_m is generally dependent on the bistatic angle β_m. However for the circular array arrangement described earlier β_m is nearly the same for all observation points and the same value of Δf can be used at all receivers. In an imaging radar situation employing such a circular array with β_m as seen from the object being approximately 30°, the incremental frequency step required to avoid aliasing in the imaging of a remote object such as a satellite of size $\ell = 10$m is 15.5 MHz. This means that coverage of a spectral window of 10 GHz will require 645 frequency steps at each of which two complex (amplitude and phase) measurements of the scattered field at each observation point are made one of the E_θ component and one for the E_ϕ component to account for polarization information as discussed in Section 2.1. A circular array for example of 50 receivers will therefore generate 64,516 real independent data points. These must be stored in computer memory together with their $\bar{p}$-space locations which requires specification of p_x, p_y and p_z for each point resulting in a total storage space requirement for 193,548 real, numbers. Such storage capacity is easily met by most present day computers.

The value of P_s/P_n in eq. (23) represents the mean signal-to-noise ratio in the detection process. The value of P_s is determined by the well known radar equation,

$$P_s = \frac{P_T\ G_T\ G_R\ \lambda^2\ \sigma\ \gamma}{(4\pi)^3\ R_T^2\ R_R^2} \tag{25}$$

where P_T is the transmitter or illuminator power, G_T and G_R are the gains of the transmitting and receiving antennas respectively, λ is the wavelength, σ is the bistatic radar cross-section of the object, γ is an atmospheric and transmission lines loss factor, R_T is the transmitter to object distance and R_R is the distance between the object to a receiving point. Note in an optical system G_T and G_R represent the gains of the transmitting and receiving optics respectively with the gain G of any aperture of area A being given by $G = 4\pi A/\lambda^2$.

The noise level P_n is determined generally by the sum of photon noise, electronic or thermal noise of the receiver and is influenced by other undesirable effects such as speckle noise caused by the coherent nature of the illumination used and the random scattering process at the object as a result of surface roughness or random distribution of scattering centers [1],[2]. At microwave and mmw frequencies photon noise is negligible compared to thermal noise with the reverse being usually true at optical and infrared frequencies. An estimate of the thermal noise power of a receiver with noise figure NF can be obtained from,

$$p_n \simeq KTB\ NF \qquad (26)$$

where K is Boltzmans constant, T is the temperature, and B is the receiver bandwidth. Typically a tuned receiver with NF = 10 dB and bandwidth B = 10 kHz will therefore have a thermal noise level of about 10^{-15} watts. A received signal power of 10^{-13} watts will provide an SNR of 100. Thus an estimate of $\log_2 (1 + \frac{p_s}{p_n}) = \log_2(101)$ in eq. (23) for this case is 6.64. Note that the assumed bandwidth will permit making the 645 measurements in less than a second.

To obtain an estimate of F, it remains to determine the volume of $\bar{p}$-space accessed in a typical situation. This is the volume defined by the sampling function $H(\bar{p})$. For a circular receiving array arrangement the sampling points defined by $H(\bar{p})$ will fall on the curved surface of a circular truncated cone with apex at the origin of a $\bar{p}$-space coordinate system centered at the object. Strictly speaking such a truncated cone shape of $H(\bar{p})$ will result only when the scattering object is centrally located directly above the circular array. As the object location moves off axis the truncated cone becomes elliptical in cross-section. For the purpose of this discussion however we will take the volume of the truncated circular cone as a good estimate of the volume of accessed $\bar{p}$-space for a wide range of object locations in the hemisphere above the circular array. Cone truncation is due to the finite extent of available spectral range. We note next that as long as the sampling arrays of delta function of $H(\bar{p})$ that lie on the curved surface of the truncated cone obey the Nyquist rate, projection holograms prepared from data associated with such an $H(\overline{p})$ and another $H(\overline{p})$ in which data within the truncated cone is also collected will not differ much. To collect data within the truncated cone however additional receiving stations or observation points must be deployed within the area contained by the circular array (see Fig. 2). This is another important advantage for using an annular array arrangement , since nearly the same performance of a circular aperture filled with receiving stations is achieved with a much fewer number of receivers (see reprint in Appendix III for detail). The above argument allows us to equate $V_{p\text{-space}}$ in eq. (20b) to the volume contained within the truncated cone defined by $H(\overline{p})$ for the annular array arrangement. Using the formula for the volume of a cone of height p and base radius r, i.e., $V = \pi r^2 p/3$, we obtain for the volume of a truncated cone extending from height $p_1 = 2k_1 \cos\frac{\beta}{2}$ to height $p_2 = 2k_2 \cos\frac{\beta}{2}$ which defines $V_{p\text{-space}}$,

$$V_{p\text{-space}} = \frac{1}{3}\pi r_2^2 p_2 - \frac{1}{3}\pi r_1^{\,2} p_1$$

$$= \frac{1}{3}\left(\frac{\pi r_2^{\,2}}{p_2^{\,2}}\right) p_2^{\,3} - \frac{1}{3}\left(\frac{\pi r_1^{\,2}}{p_1^{\,2}}\right) p_1^{\,3} \qquad (27)$$

The quantities in the brackets are recognized as definitions of the solid angle Ω of the accessed $\overline{p}$-space cone. Therefore

$$V_{p\text{-space}} = \frac{1}{3}\Omega\,(p_2^{\,3} - p_1^{\,3}) \qquad (28)$$

or by substituting for p_1 and p_2 from eq. (3b),

$$V_{p\text{-space}} = \frac{8}{3}\Omega\cos^3\frac{\beta}{2}(k_2^{\,3} - k_1^{\,3}) \qquad (29)$$

where k_1 and k_2 are the wavenumbers at the lower and upper limits of the

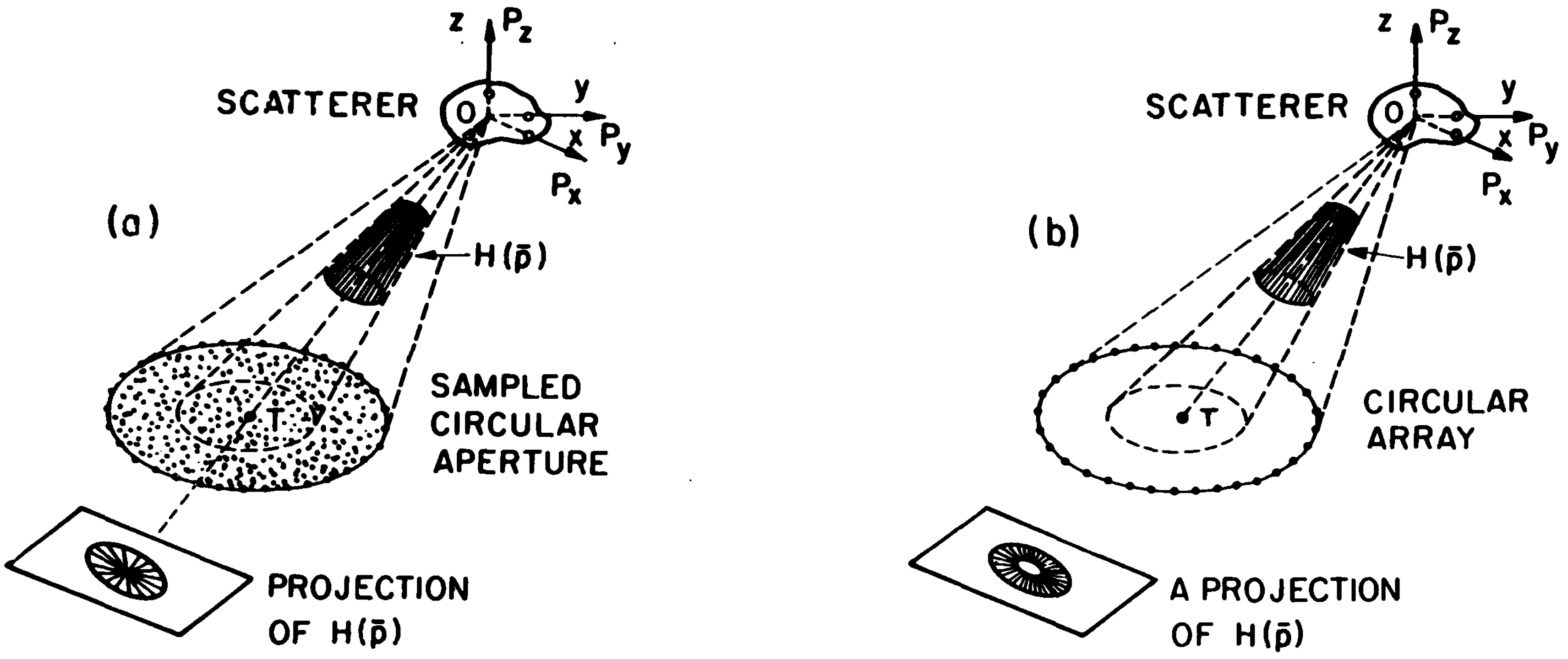

Fig. 2. Comparison of $H(\overline{p})$ for circular aperture and a circular array.

spectral range employed. Substituting for the wavenumbers $k = 2\pi f/c$ we can express eq. (29) in terms of upper and lower frequency bounds f_2 and f_1 as,

$$V_{\text{p-space}} = \frac{64\pi^3}{3c^3}\ \Omega\ \cos^3 \frac{\beta}{2}(f_2{}^3 - f_1{}^3) \tag{30}$$

Because the $\bar{p}$-space lines generating the truncated cone bisect the bistatic angle β the solid angle Ω of this cone can readily be computed as,

$$\Omega = \pi \tan^2 \frac{\beta}{2} \tag{31}$$

Combining eqs. (30) and (31) we obtain

$$V_{\text{p-space}} = \frac{6\ \pi^4\ \sin^2\ \beta}{c^3}\ (f_2{}^3 - f_1{}^3) \tag{32}$$

Note equation (32) has been derived for bistatic probing where β=0. Assuming $\beta = 30°$, $f_2 = 18$ GHz, $f_1 = 8$ GHz eq. (32) yields $V_{\text{p-space}} = 7\ 10^4$ $[1/m^3]$. For an object volume $V_{obj} = 10x10x10\ [m^3]$ eq. (20) for the degrees of freedom yields,

$$F = 8 \times 10^3 \times 7\ 10^4 = 5.6\ 10^8$$

The maximum information content of the 3-D image as obtained from eq. (23) for the previously considered case of SNR = 100 i.e. $\log_2\ (1 + \frac{P_s}{P_n}) = 6.64$ will therefore be,

$$C_i = F \log_2\ (1 + \frac{P_s}{P_n}) = 3.7\ 10^9 \quad [\text{bits}] \tag{33}$$

This is a remarkable information content nearly comparable to that encountered in an optical image. It represents the basic motive for our research program as it predicts that broadband microwave imaging systems are capable in principle of achieving resolution comparable and even better than optical systems in the imaging of remote targets through the atmosphere in a cost effective manner. It should be noted however that this is a maximum information content which can be degraded when the presence of *speckle noise* associated with coherent illumination, which we have so far excluded from the discussion, is taken into account. The reason for this exclusion is that speckle noise is different from other noise phenomena in that it is not additive but multiplicative [24],[25] because it is signal dependent. This prevents the direct inclusion of speckle noise in eq. (23). Speckle is caused by mutual interference of the fields scattered from a coherently illuminated rough object or an object with random distribution of scattering centers. It can also be produced when coherent electromagnetic radiation passes through a randomly disturbing propagation medium such as the ionosphere in radio wave propagation or a glass diffusior in the optical regime. As a result images of monochromatically illuminated objects contain a degrading granular structure commonly referred to as *speckle or coherent noise* which can be particularly deleterious in microwave and mmw images. Figure 3 shows an example of a mmw image of a perfectly reflecting model aircraft degraded by speckle. The image was formed at a wavelength $\lambda = 4$mm employing a scanned transmitter-receiver mode of holographic imaging in our Laboratory as described elsewhere [26].

Another example showing severe image degradation by speckle is shown in Fig. 4 which is a 90 GHz ($\lambda = 3.2$ mm) radar image of an M-48 tank [27]. It is clear from these examples of monochromatic mmw imagery that elimination of speckle can lead to dramatic improvement in image quality.

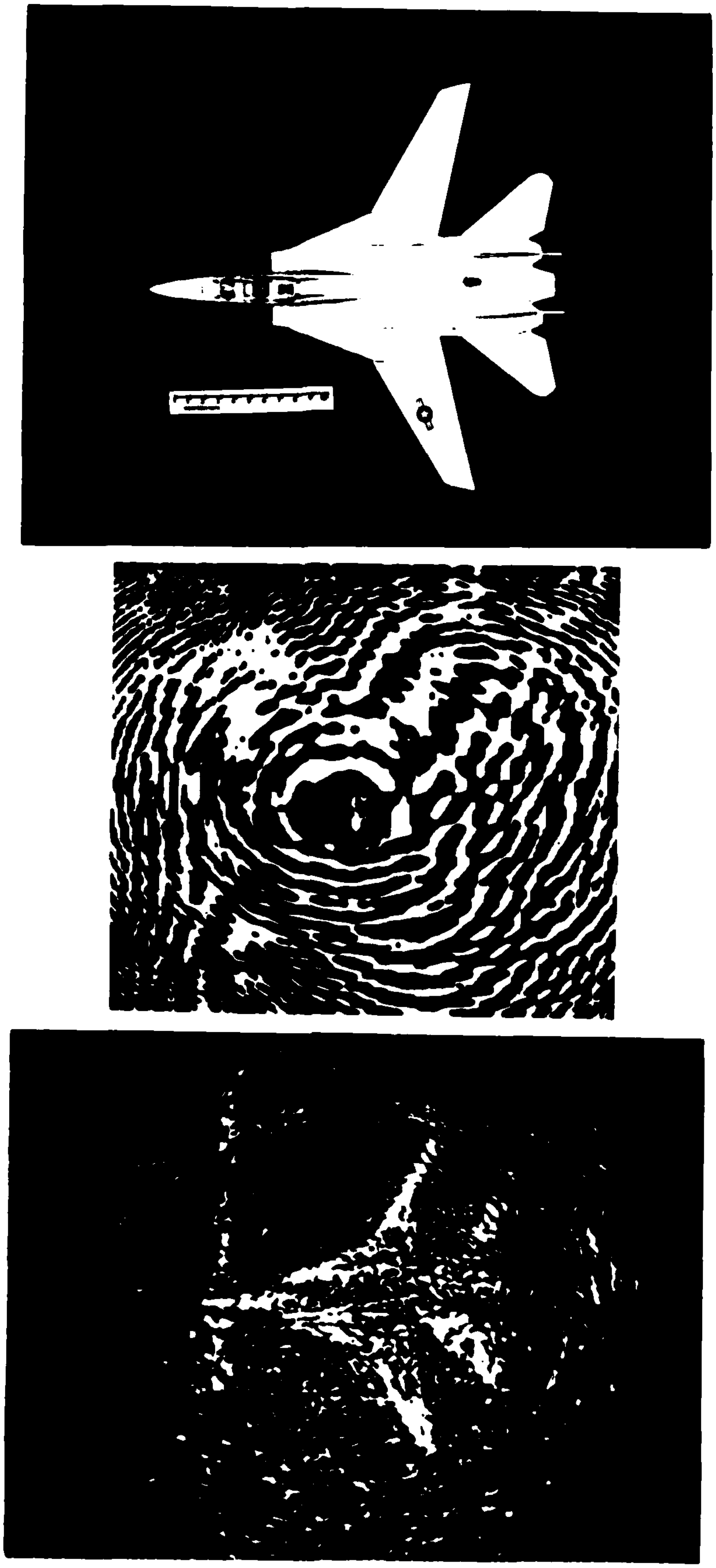

Fig. 3. 70 GHz (λ = 4.3mm) scanned T/R imaging of a 1:64 scale model of an F-14 aircraft. From top to bottom: object, hologram, and retrieved image degraded by speckle or coherent noise.

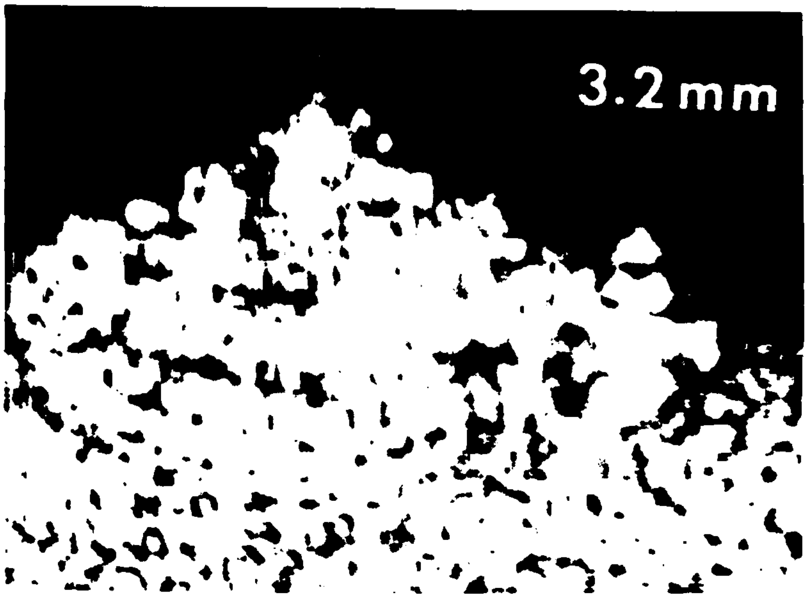

Fig. 4. 90 GHz (λ = 3.2mm) radar image of an M-48 tank showing deleterious effect of speckle. [From Ref. 27]

2.4 Speckle Reduction by Wavelength Diversity

Considerable progress in the understanding of speckle, its use, and its elimination has been achieved [24],[25], [28]-[32], since the advent of the laser when the observation of speckle and its related phenomena became a routine everyday occurrance. This work has resulted in good understanding of the statistics of speckle patterns formed in polarized monochromatic electromatnetic fields. These are shown to result from a classical random walk in the complex plane with the resulting irradiance fluctuations obeying a negative exponential law and the contrast of the speckle pattern, defined as the ratio of the standard deviation to the mean, being equal to unity [33]. Most methods for the reduction of speckle contrast [24],[25], [28]-[33] rely on either frequency diversity, spatial or angular diversity, or on polarization diversity all of which are automatically realized in wavelength and polarization diversity imaging. In particular the effect of wavelength diversity in suppressing speckle can be explained in terms of decorrelation of the speckle patterns at the various recording frequencies making thus the effect of speckle on the recorded data resemble that of random noise. It can be appreciated from this brief discussion of speckle that the wavelength and polarization diversity imaging method has inbuilt mechanisms for suppressing speckle noise. This leads us to expect that the reduction by speckle of the information content computed in eq. (33) should not be excessive. This speckle combating capability is one of the most significant features of λ and polarization diversity imaging allowing it to combine the best of two worlds, the world of incoherent imaging where speckle noise is nonexistent and the world of coherent imaging where sensitive detection techniques and versatile data acquisition and processing is available.

Our research program calls for closer examination of the effect of speckle noise on information content. Therefore to understand the role of wavelength diversity in suppressing speckle we consider an ideal λ-diversity imaging situation in which the $\overline{p}$-space of the object is accessed over a ball of radius $p_o = 2k_o$ by monostatic (β=0) multiaspect interrogation of a scattering object over an angular aperture of 4π[sr]. The volume of this ball represents then $H(\overline{p})$ of eqs. (10) and (14). i.e.,

$$H(\overline{p}) = \begin{cases} 1 & \ldots\ldots\ldots \quad p < p_o \\ 0 & \ldots\ldots\ldots \quad \text{elsewhere} \end{cases} \tag{34}$$

The 3-D impulse response or *point spread function* (PSF) obtained by 3-D Fourier transformation of eq. (34) is [34],

$$h(\overline{r}) = \frac{4\pi p_o^3}{(p_o r)^2} \{\text{sinc } (p_o r) - \cos (p_o r)\} \tag{35}$$

and is seen to be spherically symmetric. In eq. (35), $\overline{r}$ is a position vector in spatial domain. Similarly $H(\overline{p})$ for a spherical shell in $\overline{p}$-space of radius $p=p_o$ and unit strength can be described by [34],

$$H(\overline{p}) = \begin{cases} \dfrac{1}{4\pi p_o^2 \varepsilon} & \ldots\ldots\ldots \quad p_o < p < p_o + \varepsilon, \ \varepsilon << p_o \\ 0 & \ldots\ldots\ldots\ldots\ldots \quad \text{elsewhere} \end{cases} \tag{36}$$

which can be accessed by using monochromatic radiation at wavenumber $k_o = p_o/2$ and angular diversity of 4π[sr]. Fourier inversion of eq. (36) yields, the 3-D PSF,

$$h(\overline{r}) = \text{sinc } (p_o r) \tag{37}$$

Equation (35) can be utilized to determine the 3-D PSF of a spherical shell in $\bar{p}$-space extending from p_1 to $p_2 > p_1$ by simply replacing p_o in eq. (35) by p_2 and p_1 respectively and subtracting the two resulting expressions. This procedure can be also extended to evaluation of the PSF of a series of concentric $\bar{p}$-space spherical shells of arbitrary thickness determined by frequency diversity measurements extending over several available nonoverlapping frequency bands. Using this approach the PSF for monochromatic and broadband (wavelength diversity) imaging systems operating in different regions of the μwave and mmw spectrum were computed. The results are shown in Figs. 5 and 6. In Fig. 5(a), the monochromatic 18 GHz PSF (inner curve) and the broadband (2-18) GHz PSF (outer curve) are compared. Similar results are shown in (b) and (c) for 17 GHz versus (6-17) GHz and 40 GHz versus (2-40) GHz. The 3 dB width Δr_{3dB}, first zero crossing Δr_{zero}, and the first sidelobe level for all these cases are summarized in Table I. It is evident from the results shown that wavelength or frequency diversity results in a slight broadening of the PSF but has the important effect of suppressing the sidelobes of the PSF as compared with the monochromatic shortest wavelength (or highest frequency) in each case. The degree of sidelobe suppression is greater the smaller is the value of the lower bound on the frequency spectrum utilized. Of significance is the fact that the PSF for the (2-18) GHz and the (2-40) GHz cases is essentially unipolar, i.e., they are essentially positive real as for *incoherent* imaging systems that exhibit no speckle noise. Similar behavior is exhibited in Fig. 6 and Table II which present similar results for the PSF of several idealized monochromatic and broadband imaging systems operating in the (18-96) GHz range. The broadband (18-96) GHz is computed for three non-overlapping waveguide bands where travelling wave tube amplifiers are available. These results show that high resolution speckle free wavelength diversity imaging is possible through the use of broad frequency bands with small lower frequency limit.

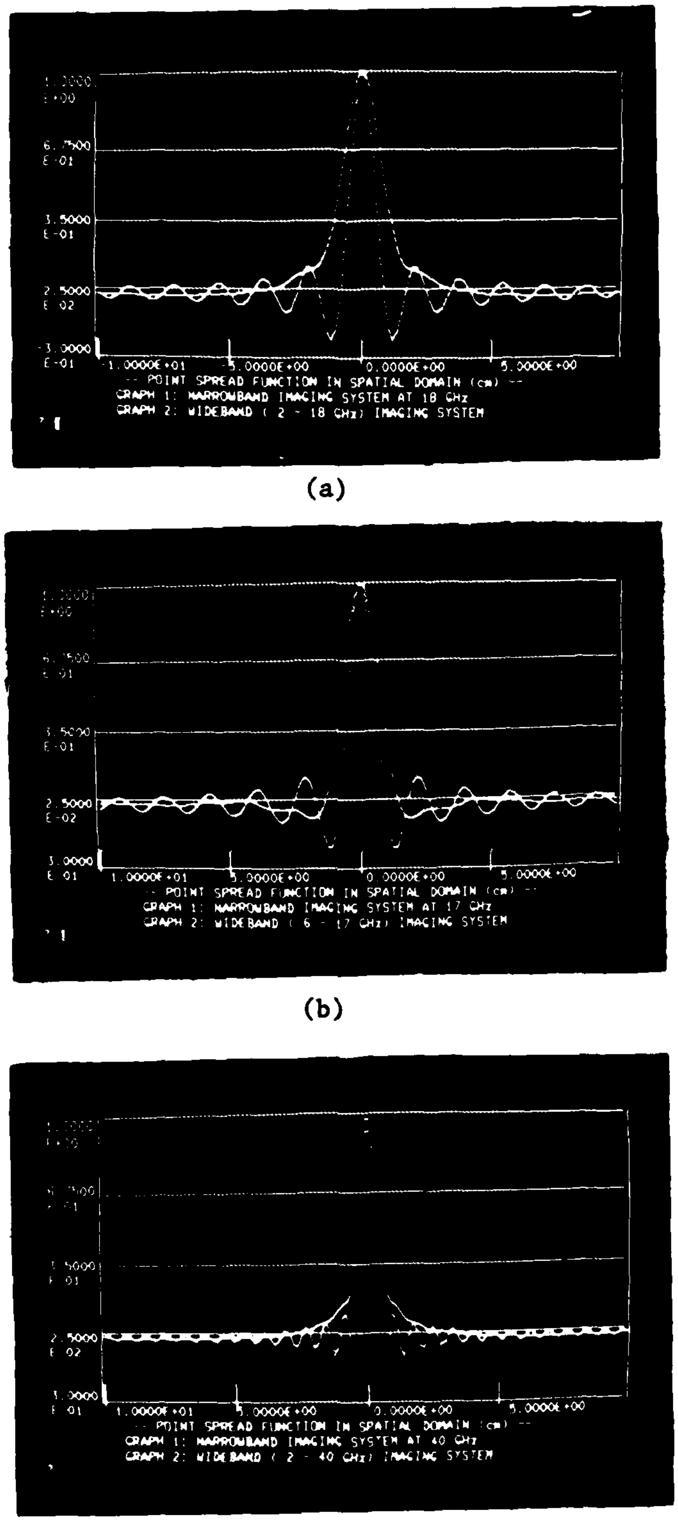

Fig. 5. Computed PSF of several idealized monochromatic and broadband imaging systems operating in the (2-40) GHz range.

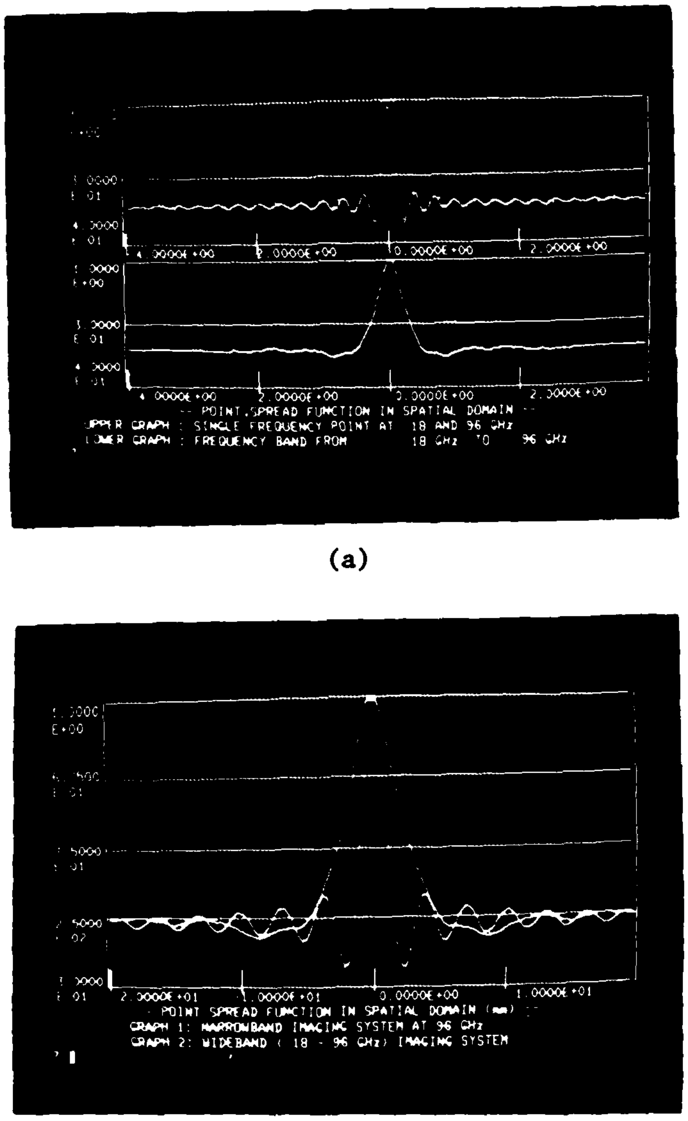

(a)

(b)

Fig. 6. Computed PSF of several idealized monochromatic and broadband imaging systems in the (18-96) GHz range. The (18-96) GHz range is covered in three nonoverlapping bands specified in Table II.

	18 GHz	(2-18) GHz	17 GHz	(6-17) GHz	40 GHz	(2-40) GHz
Δr_{3dB} [cm]	.74	1.27	.78	1.12	.33	.58
Δr_{zero} [cm]	1.67	9.13	1.75	2.68	.75	9.76
1st side lobe level [dB]	-13.4	-42.5	-13.4	-23	-13.4	-46

Table I. Comparison of PSF of several idealized monochromatic and broadband coherent imaging systems in the (2-40) GHz range.

	18 GHz	96 GHz	(18-96) GHz in Three Frequency Bands
			18 40 49.5 58 91 96
Δr_{3dB} [mm]	7.37	1.38	2.5
Δr_{zero} [mm]	16.67	3.125	10.7
side-lobe level [dB]			
1st	-13.4	-13.4	-23
2nd	-18	-18	-36.7

Table II. Comparison of PSF for several idealized monochromatic and broadband coherent imaging systems in the (18-96) GHz range.

Finally in this section it is worth pointing out that the PSFs of the solid sphere (ball) and the spherical shell sampling formats in $\bar{p}$-space described by eqs. (34)-(37) are nearly equal except for their "side-lobe" behavior. The similarity of the two PSFs becomes immediately evident when one applies the projection slice theorem (Appendix I) to the two sampling formats as elaborated upon in Appendix III. As long as the $\bar{p}$-space sampling format has always extended projections, as is true for the ball and the spherical shell where the projection areas are also equal the 3-D PSF will contain a sharp central peak. Accordingly if we were to access the $\bar{p}$-space of an object over a portion of the spherical shell (a cap) as is done in conventional monochromatic "sector scanning" or "rotational scanning" [41],[42] one can lose the 3-D imaging capabilities very rapidly as the depth of the cap diminishes (case of lensless Fourier transform hologram discussed in [42]). This is so because not all projections of a shallow cap are extended in area and therefore not all central slices of its PSF are of compact support (narrow extent). The above reasoning provides a new and general way of viewing imaging processes, whether broad-band or narrow, in such a way as to enhance our insight and understanding.

3. MEASUREMENT FACILITIES

Experimental investigation of 3-D λ and polarization diversity imaging requires facilities for precise measurement of the complex (amplitude and phase) frequency response of a scattering object for any desired range of aspect angles and state of polarization. For this reason we have put-together over the past few years a versatile measurement facility designed for microwave imaging studies that involve angular, spectral and polarization diversity in the (6-17) GHz range. The facility consists of a μwave (2-18) GHz *Automated Network Analyzer* (ANA) under DEC MINC 11/03 computer control. The systems allows measurement of the complex vector *scattering matrix* of scattering bodies situated in an *anechoic chamber* environment. The multiaspect object response is measured with the aid of a pair of monostatically or bistatically deployed stationary transmitting and receiving antennas by mounting the object on an elevation-over-azimuth positioner that can be made to change the aspect angles θ, ϕ of the object relative to the stationary antennas. Computer controlled selection of the frequency and polarization of illumination and of the object aspect angle are provided for. Digitally implemented data correction for system frequency response and chamber *clutter* are features that enhance accuracy and make such a facility a most powerful tool in the study of new aspects of *inverse scatering, holography* and *nondestructive evaluation*. Algorithms for precise determination of the range to the object from the collected data are needed to eliminate the range-phase factor from the measured data to obtain the frequency response of the object proper. Several such algorithms have been developed and are presently in use. This provides in effect a most versatile *Experimental Microwave Imaging and Measurement Facility* that enables the development of design criteria and optimal strategies for practical implementations of innovative radar imaging concepts that are based on findings derived from realistic data. The facility can be used to duplicate the performance of any existing or conceivable microwave imaging arrangement we wish to study. For example, by precise computer controlled angular positioning of the test object in front of translatable illuminating and receiving antennas the data collected in virtually <u>any existing or conceivable</u> imaging aperture configuration can be generated in the present operational band of (6-17) GHz range. This means that innovative μwave imaging concepts and modalities can be studied and evaluated without having to build an actual prototype. Modifications in concept and design, that would ordinarily be costly in the prototype case, are readily implemented in the facility because of its inherent versatility. Microwave imaging apertures of any extent, shape (planar, spherical or conformal), nature (i.e., degree of thinning, number of elements and their distribution), and mode of data acquisition (i.e., multiaspect monostatic or bistatic object interrogation) can thus be readily simulated. For example, the performance of a random and/or conformal imaging array can be simulated in the facility by deciding elevation and azimuth angles (θ,ϕ) of the object positioner with a random number generator in the controlling computer. This will furnish the angular randomness of the array elements as viewed from the object. Range variations due to random location of elements or due to their conformity to a shaped surface can also be simulated through the use of a programmable phase shifters placed in the transmitter or receiving arms of the ANA or better still by implementing the equivalent of this operation digitally directly on the p-space data obtained when using only angular randomness. In this fashion virtually every imaging array configuration whether it is intended for close-range or remote applications can be studied. This is a powerful capability whose value is amplified when we consider that because of its indoor nature the facility is available for use year-around.

The facility has also been used in the characterization of microwave components, devices, and antennas and can be used in conventional radar cross-section measurements. Detailed description of this facility and examples of its use in microwave imaging studies were given in earlier reports and publications [12],[35],[40].

4. PROGRESS DURING THE CURRENT PROGRAM YEAR

This chapter is devoted to describing the progress achieved to date in the various tasks of our research program in the course of the present program year. The material presented serves also to indicate future directions of research.

4.1 Projective Imaging of 3-D Object Detail From Realistic Data

A procedure for accessing the 3-D Fourier space of a conducting or non-dispersively scattering object by angular (aspect) and spectral diversity was developed and tested. Cost-effective data acquisition in the microwave regime was achieved making use of the concepts of chapter 1 by substituting spectral degrees of freedom for the more costly angular degrees of freedom set by the number of observation points defining the imaging aperture. A novel *target derived reference* (TDR) technique was utilized to generate a synthetic phase reference signal emanating from a point on the target achieving thereby a *3-D lensless Fourier hologram* recording arrangement that has many practical advantages. Application of the *projection-slice theorem*, derivable from the multidimensional Fourier transform, to the Fourier space volume accessed by measurement is shown to allow the retrieval of 3-D image detail. This can be achieved either tomographically in slices (or cross-sectional outlines) or as shown here in the form of a projection image of the 3-D object scattering function. Examples of microwave data acquisition, data normalization for an undesirable range-dependent-phase term via the TDR method, and image reconstruction are presented for complex conducting test objects. The results achieved in this task herald a new generation of high resolution 3-D imaging radars and can be applied in NDE (non-destructive evaluation), biomedical imaging, and remote sensing applications.

To simplify the description of the procedures utilized in this task we will confine the discussion to a cartesian component of the scattered vector field $\overline{E}$ described in Chapter 1 which we represent here by ψ. Then the component of the far field scattered by the object (under the physical optics and Born approximations) in the direction of the unit vector $\vec{1}_R$ due to plane wave illumination incident in the direction of the unit vector $\vec{1}_i$ can be expressed as,

$$\Psi(\vec{p},R) = \frac{jAke^{-jkR}}{2\ R} \int_{-\infty}^{\infty} \gamma(\vec{r}) e^{j\vec{p}\cdot\vec{r}} d\vec{r} \tag{38}$$

where using a slightly different notation than that used in Chapter 1 $\gamma(\vec{r})$ is taken here to represent any cartesian component of the vector object scattering function, $\overline{O}(\vec{r})$, which for conducting bodies of interest in this paper departs from zero only on the illuminated surface of the body; $\vec{r}$ is a 3-D position vector of an object point measured relative to a common origin in the object or its vicinity, $\vec{p} = k(\vec{1}_R - \vec{1}_i)$ is a 3-D position vector in Fourier space, $d\vec{r}$ is the differential element of integration, R is the distance between an observation point and the common origin and A represents the strength of the incident illumination. The integral in eq. (38) shows that far field measurements carried out for a sufficient range of values of $\overline{p}$ (that are realized by varying $\vec{1}_R$ and/or $\vec{1}_i$ (angular diversity) and by varying k (frequency or wavelength diversity)) permits accessing a finite region of the 3-D Fourier space,

$$\Gamma(\vec{p}) = \int_{-\infty}^{\infty} \gamma(\vec{r})\, e^{j\vec{p}\cdot\vec{r}}\, d\vec{r} = -j\,\frac{2\pi R}{Ak}\, e^{jkR}\, \Psi(\vec{p},R). \tag{39}$$

$\Gamma(\vec{p})$ can be regarded as a *3-D Fourier transform hologram* of the object scattering function component $\gamma(\bar{r})$. The size and shape of the accessed region of $\vec{p}$-space depends on the values of $\vec{p}$ used in the measurement. Equation (39) shows that extraction of $\Gamma(\vec{p})$ from the measured field $\Psi(\vec{p},R)$ requires knowledge of the range R from a reference point on the object to each observation point in order to carry out the required range-phase normalization. Equation (39) shows further that a diffraction and noise limited version of $\gamma(\vec{r})$ can be retrieved by 3-D Fourier inversion of the available $\Gamma(\vec{p})$. It is clear that the function $\Gamma(\vec{p})$ can in practice be determined over only a finite number of points defining the accessed volume of $\vec{p}$-space. We assume here without further elaboration that the $\vec{p}$-space sampling interval obeys the Nyquist criterion as discussed in Section 2.3 in order to avoid alising in the image reconstruction. Inversion of eq. (39) yields,

$$\gamma(\vec{r}) = \int_{-\infty}^{\infty} \Gamma(\vec{p}) e^{-j\vec{p}\cdot\vec{r}} \, d\vec{p} \qquad (40)$$

where $\vec{r}$ is now a 3-D position vector in image space.

Representing next the conjugate variables $\vec{r}$ and $\vec{p}$ by their cartesian components and computing the projection of $\gamma(\vec{r})$ on the x-y plane we obtain,

$$\gamma_{proj}(x,y) = \int_{-\infty}^{\infty} \gamma(x,y,z) \, dz = \int_{-\infty}^{\infty} dz$$

$$\iiint_{-\infty}^{\infty} \Gamma(p_x,p_y,p_z) e^{-j(p_x x+p_y+p_z z)} \, dp_x dp_y dp_z$$

$$= \iint_{-\infty}^{\infty} \Gamma(p_x,p_y,o) e^{-j(p_x x+p_y y)} \, dp_x dp_y \qquad (41)$$

which shows that the projection $\gamma_{proj}(x,y)$ of the scattering function on the x-y plane and a central slice $\Gamma(p_x,p_y,o)$ though $\Gamma(\vec{p})$, that is parallel to the projection plane are a Fourier transform pair as discussed earlier in Chapter 2. Because the Fourier transform conserves rotation, i.e., rotation of the object function results in identical rotation of the Fourier transform, the result in eq. (41) can be generalized to show that projections of $\gamma(\vec{r})$ in any given direction, other than the z direction chosen above, is the 2-D inverse Fourier transform of a central slice through $\Gamma(\vec{p})$ oriented normal to direction of projection.

By repeating the above arguments for each component $\psi(\bar{p},R)$ of the scattered vector field one can determine the vector image by superposition of the image components $\gamma(\bar{r})$ as described in Chapter 2 or alternately by superposition of the projection components $\gamma_{proj}(p_x,p_y)$ to obtain a vector image of slices through the vector scattering function.

Our experimental Microwave Imaging Facility [35] was employed in this task to access a slice in the 3-D Fourier space of complex shaped test objects. Based on the projection-slice theorem presented above projection images of the 3-D distribution of scattering centers on the test objects were formed utilizing the TDR method. Two test objects were used, a metalized 100:1 scale model of a B-52 aircraft with 79 cm wing span and 68 cm long fuselage, and a metalized 1:72 scale model of the space shuttle The test object is mounted on a computer controlled elevation-over-azimuth positioner situated in an anechoic chamber environment as shown in Fig. 7. Automated measurement of the scattered field over any band in the (6-18) GHz frequency range is provided by a coherent microwave measurement system consisting of a microwave sweeper and a coherent receiver as shown in Fig. 7(b). The minimum detectable signal of the receiver at 18 GHz is

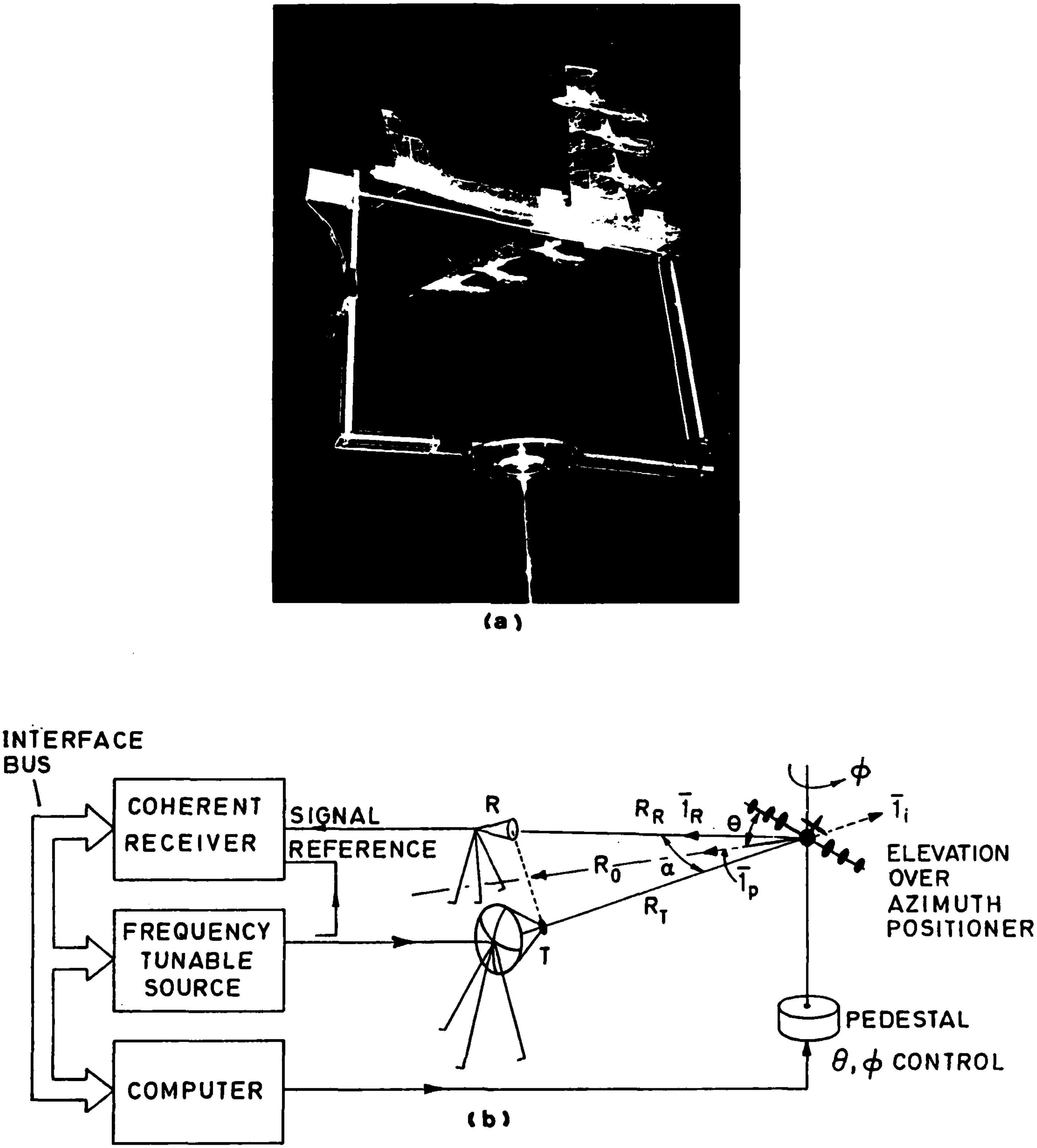

Fig. 7. Measurement System (Experimental Microwave Imaging Facility). (a) View of a test object mounted on the elevation-over-azimuth positioner. (b) Major components of measurement system.

approximately -110 dBm or 10^{-14} W while the dynamic range is of the order of 100 dB. These figures were achieved by using a (6-18) GHz GaAs FET pre-amplifier in the signal arm of the coherent receiver (not shown in Fig. 7(b)).

It is important to note that the $\bar{p}$-space accessed by rotating the object relative to a fixed T/R is identical to that accessed by spherical scanning the T/R around the fixed object over the same range of aspect angles. The measurement system of Fig. 7 is specifically configured to provide maximum versatility in the study of broadband microwave imaging, holography, and inverse scattering and in the evaluation of innovative radar imaging concepts. Plane wave illumination of the object at an irradiance level of about 10 mW/cm^2 is produced. Circularly polarized transmitting and receiving antennas are utilized and the amplitude and phase of the scattered field at the receiving antenna R is measured with the aid of a microwave network analyzer acting as a coherent receiver. Note the measurement configuration in Fig. 7 is nearly monostatic except for a slight spacing between the T/R antennas for the insertion of a microwave absorbing panel (not shown) intended to minimize direct leakage between antennas. In the arrangement shown $\alpha = 20°$ and $R_o \simeq 7$m. The entire measurement sequence consisting of angular positioning of the object in azimuth and elevation in increments of .7°, incremental frequency stepping over the (6-18) GHz in selectable frequency steps, digitization and storage of the amplitude and phase readings of the coherent receiver is carried out under control of a DEC Modular Instrumentation Computer, a MINC 11/03, which also performs the data reduction and display and all necessary image computations. The specified accuracy of amplitude and phase measured by the coherent receiver are ± 1.2dB and ± 4 degrees respectively. Settability in frequency tuning is possible to an accuracy of better than 1 MHz through precalibration with a microwave counter and least squares fit of a quadratic function to the measured frequency versus voltage transfer function of the sweep oscillator performed by the computer. Frequency incrementing by $\delta f = c/2L$ where L is a characteristic size of the scattering object is chosen to satisfy the Nyquist sampling criterion and avoid aliasing in the retrieved image. Assuming $L = 79$ cm for the B-52 a $\delta f = 86.6$ MHz was used requiring accordingly 128 frequency steps to cover the (6.1-17.1) GHz range employed in obtaining the data used below. A single Fourier space slice of finite extent was obtained for a fixed object elevation angle of $\Theta = 30°$ when the azimuth angle ϕ was altered between -45° to +45° relative to broadside orientation of the model (when the fuselage is perpendicular to the line bisecting the angle α in Fig. 7) in steps of .7° for a total of 128 angular looks. This arrangement was chosen to simulate the $\vec{p}$-space data that would be collected in the imaging geometries of a passing aircraft depicted in Fig. 8. For the value of $\alpha = 20°$ used in the recording geometry, the vector $\vec{p} = k(\vec{1}_i - \vec{1}_R) = 2k\cos\frac{\alpha}{2}\,\vec{1}p$ extends from $p_1 = 2k_1\cos\frac{\alpha}{2} = 503.25$ Rad/m to $p_2 = 2k_2\cos\frac{\alpha}{2} = 1402.5$ Rad/m in the direction of $\vec{1}p$ along the bisector of the angle α in Fig. 7. In this fashion the $\vec{p}$-space is accessed in a polar format consisting of 128 radial lines each corresponding to one value of ϕ covering an angular span of 90° with each line containing 128 data points for a total of 16,384 complex data points. Computer displays of $\mathrm{Re}\{\Gamma(\vec{p})\}$ over the accessed slice obtained in this fashion are shown later in Figs. 10, 12 and 13. The time required to obtain the slice data is of the order of 20 minutes. This includes measurement time and data correction time.

In practice the measurement system of Fig. 7 cannot measure $\Psi(\vec{p},R)$ of eq. (38) directly. Instead the measurement is distorted by undesirable effects of clutter and system frequency response. Clutter is an additive signal

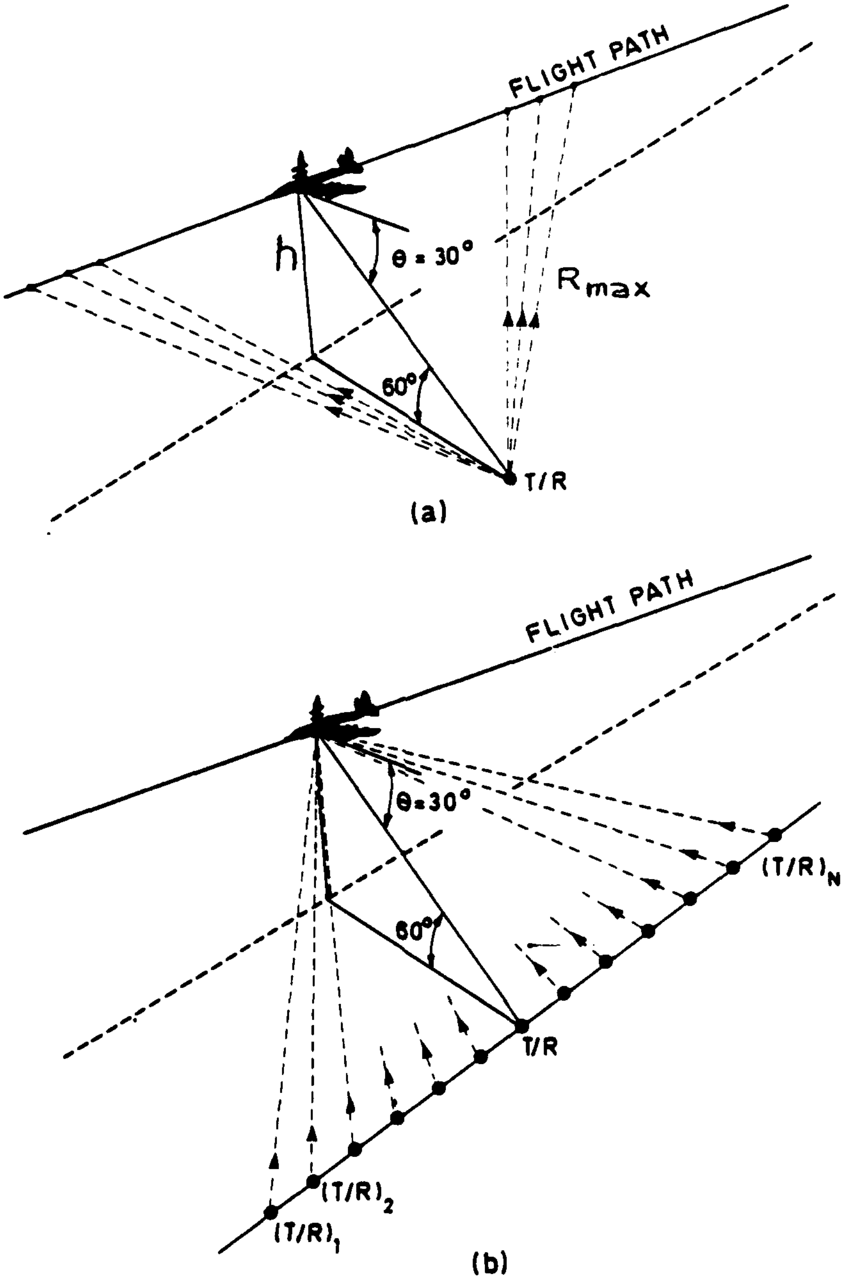

Fig. 8. Imaging arrangements equivalent to that of Fig. 7. (a) Target synthesized aperture or inverse Synthetic Aperture Radar arrangement. (b) Imaging radar network arrangement.

component caused by reflections from the microwave absorbing panels covering the chamber walls, floor, and ceiling, and for any other present items such as the object mount and positioner. Also included in clutter is any direct signal leakage from the transmitting to receiving arms of the measurement system as, for example, through antenna coupling. System response represents the combined multiplicative effect of the frequency response of all measurement system components such as antennas, cables, amplifiers, etc. which can modify the measured values of $\Psi(\vec{p},R)$. Error free determination of $\Gamma(\vec{p})$ requires, therefore, not only the phase-range normalization indicated in eq. (39), but also requires correction of the measured scattered field for clutter and system response. The most significant advantage of computer controlled automated microwave measurements, in addition to speed of data acquisition, is that such corrections can be carried out readily by the computer using algorithms that lead to the determination of $\Gamma(\vec{p})$ with an accuracy unattainable otherwise. One data correction procedure developed in our work and found to be quite effective enables the correction of the measured scattered field for both range-phase and system response simultaneously. The procedure uses the frequency response of a reference target of known linear phase dependence on frequency and of constant amplitude response. Both the conducting sphere and conducting cylinder satisfy this requirement over a wide range of bistatic scattering angles in their physical optics scattering regime where $ka>1$, a being the radius [36]. For both cases, the frequency dependence of the phase of the copolarized scattered field received at R relative to the phase of the transmitted signal at T can be represented by $\exp -jk[(R_T+R_R) - 2a\cos\alpha/2]$ where R_T and R_R are the distances between the phase centers of the transmitting and receiving antennas respectively and the center of the reference sphere or axis of the reference cylinder when either is used in place of the object in Fig. 7 [36]. The correction data for the results presented below were produced using a conducting cylinder as the reference target. The cylinder used was of diameter $2a = 7.5$ cm$>\lambda$ and length $\ell = 1$m$>>\lambda$. A quantitative description of the procedure is given next. Let,

$$\Psi_m(\vec{p}) = kAe^{-jk(R_T+R_R)}\;\Gamma(\vec{p})H(p)+C(p) \tag{42}$$

be the scattered field measured by the system of Fig. 7. Here A is a complex constant and H(p) and C(p) represent the multiplicative complex frequency response of the system and the additive clutter respectively. Note that H and C are functions of frequency alone though $p = 2k\cos\frac{\alpha}{2}$ and when polarization effects are taken into account that C(p) is also polarization dependent. Furthermore C(p) in eq. (42) contains implicitly the effect of the system response H(p) on the clutter measurement. The copolarized scattered field for a vertically oriented conducting reference cylinder whose axis coincides in Fig. 7 with the azimuthal axis of rotation is independent of aspect angle ϕ and is given therefore by,

$$\Psi_c(p) = kAe^{-jk(R_T+R_R)}\,e^{jk2a\cos\frac{\alpha}{2}}\;H(p)+C(p). \tag{43}$$

If the reference cylinder is positioned with its axis displaced by an amount a in range from the axis of azimuthal rotation of the pedestal, the measured field of eq. (43) becomes,

$$\Psi_r(p) = kAe^{-jk(R_T+R_R)}\;H(p)+C(p). \tag{44}$$

with the first term on the right hand side representing specular reflection at the leading edge of the cylinder which acts as a line scatterer positioned on the axis of azimuthal rotation. The copolarized scattered field of the displaced reference cylinder is seen to contain the required data correction terms; the range-phase term, the system response term and the clutter term. To effect data correction the clutter term C(p) is first measured by the system without any target in place and stored in computer memory. Then the reference cylinder is positioned as described above and the response (of eq. (44)) is measured and stored. The computer is then used to subract C(p) from the previously measured and stored object frequency response of eq. (42) and from the stored reference response of eq. (44) to finally obtain the required object response from,

$$\Gamma(\overline{p}) = [\Psi_m(\overline{p}) - C(p)]/[\Psi_r(p) - C(p)]. \qquad (45)$$

The preceeding procedure has been tested in our studies and found to provide good results. However, it is frequently not practical or possible to locate the reference target in place of the scattering object in order to effect data correction for range-phase and system response simultaneously as described above. This is particularly true when the object is remote as in actual radar imaging situations. A procedure different than that indicated by eq. (45) is then needed. Therefore a more practical method in which the system response and the range-phase are determined separately was devised and applied in obtaining the imaging results presented in this section. The method is novel in that it synthesizes a phase-reference point on the target realizing thereby all the advantages of a TDR [3]-[6]. It is based on utilizing the available measured multiaspect frequency response data of the scattering object to determine the total path length (R_T+R_R) between the phase centers of the transmitting and receiving antennas to a selected phase reference point on the object. Clutter is measured exactly as before, however, the reference target is utilized now only to determine the system response H(p). The path-length information for each "look" or viewing angle (aspect) of the object is obtained by Fourier inversion of the already available frequency response data after correcting it for clutter and system response. This provides the impulse response of the object for each viewing angle as a function of a spatial variable ξ proportional to ct, c and t being the velocity of light and time respectively. Because plane wave illumination is utilized, the resulting "spatial" impulse response represents essentially the geometrical projection of the visible scattering centers of the object, weighted properly by their scattering strengths, on a line in the $\overline{1}_p$ direction. With the impulse response information in hand, the location of the *scattering centroid** of the object on the ξ axis is determined for each viewing angle and then used to estimate the range information (R_T+R_R) as will be described below. The accuracy of this method for determining range information is well known and is given by $c/2\Delta f$, Δf being the width of the spectral window utilized in data acquisition [37]. The last step in data correction, namely the range-phase normalization, can now be carried out to yield the desired $\Gamma(\overline{p})$. This last operation is in effect equivalent to an alignment or coalescing of the positions of the scattering centroids for the various viewing angles into a single phase reference point on the object that represents a synthetic TDR.

---

* This often coincides with the location of a dominant peak in the impulse response when there is a dominant scattering center on the object.

To put the above remarks on a quantitative basis we write from eq. (43),

$$H(p) = \frac{1}{kA} e^{j\left(\frac{R_T+R_R}{2\cos\alpha/2} - a\right)p} [\Psi_r(p) - C(p)]. \tag{46}$$

All quantities on the right side of this equation are known (from clutter data and measurements with the reference cylinder) with the exception of (R_T+R_R) which we determine by Fourier inversion of the known quantity.

$$G(p) = \frac{1}{kA} [\Psi_r(p)-C(p)] = e^{-j\left(\frac{R_T+R_R}{2\cos\alpha/2} - a\right)p} H(p) \tag{47}$$

This inversion yields,

$$g(\xi) = \frac{1}{2\pi} \int G(p) e^{jp\xi} dp = \frac{1}{2\pi} h(\xi-\xi_c) \tag{48}$$

where $h(\xi)$ is the Fourier inverse of $H(p)$, and

$$\xi_c = (R_T+R_R)/2\cos\frac{\alpha}{2} - a \tag{49}$$

By taking ξ_c to equal the centroid of g (see Fig. 9) which is defined as,

$$\xi_c = \int \xi g(\xi)\, d\xi \Big/ \int g(\xi)\, d\xi \tag{50}$$

and equating eqs. (49) and (50) we can determine the range information (R_T+R_R) which can then be substituted in eq. (46) to yield the system response $H(p)$.

Having determined $H(p)$ we can find $\Gamma(\bar{p})$ from eq. (42) as,

$$\Gamma(\bar{p}) = \frac{1}{kA} e^{jk(R_T+R_R)} [\Psi_m(\bar{p}) - C(p)]/H(p) \tag{51}$$

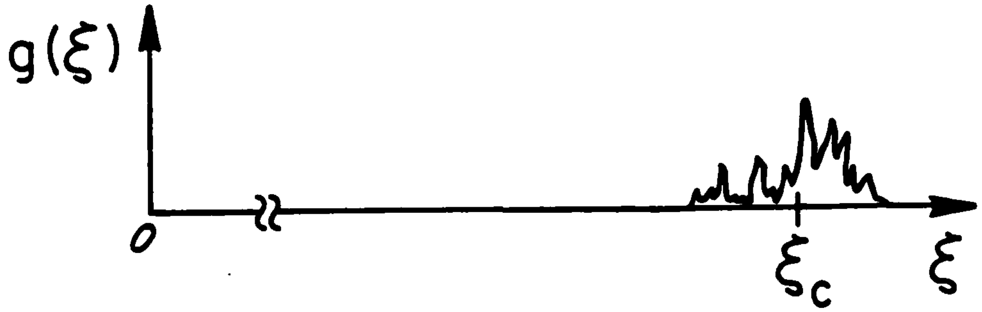

Fig. 9. Plane wave impulse response representation used in defining the scattering centroid ξ_c.

Again we note that all quantities on the right side of this equation are now known from measurements except for the range information (R_T+R_R) of the object which will be aspect dependent since the scattering centroid is aspect dependent. This term can be determined as before by Fourier inversion of,

$$Q(\bar{p}) = [\Psi_m(\bar{p}) - C(p)]/H(p) = e^{-jk\left(\frac{R_T+R_R}{2\cos\alpha/2} - a\right)p}\,\Gamma(\bar{p}) \qquad (52)$$

to first obtain the impulse response for each viewing angle and then to determine the distance of the scattering centroid for each look to find the corresponding (R_T+R_R) which can finally be used in eq. (51) to obtain $\Gamma(\bar{p})$.

An example of the $\theta = 30°$ slice of $\Gamma(\vec{p})$ of the B-52 test object extracted from the measured data by the above procedure is shown in Fig. 10(a). This represents the real part of the slice data as displayed by the computer on a high resolution CRT display. Fourier inversion of the data in this slice should yield, as explained previously a *projection image* representing the projection of the scattering centers of the object on a plane parallel to the plane of the $\vec{p}$-space slice. Digital Fourier inversion of the $\vec{p}$-space slice data requires its conversion first from the polar format (p,ϕ) in which it is originally acquired to a rectangular format (x,y) suited for application of the 2-D Fast Fourier transform. Conversion from polar to rectangular format was achieved by means of a weighted average of four nearest neighboring data points algorithm [38] represented in Fig. 11. The result is shown in Fig. 10(b). Typical interpolation time on the MINC 11/2 for the 16K complex data point of the $\vec{p}$-space slice was about 10 minutes. The result of applying the 2-D FFT to the interpolated data is shown in Fig. 10(c). This projection image is actually magnified in the vertical direction by a factor $1/\cos\Theta = 1.155$ in order to obtain a properly scaled projection image of the scattering centers as they would be seen in a bottom view of the B-52 shown in Fig. 10(d). The same scaling effect can also be achieved by scaling (contracting) the slice hologram of Fig. 10(b) in the vertical direction by the same factor $1/\cos\Theta$ after interpolation and then Fourier inverting. It is seen that prominent characteristic scattering centers of the B-52 e.g. engines, fuel tanks and fuselage are delineated clearly and in the correct geometrical relation and relative size to enable recognition and classification of the scatterer. The image resolution achieved is of the order of 2 cm and is in agreement with theoretical predictions [3]. The two vertical wedges appearing in Fig. 10(c) are the projection image of the vertical plexiglass arms supporting the test object (see Fig. 7(a)). Since the clutter information used in the data correction procedure is obtained for a single positioner orientation in ϕ, it will remove the effect of all cylindrically symmetric features of the positioner that do not change with ϕ from the image such as the vertical plexiglass tubing but not the vertical plexiglass arms since these lack

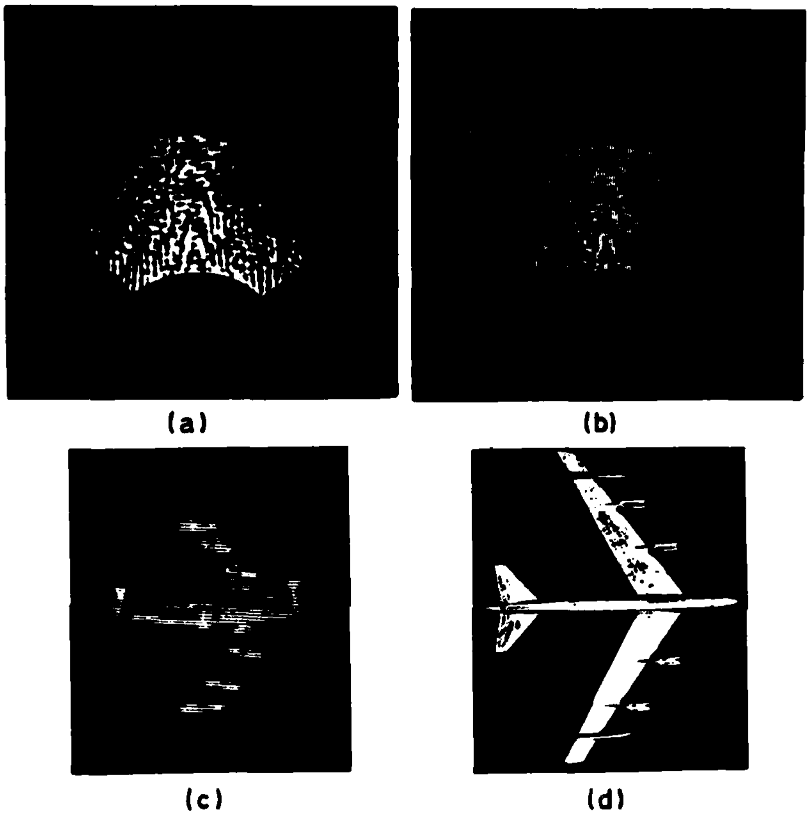

Fig. 10. Results of projection imaging of B-52. (a) Slice of 3-D Fourier space of object. (b) Same slice in rectangular format obtained by interpolation. (c) Projection image showing characteristic scattering centers identifiable in the pictorial view (d).

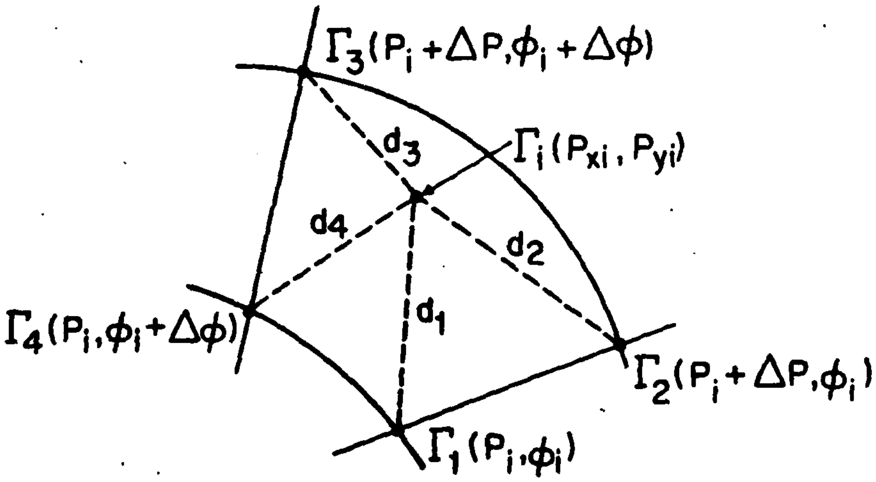

$$\Gamma_i(P_{xi},P_{yi}) = \frac{\frac{1}{d_1}\Gamma_1(P_i,\phi_i)+\frac{1}{d_2}\Gamma_2(P_i+\Delta P,\phi_i)+\frac{1}{d_3}\Gamma_3(P_i+\Delta P,\phi_i+\Delta\phi)+\frac{1}{d_4}\Gamma_4(P_i,\phi_i+\Delta\ )}{\frac{1}{d_1}+\frac{1}{d_2}+\frac{1}{d_3}+\frac{1}{d_4}}$$

Fig. 11. Interpolation algorithm [38].

cylindrical symmetry. The imaging of the plexiglass arms is also an indication of the effectiveness of the methods described here in imaging of composite (metalic/dielectric) bodies.

To reduce the effect of the positioner and test object mount evident in Fig. 10, the test object was mounted on a thin styrofoam support as shown in Fig. 12(z) and the imaging procedure outlined above was repeated. However this time the accessed $\overline{p}$-space slice of the B-52 was measured over a 90° angle covering a quadrant of a plane in front of the aircraft inclined at 30° below the nose of the aircraft. Circularly polarized plane wave illumination was utilized and the copolarized and cross-polarized components of the scattered field were measured. Photographs of the Fourier slices of $\Gamma(\overline{p})$ computed from the measured data for both polarization states are shown in (b) and (c) of Fig. 12. A photograph of the digitally retrieved image is shown in (d) of Fig. 12. This was obtained by incoherent superposition of the two polarization images to obtain a *polarization enhanced image*. Furthermore the known symmetrical nature of the target was exploited to form the left half of the image as a mirror image of the actual image retrieved from the data shown in (b) and (c) of Fig. 12. This is a simple but excellent example of the role of *a priori* knowledge, namely target symmetry in this case, in image enhancement. Further enhancement and restoration of the polarization and symmetry enhanced images obtained in this task will be considered in our future research work. The result of an identical imaging experiment of a second test object, a metalized 72:1 scale model of the space shuttle are shown in Fig. 13. The actual dimensions of this model are 48 cm body length and 33 cm wing span.

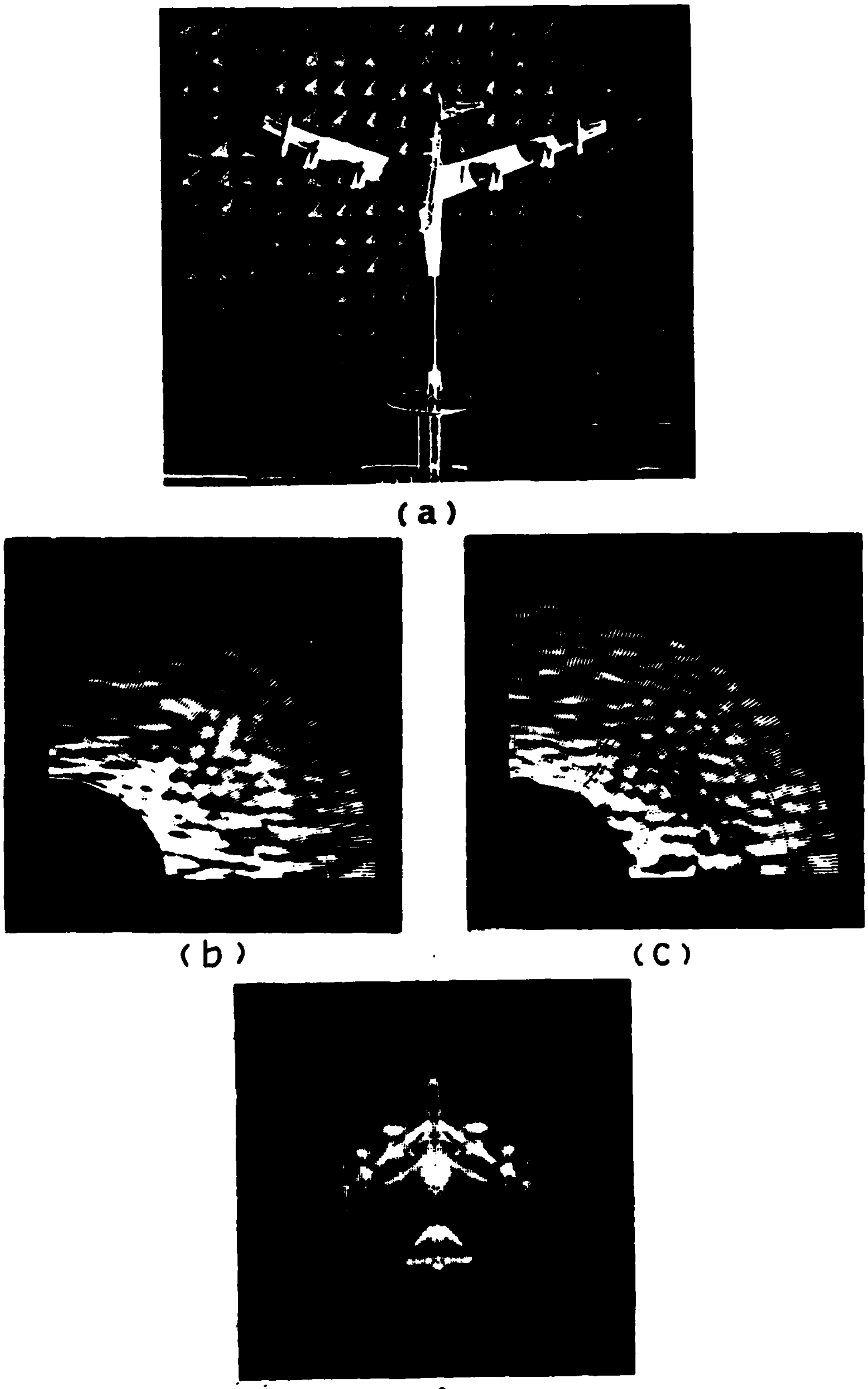

(a)

(b)

(C)

(d)

Fig. 12. Results of λ and polarization diversity imaging of a metalized 100:1 scale model of a B-52 shown in (a) mounted on an azimuth positioner. Co-polarized (b) and cross-polarized (c) p-space data, and polarization and symmetry enhanced retrieved image (d).

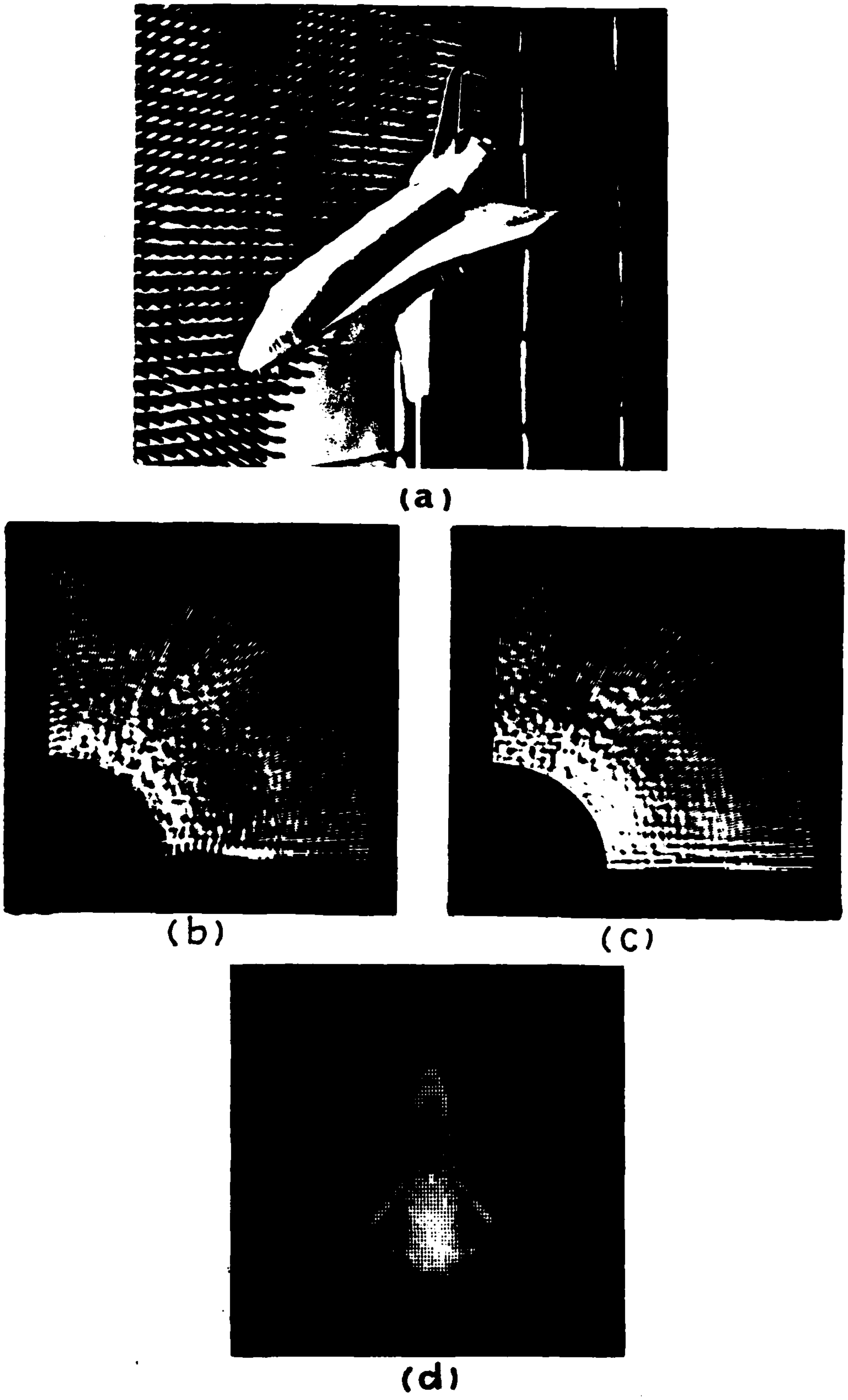
(a)
(b)
(C)
(d)

Fig. 13. Results of λ and polarization diversity imaging of a metalized 72:1 scale model of the space shuttle shown in (a) mounted on an azimuth positioner. Co-polarized (b) and cross-polarized (c) $\bar{p}$-space data, and polarization and symmetry enhanced retrieved image (d).

The results shown in Figs. 12 and 13 were obtained using an identical procedure for determining the multiaspect impulse response as in Fig. 10 with the exception of one added refinement. The procedure based on eqs. (51) and (52) was utilized as before to determine the scattering centroid of the object for each "look" or aspect as before, then each adjacent pair (in angle ϕ) of object impulse responses were cross-correlated and the displacement $\Delta\xi$ required to maximize the cross correlation was taken as a correction for the scattering centroid from a reference "look" with a prominent scatterer.

Several important conclusions and remarks can be drawn from the work described in this section.

(a) The principles and methods discussed show how to access the 3-D Fourier space of a nondispersively scattering object by angular and wavelength diversity. Although not specifically discussed in this paper, polarization diversity can also be employed to increase the amount of information in the accessed Fourier space.

(b) The accessing of the Fourier space is facilitated by the use of a novel synthetic target derived reference (TDR) technique whose advantages have been enumerated elsewhere [3]-[6] and whose effectiveness has been demonstrated here in the microwave regime. The TDR method is being used routinely in our tomographic and projective imaging of complex objects yielding unprecedented resolutions. The TDR technique results in a recording arrangement that yields what can be regarded as a 3-D lensless Fourier transform hologram.

(c) The first centimeter resolution microwave projection imaging of scattering centers of a complex conducting body from measured data is demonstrated. This is achieved by applying the projection-slice theorem to realistic microwave scattering data collected in our experimental microwave imaging facility.

(d) Projection imaging of characteristic highlights of the scattering centers of complex shaped objects of the kind employed in this study is shown to provide sufficient geometrical image detail to enable identification.

(e) Centimeter resolution is demonstrated through the use of frequency diversity in the (6-17) GHz range and angular diversity over $\pi/2$ in the data acquisition and by using digital image reconstruction. Excellent microwave image quality is obtained from data contained in a single slice of the Fourier space of finite extent accessed in an angular format of 128 equally spaced radial lines covering an angle of 90° with each radial line containing 128 complex data points. A study, not reported here, of the effect of angular aperture thinning and reduction, shows that reducing the number of radial lines (aspect angles) covering the 90° angular aperture from 128 to 64 hardly causes any noticeable change in image quality while narrowing the angular aperture to 45° does not degrade image quality to any significant degree as to render it unrecognizable.

(f) As can be seen by comparing Figs. 10, 12 and 13 with Fig. 4, the retrieved images are nearly free of the speckle noise that plagues conventional coherent imaging systems [24] and particularly microwave imaging systems. Speckle noise suppression is attributed to wavelength diversity which tends to make the impulse response of a coherent imaging system change from bipolar (i.e. with negative side lobes) to unipolar (see Section 2.3) making it thus behave like a speckle free incoherent imaging system [39].

(g) The concepts described and verified in this section show for the first time how a network of widely dispersed, extremely broadband, coherent radar stations can be used in a cooperative mode to produce 2-D projective images or 3-D tomographic images of distant aerospace objects with unprecedented resolution. This resolution can exceed the capabilities of optical imaging systems whose operation, unlike microwave systems, is severely hindered by atmospheric effects.

(h) The results presented here were obtained from data collected without having to maintain phase coherence from one angular frequency response measurement to another. This has important practical advantages when multiaspect interrogation of the scatterer with an array of broadband monostatic coherent transmitter/receiver elements is employed as the mode for data acquisition as envisioned in the proposed radar imaging network since it indicates that maintenance of phase coherence between the sources at the various stations is not required. This eliminates the need for reference signal distribution networks which are known to be a major obstacle in the realization of giant coherent microwave imaging apertures [5] because of economical and practical constraints on their implementation.

(i) Despite the fact that for the distance $R_T \approx 7$m and scatterer size L = .79m the receiving antenna position in Fig. 7 is hardly in the far field zone $(R>L^2/\lambda min)$ of the scatterer, high quality images were obtained using algorithms that stem from far field inverse scattering considerations. This seems to indicate that the imaging methods described here are applicable to intermediate range applications and possibly with some modifications to near field imaging situations.

(j) The Fourier space slice accessed by the measurements described in Fig. 10 using our experimental microwave imaging facility is identical to the $\vec{p}$-space that one might access in the inverse SAR geometry of Fig. 8(a) or the imaging radar network geometry of Fig. 8(b). This can readily be verified by drawing the $\vec{p}$-space sampling format for these equivalent geometries to find that they are identical since both access the $\vec{p}$-space of the scatterer over the same range of aspect angles one doing so sequentially in time as the scatterer progresses in its flight and the other acquiring the same data simultaneously. The questions of $\vec{p}$-space acquisition in the presence of scatterer motion and simultaneous interrogation where "cross-talk" can be a problem in the arrangement of Fig. 8(b) is being considered in our work and will be described in a future report.

(k) Customarily, the function $\gamma(\vec{r})$ is identified as the *characteristic function* of the scatterer defined as being unity within it and zero outside [7],[8]. The results presented here show that in practice γ can assume zero values on those parts of the scatterer's surface that are not seen by the system (i.e. do not scatter radiation in the direction of the observation point or points) such as the case of the flat portions of the wing sections and other gross detail in the example of the B-52 test object utilized in this work.

(l) Since scattering from a complex shaped object is polarization dependent, polarization selective measurements can readily be incorporated in the procedures described. This yields a wavelength and polarization diversity imaging method capable of providing more information about the scattering object.

4.2 Resolution Capability of the Experimental Microwave Imaging Facility

An estimate of the resolution of the experimental microwave imaging facility employed in the projection imaging study presented in the preceeding section was also obtained during this period. Two 1m long perfectly conducting rods 1.25cm in diameter and 2.5cm apart were used as the test target. The rods were mounted on the azimuth positioner (turn-table) off-axially as shown in Fig. 14. The distance between the axis of rotation to the central point

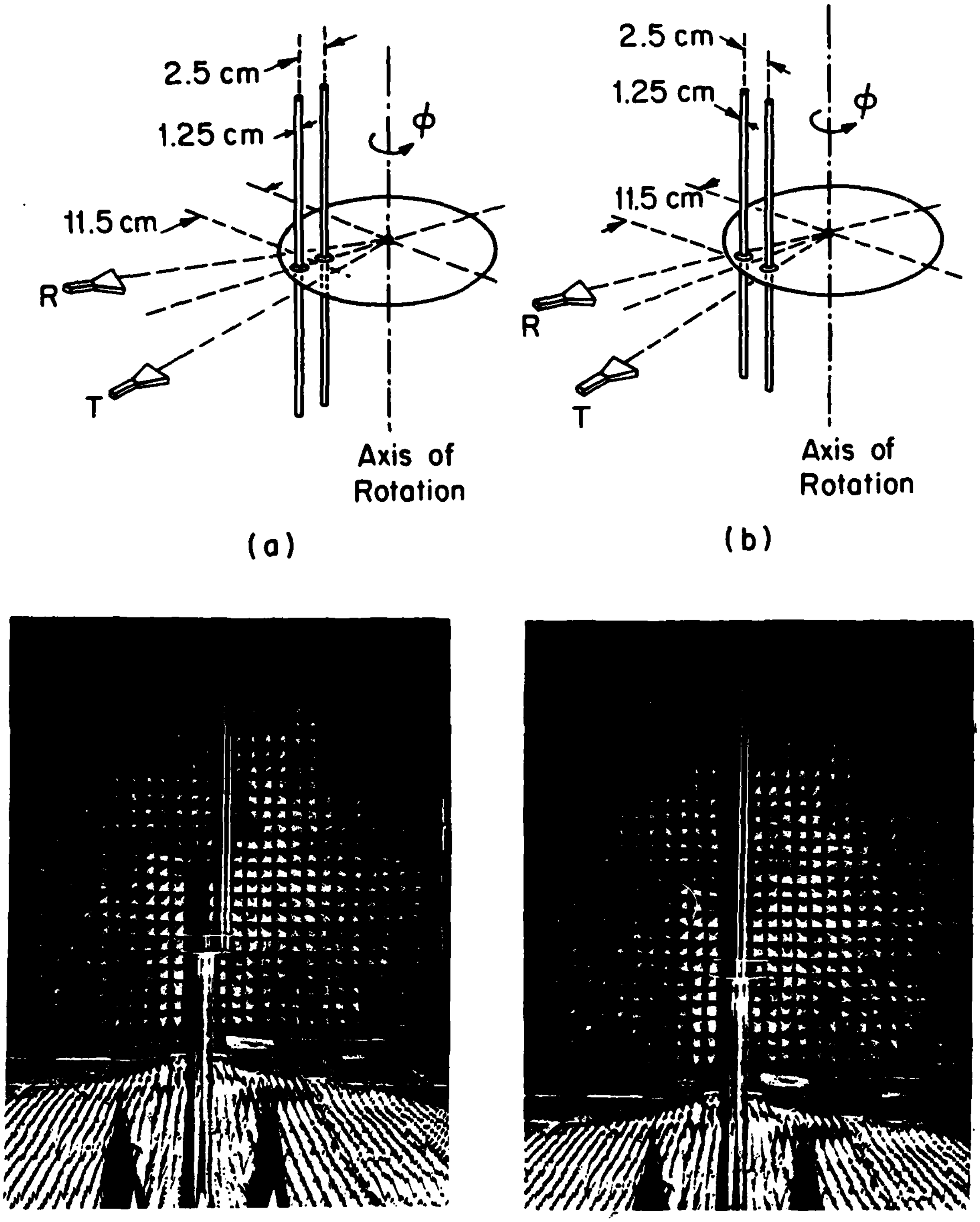

(a) (b)

(C) (d)

Fig. 14. Arrangement used in determining the resolution of the projection imaging capabilities of the experimental microwave imaging facility.

between the two rods was 11.5cm. To study longitudinal or range resolution the rods were mounted as shown in Fig. 14(a) and (c), while for studying transversal or lateral resolution they were mounted as shown in Fig. 14 (b) and (d). The Fourier space slices accessed for each case are shown in Fig. 15 (left). These were obtained using an angular aperture of 90° ($-45° \leq \phi \leq 45°$) and a (6.1 - 17.1) GHz spectral window. The digitally retrieved projection images for both cases are shown in Fig. 15 (right). These show the two rods to be clearly resolved in both azimuth and range indicating a resolution capability of the order of a centimeter or two. The images shown in Fig. 15 were plotted using the same scale used in plotting the images of the B-52 and the Space Shuttle presented in the preceeding section to enable direct comparison.

4.3 3-D Tomographic Reconstruction From Incomplete Fourier Space Data

Details of the work performed in this area are presented in Appendix III. The results presented indicate that accessing the 3-D Fourier space over closed or open surfaces that have extended 2-D projections in all directions is desirable. Considerations based on the projection-slice theorem show that for such $\bar{p}$-space sampling formats, the 3-D PSF will be as narrow as that resulting when the entire volume contained within the surface is accessed. However, since the number of receiver array elements needed to access a volume is always much larger than the number of elements required to access the containing surface or large portions thereof, considerable savings in cost can be achieved by adopting surface sampling. One example studied in our work so far is the circular array which accesses the p-space over the surface of truncated cone which satisfies this *finite extent projection criterion*.

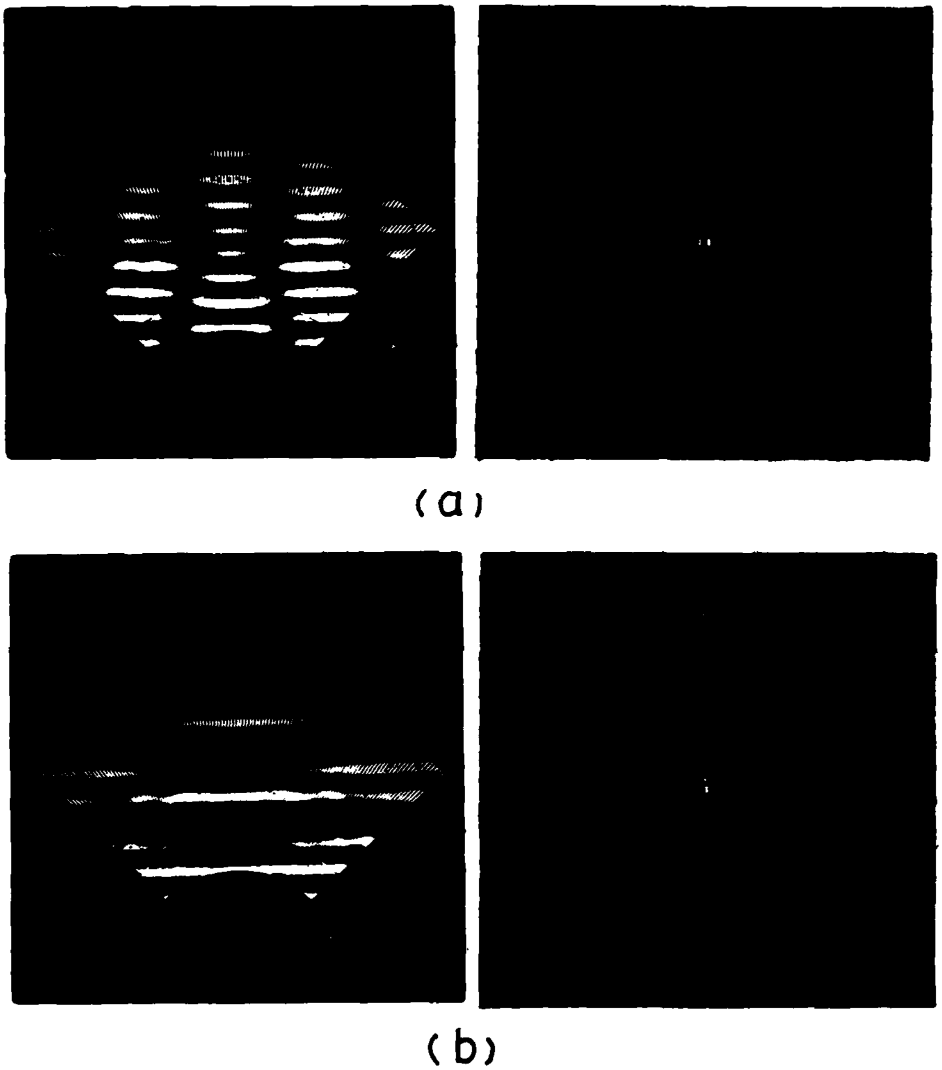

Fig. 15. Resolution capability of the experimental microwave imaging facility (a) Lateral resolution, (b) longitudinal resolution. Left: Fourier space slices. Right: retrieved projection images of the two-rod test target.

The above approach provides a useful criterion for determining optimal cost-effective $\bar{p}$-space sampling formats and the physical broad-band aperture geometries that give rise to them.

4.4 Tomographic Imaging of Dielectric Bodies

This task of our research program is concerned with the ability to image dielectric and composite bodies using the λ and polarization diversity imaging techniques developed in our work. There are several reasons for this concern. One is the fact that many aero-space objects of interest in remote imaging are composite in nature i.e., they contain conducting, semi-conducting, or dielectric parts. Another is the important role that can be played by an effective means of 3-D visualization in nondestructive evaluation (NDE). Microwave and millimeter wave (mmw) visualization of internal defects and flaws can be particularly important in materials that do not lend themselves to inspection by ultrasound techniques such as large solid propellant grains [43]. Preliminary results of (6-17) GHz microwave projection imaging of a dielectric test object consisting of two concentric cylindrical tubings of .3 cm wall thickness and inner and outer cylinder diameters of 4.750 cm and 29.70 cm respectively are given in Figure 16. The object was mounted on the elevation-over-azimuth positioner as shown in the top photograph of Fig. 16 and horizontal plane slices of its Fourier space where accessed over an azimuthal angle range of $0 \leq \phi \leq 360°$ for different values of elevation angle θ (= 0°, 20°, 30°). Since a single Fourier space slice is measured, the images retrieved from it by Fourier inversion will, in accordance to the projection-slice theorem, correspond to projections of the object scattering function on a plane parallel to the projection plane. These are shown in the second row of Fig. 16 for the three values of Θ chosen.

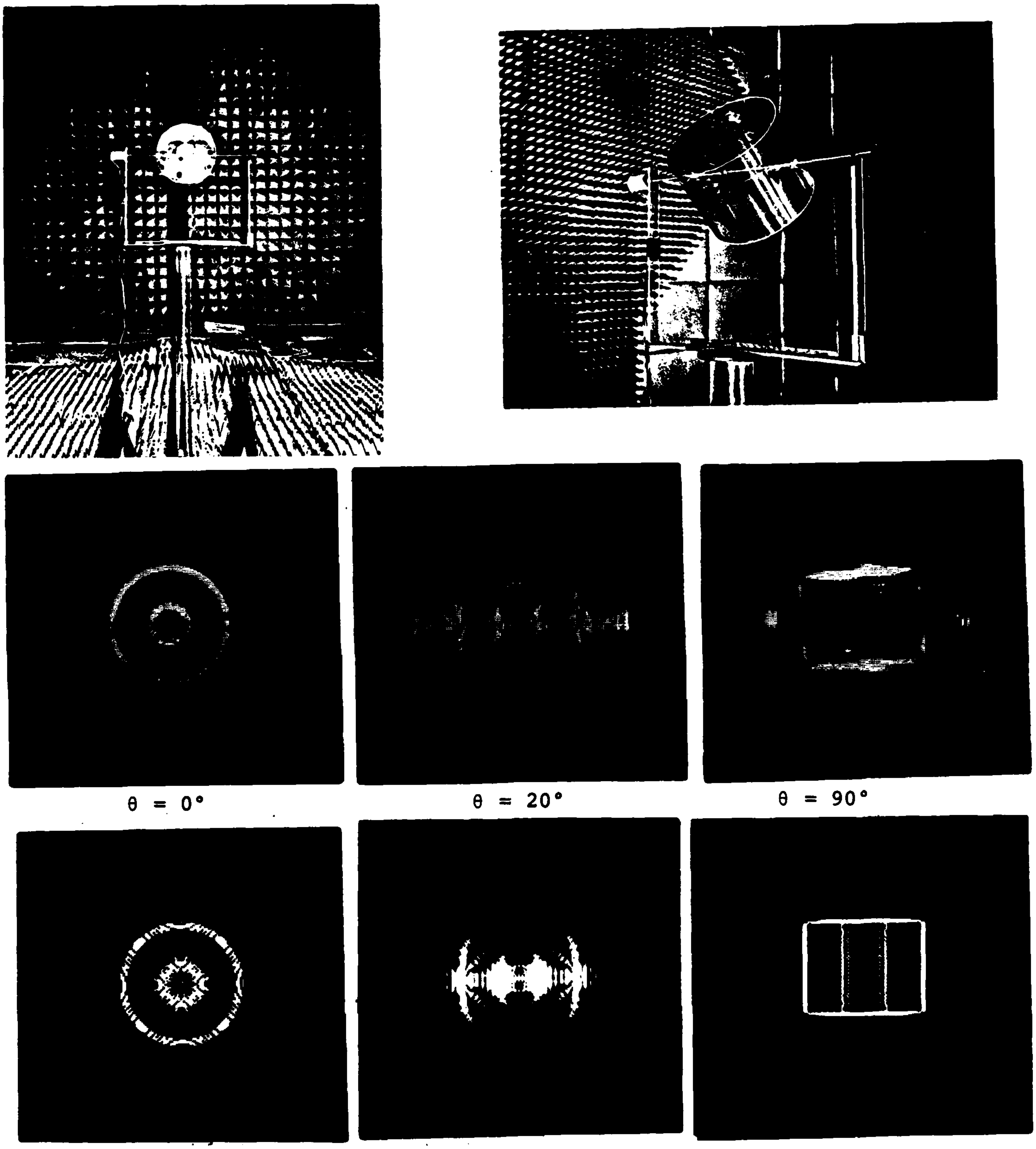

θ = 0°

θ = 20°

θ = 90°

Fig. 16. Results of microwave tomographic imaging of two concentric plexiglass cylinders shown in top row mounted on elevation-over-azimuth positioner. Second row - Digital reconstruction from Fourier space slices obtained using (6-17)GHz spectral window and 360° angular aperture. Bottom row - Digital reconstruction from equivalent computer simulation. θ is the angle between the cylinder axis and the vertical.

The projection images shown are seen to have adequate resolution for identification of gross detail but obviously not for the identification of other features such as possible voids, cracks, delaminations and other fine detail and imperfections of interest in NDE would require higher mmw resolutions. Also shown for comparison (bottom row) are the results of a computer simulation. It is seen that good agreement exists between the experimentally and numerically obtained results.

4.5 Design Considerations of Roof Experiment

The aim in this task of our research is to use the concepts of λ and polarization diversity imaging in an implementation of the *Inverse SAR* arrangement of Fig. 8(a) for the imaging of a passing aircraft using a modification of the measurement system of Fig. 7(b). The modification includes mounting a pair of transmitting and receiving antennas on a manually operated θ, ϕ positioner with which they can track the moving target. The design and construction of such a tracker has been completed during this period in our workshop. A pictorial view of the completed tracker with the two antennas mounted in position is shown in Fig. 17. The design incorporates angular position sensors which provide signals proportional to θ and ϕ with high accuracy that can be A/D converted and stored by the computer while the target is being tracked and interrogated (measurement of its frequency response repeatedly and rapidly over the desired spectral window). The nominal gains of the two parabolic dish antennas are about 30 dB and 40 dB respectively at 10 GHz. Using these values and eqs. (25) and (26) in which we assume, $P_T = 10W$ $\lambda = \lambda_{min} = 1.75$ cm, $\sigma = 10\ m^2$, $\beta = 10^4$ Hz, NF = 10 dB (noise figure of GaAs FET (6-18) GHz preamplifier) and ignoring transmission loss ($\gamma = 1$) we find that the maximum possible range R_{max} (see Fig. 8(a)) for maintaining a noise figure of 30 dB will be about 5 km.

If we assume that an angular aperture of 90° is to be utilized to gather data about the aircraft as depicted in Fig. 8(a), then the length of the observed flight path will be approximately 7 km and the closest distance of the aircraft will be 3.5 km. If we also assume realistically that the inclination angle $\theta = 60°$ then the altitude will be about h = 2.8 km or over 8000 feet which is a realistic figure for the flight patterns of aircraft passing in the air-

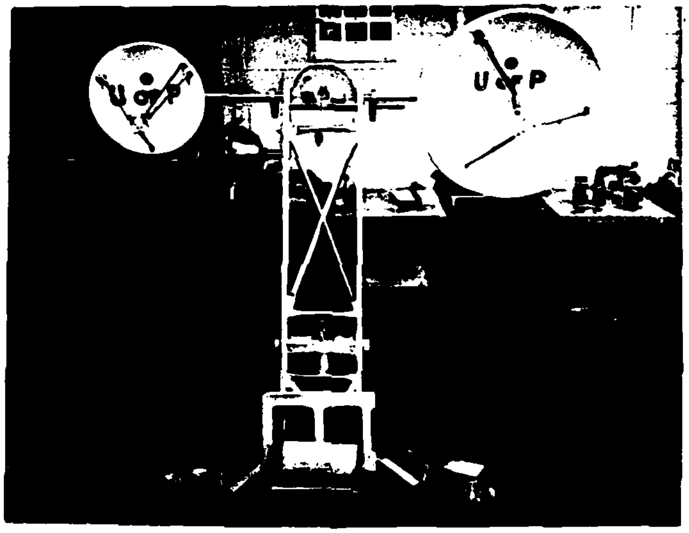

Fig. 17. Manual tracker for use in Roof Experiment.

space over the site for the experiment (the roof of the Moore School Graduate Research Center) on their way to land at the Philadelphia International Airport. According to the above figures the data acquisition time, assuming aircraft velocity of 100 m/sec, will be about 70 sec. or over a minute. The data volume we expect to gather during this interval is determined next using angular and spectral sampling considerations as discussed next.

If the lateral spacing between two extreme scattering centers on the object is L then the finest angular detail in its angular scattering pattern will be $\delta\theta = \lambda_{min}/L$ where λ_{min} is the shortest wavelength in the spectral window utilized. This value determines the angular sampling interval of the scattering pattern required in order to avoid azimuthal undersampling and image degradation due to aliasing. For the scale model of the B-52 test target utilized in our studies L is of the order of 80 cm and $\lambda_{min} \simeq 1.75$ cm ($f_{max} \simeq 17$ GHz). Therefore we find $\delta\theta \simeq 2.2\ 10^{-2}$ Rad $\simeq 1.3°$. The angular apertures employed in imaging this test target must therefore be sampled (angularly) at intervals of $\delta\theta = 1.3°$ or less. In the results presented in Section 4.1 for the B-52, the 90° angular aperture employed was sampled at intervals $\delta\theta = 90°/128 \simeq .73°$ which clearly satisfies the angular sampling requirement.

As mentioned earlier in Section 4.1 we have reduced the number of "looks" used from 128 to 64 i.e., to $\delta\theta = 1.46°$ and found that the retrieved image quality is virtually unchanged in agreement with theoretical predictions. Further angular thinning to 32 "looks" produce slight aliasing effects however the image remains recognizable.

These considerations as applied to the *Roof Experiment* (where it is intended to image a passing aircraft) mean (see also Appendix IV) that for a realistic aircraft size L = 50 m and λ_{min} = 1.75 cm, $\delta\theta$ will be of the order of 3.5 10^{-4} Rad or .2°. A 90° angular imaging aperture synthesized in time by the aircraft motion will therefore require about N_θ = 450 "looks" to angularly sample the aircraft scattering pattern. Each look will contain N_f frequency samples determined by the frequency sampling intervals $\Delta f = c/2L$ required to avoid aliasing in range as discussed earlier (see Section 4.1). For the spectral window of Δf = (6 - 17) GHz we find $N_f = \Delta f/\delta f = 11\ 10^9/3\ 10^6 \simeq 3.7\ 10^3$ frequency steps are required. The total number of angular and spectral samples that need to be gathered is therefore,

$$N = N_\theta \times N_f = 450 \times 3.7\ 10^3 = 1.67\ 10^6 \qquad (53)$$

Each sample point will consist of 4 data points, two for the complex field, two for the elevation and azimuth angle of the aircraft bearing. Therefore a total of 6.68 MB of data needs to be collected and stored in the computer in such an experiment. This considerable increase in the number of data points (as compared for example to the number encountered in the anechoic chamber imaging experiment of the B-52 test model) would require about ten fold increase in the storage capacity of the MINC 11/03 computer. This can readily be done by upgrading the DEC MINC 11/03 to a MINC 11/23 with the aid of an available upgrading kit, an additional 128 KB MOS memory card and a dual RL102 disc memory of 10 MB.

Because the target in this experiment is moving, we are unable to use directly the *static mode* (frequency stepped mode) of frequency response measurement developed and utilized in our anechoic chamber imaging studies described in Section 4.1 where the object was stationary during data acquisition. Instead a fast *dynamic mode* of data acquisition that can function in the presence of object motion must be developed and utilized.

We have shown [40] that such a dynamic scheme can be realized by utilizing frequency swept illumination instead of frequency swept illumination and by measuring the instantaneous frequency of the complex envelope of the coherently detected back scattered signal. For this case of frequency swept illumination of an object moving with constant velocity $\bar{v}$ the complex envelope of the scattered wavefield synchronously detected at a monostatic T/R station is shown [40] to be given by,

$$\psi(t) = \frac{E_o^2 \, e^{j\phi_o}}{4\pi R_1} \, |\Gamma \;\; (\bar{p}(t))| \, e^{j\phi(t)} \tag{54}$$

where for the practical case of $\bar{v}\cdot\bar{1}_{R_1} \ll c$ (i.e., object velocity is low compared to that of light) and for sweep duration T > 1 msec

$$\bar{p}(t) = \frac{2}{c}\,(\omega_1 + \gamma t)\,\bar{1}_{R_1}, \tag{55}$$

$$\phi_o = \frac{2\omega_1}{c}\,R_1 + \frac{\pi}{2} \tag{56}$$

$$\phi(t) = \mathrm{Arg}\,\Gamma(\bar{p}(t)) - at - bt^2 \tag{57}$$

where

$$a = \frac{2\omega_1}{c}\,\bar{v}\cdot\bar{1}_{R_1} + \frac{2\gamma}{c}\,R_1 \tag{58}$$

and

$$b = \frac{4\gamma}{c}\,\bar{v}\cdot\bar{1}_{R_1} \tag{59}$$

Here ω_1 is the initial frequency of the sweep, γ is the sweep rate, R_1 is the initial range to the object and $\bar{1}_{R_1}$ is a unit vector in the initial bearing direction. The instantaneous frequency of the complex envelope is,

$$\Omega(t) = \frac{d\phi}{dt} = \frac{d}{dt} \text{ Arg } \Gamma(\bar{p}(t)) - (a + bt) \tag{60}$$

This part of our research calls for measuring the instantaneous frequency $\Omega(t)$ over the interval $0<t<T$ with the aid of a suitable frequency discriminator, digitized and stored in our MINC 11 computer where a straight line fit of the data will be computed from which the values of a and b will be determined. Because of the large number of data points involved in each frequency sweep, the straight line fit is expected to be excellent leading to highly accurate estimates of a and b. With the values of a and b known, we can: (a) use eqs. (58) and (59) to determine the initial range R_1 and range rate $\bar{v}\cdot\bar{1}_{R_1}$ and (b) use eq. (60) to determine $\frac{d}{dt}$ Arg $\Gamma(\bar{p}(t))$ which can be numerically integrated between t=0 to t=T to yield Arg $\Gamma(\bar{p}(t))$.

By following this procedure and measuring the magnitude $|\psi(t)| = E_o^2|\Gamma(\bar{p}(t))|/4\pi R_1$ of the complex envelope we will be able to determine the required Fourier space data $\Gamma(\bar{p}(t))$ in both amplitude and phase.

A wide control over the values of a and b is available through the sweep rate $\gamma = (\omega_2 - \omega_1)/T$ which can be altered to make the initial frequency a and the final frequency a + bt fall within the bandwidth of the available frequency discriminator. Work is in progress to convert the phase measurement capabilities of our microwave network analyzer to a frequency discrimination mode by applying the received signal to the reference and test ports through two unequal lengths of coaxial cables which introduce a phase difference that is a linear function of the frequency of the incoming signal.

Other dynamic frequency response measurement approaches such as measuring the group delay of the backscattered signal as a function of frequency and a study of the feasibility of phase-locking the local oscillator of the network analyzer to the carrier in the incoming signal are also being considered.

4.6 Projection Imaging of Incoherent (Noise-Like Sources)

In earlier analysis we showed that the concept of 3-D tomographic imaging by wavelength diversity is extendable to incoherent radiation and thus to thermally emitting objects [12]. Verification of this concept can lead to true 3-D passive imaging (radiometry or thermography) with important implications in radio-astronomy, passive surveillance and remote sensing.

We have shown, [12], that spectrally selective cross-correlation measurements or equivalent cross-spectral density measurements of the random wavefield emitted by a 3-D incoherent source of brightness distribution $b(\overline{r})$ can be employed to access the 3-D Fourier space $B(\overline{p})$ of the emitter where $\overline{p} = k(\overline{1}_{R_1} - \overline{1}_{R_2})$. $\overline{1}_{R_1}$ and $\overline{1}_{R_2}$ being unit vectors in the directions of the transducers used to sense the field and k the wavelength (central wavelength of the congruently tuned filters used to achieve spectral selectivity in the correlator arms).

Successful verification of the concept was achieved recently employing acoustic noise emission rather than microwave emission because of easier and less costly implementation. Because of the large ratio of velocity of light to velocity of sound ($\approx 10^6$) the same wavelength ranges of interest in incoherent microwave frequencies can be achieved with sound spectra in the KHz range. This fact was employed to form *correlograms* of a 3-D spatial distribution of acoustic sources emitting noise in the (.6 - 13.5) KHz range and by an automated spectrally selective cross-correlation measurement arrangement described earlier [40]. The correlograms were treated as wavelength diversity holograms and employed in digital or optical image reconstruction schemes to form the first 3-D images of the incoherently emitting objects obtained in this fashion. Present efforts are also addressing the question of rapid data acquisition, rapid determination of cross-correlation and resolution enhancement.

Pictorial views of the measurement system are given in Fig. 18. The 3-D noise emitting object, shown in Fig. 18(b), was realized using a 3-D formation of five acoustic tweeters excited from independent random noise generators in the (.6 - 13.5) KHz range. The tweeters' assembly is mounted on an azimuthal positioner that is used to change their azimuthal angle ϕ relative to the sensors. The random wavefield produced was transduced at two points in space separated as seen from the object by angle $\theta \simeq 45°$ with the aid of two condenser microphones and the cross-spectral power density of their outputs was measured and recorded.

The correlogram recorded when only two of the five tweeters, indicated in the top view given in Fig. 19(a), were excited are shown in Fig. 19(b) and (c). Figure 19(b) is the real part of the correlogram as recorded by changing ϕ in Fig. 19(a) by 180° and plotting the measured cross-spectral density radially over a range equivalent to the (.6 - 13.5) KHz spectral window utilized. The correlogram consists of 196 radial lines each consisting of 48 frequency points. A digitally interpolated version of this correlogram as obtained by the four-nearest-neighbors algorithm of Fig. 11 is shown in Fig. 19(c). The patterns in Figs. 17(b) and 17(c) represent essentially a slice in the Fourier-space $B(\overline{p})$ of the object. Therefore in accordance with the projection-slice theorem, Fourier inversion of the data in this slice should yield a projection image

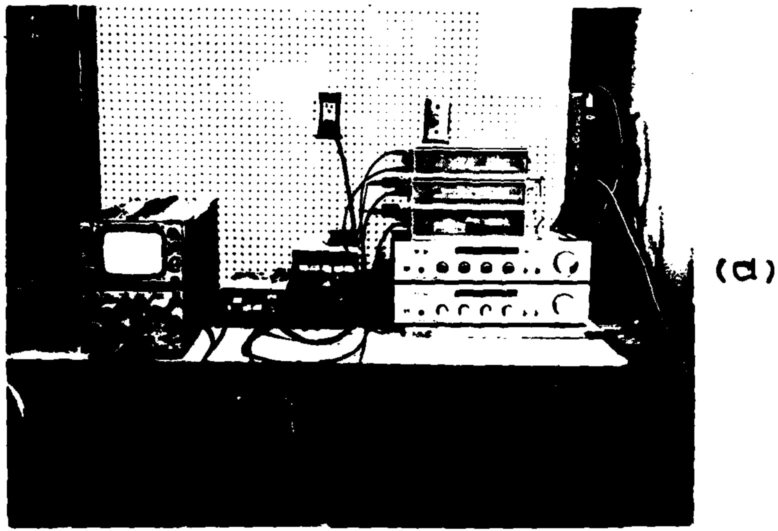

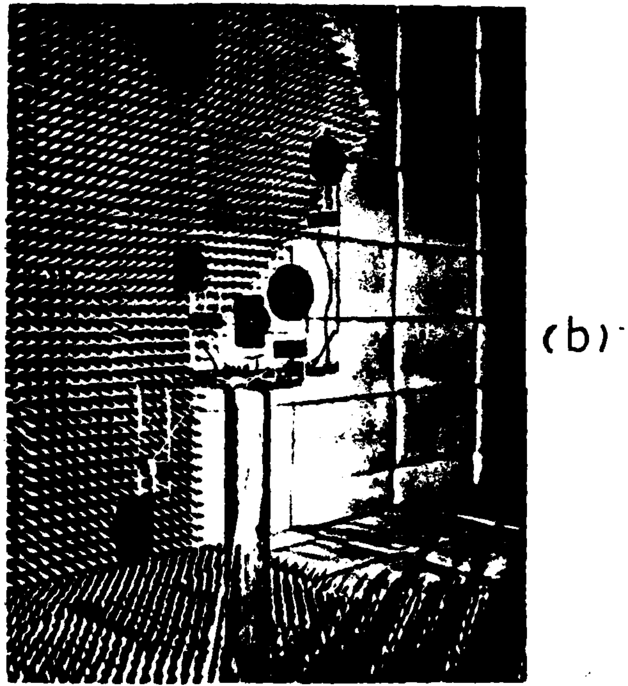

Fig. 18. Pictorial detail of measurement system employed in accessing a slice of the 3-D Fourier space of an incoherent 3-D acoustic source. (a) Instrumentation including amplifiers, programmable delays and multiplier. (b) View of 3-D distribution of five acoustic noise emitters (tweeters). (c) View of one of the two condenser microphones used for sensing the random acoustic field in the (.6 - 13.5) KHz range.

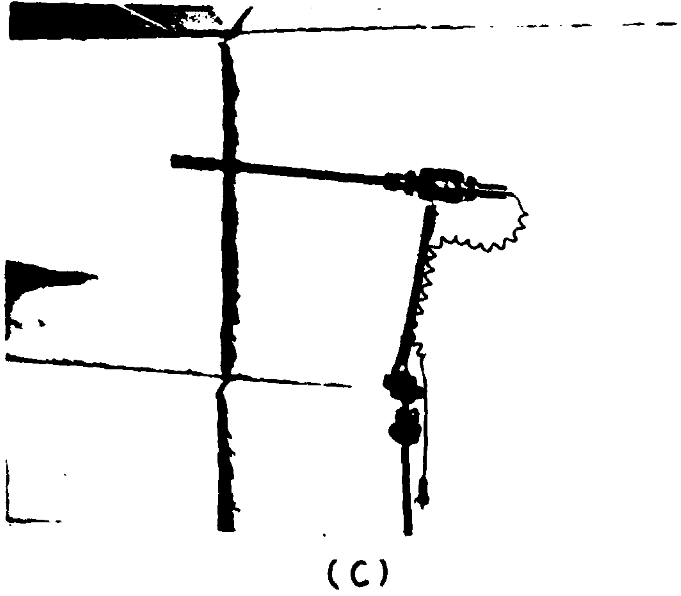

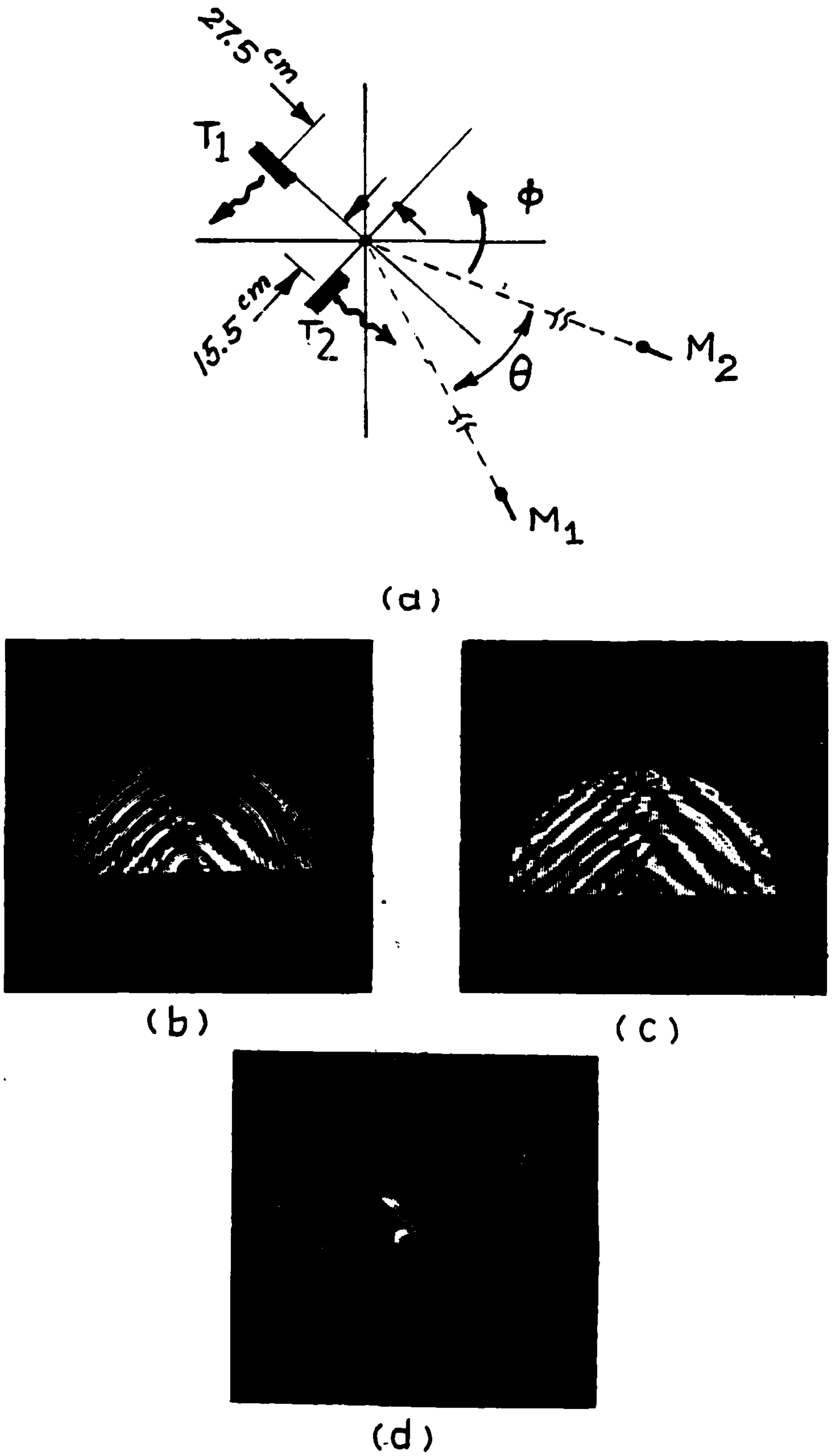

Fig. 19. Results of the first correlation imaging experiment of two acoustic noise emitters (tweeters) in the (.6-13.5) KHz range. (a) Top view of source geometry (T_1 and T_2) relative to transducer microphones (M_1 and M_2). (b) Real part of *Correlogram* in polar format and (c) Rectangular format. (d) Retrieved projection image.

of the brightness distribution of the source as projected on a plane parallel to that of the slice. The results of 2-D digital Fourier inversion of the correlogram slice of Fig. 19(c) is shown in Fig. 19(d). This preliminary result represents the first successful experimental verification of the concept of projective imaging of 3-D detail of an incoherently emitting object employing spectrally selective cross-correlation measurements or equivalent cross-spectral density measurement. The results pave the way to true 3-D tomographic imaging of such objects and raise intriguing questions on the 3-D object information content in random fields produced by thermally emitting objects.

4.7 Real-Time 3-D Image Reconstruction and Display

The objective of this task of our research is to study and develop methods by which true 3-D image reconstruction of the scattering centers of an object can be obtained and in real-time. In this fashion one would achieve the full potential of the 3-D imaging capability of λ and polarization diversity imaging and thus exploit fully the power of the human eye-brain system in cognition and identification. The advantages of a true 3-D image display are best appreciated when the number of visible scattering centers is small or when the scattering centers are closely packed. An example illustrating this point is given in Fig. 20 where two drawings of a cubical formation of eight point scatterers are given. In one, Fig. 20(a), a perspective view of the scatterers is given with depth cues being provided by adding the joining lines shown. These lines furnish the observer with an "impression" of a cubical formation. In Fig. 20(b) the same scatterers are redrawn but with the lines removed which makes the recognition of a cubical deployment not that obvious. If however the eight point scatterers in Fig. 20(b) are shown to an observer in a true 3-D representation, recognition of the cubical deployment will be immediate because of the introduction of true

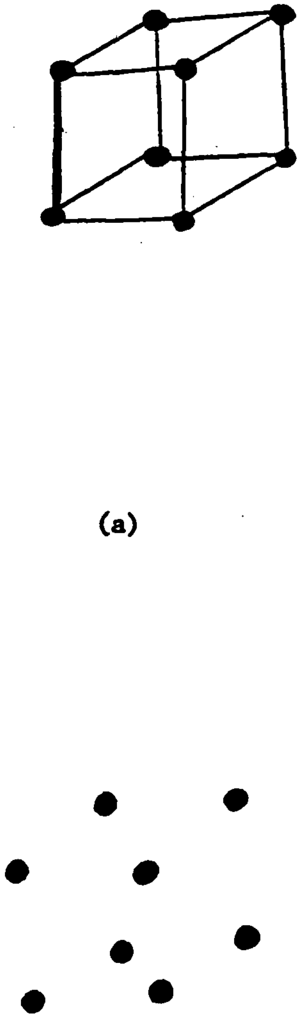

(a)

(b)

Fig. 20. Illustrating the advantages of true 3-D image display. 2-D display of scattering centers at corners of a cube (a) with depth cues (lines) that aid recognition and (b) without depth cues. Depth cues in a true 3-D display occur automatically because of depth of focus and parallax.

depth and parallax cues.

Therefore in this task we are investigating the potential of hybrid (opto-digital) computing in true 3-D image reconstruction and display. Hybrid computing methods combine the flexibility of a digital computer with the speed and efficiency of optical computing. The concepts developed and studied in this task are of interest to imaging methods that enable accessing the 3-D Fourier space of an object function which represents absorptivity, reflectivity or refractive index variation of the object. One such method of particular interest to us is microwave wavelength diversity imaging or inverse scattering which involves accessing the 3-D Fourier space of a scattering object.

It is clear that once the 3-D Fourier space data is made available in digital form through measurement, a 3-D Fast Fourier transform (FFT) algorithm can be utilized to reconstruct 3-D image detail. However, the time required to carry out the FFT, even when an array processor is utilized, precludes at present image reconstruction in real-time. Moreover because of the inherent two dimensionality of computer displays the above entirely digital processing approach does not permit true 3-D image display.

Optical computing is inherently suited for the processing of two dimensional functions. In any hybrid 3-D image reconstruction and display scheme from 3-D Fourier space data it is necessary first to reduce the dimensionality of the data from three to two. In our work reduction of dimensionality of the 3-D Fourier space data is effected through application of Fourier domain projection theorems. This is shown to permit 3-D image reconstruction tomographically in parallel or central slices. The projections are best carried out digitally since the Fourier space data are available to start with in computer memory. It is reasonable to conceive then of the arrangement shown in Fig. 21 where the required 2-D Fourier

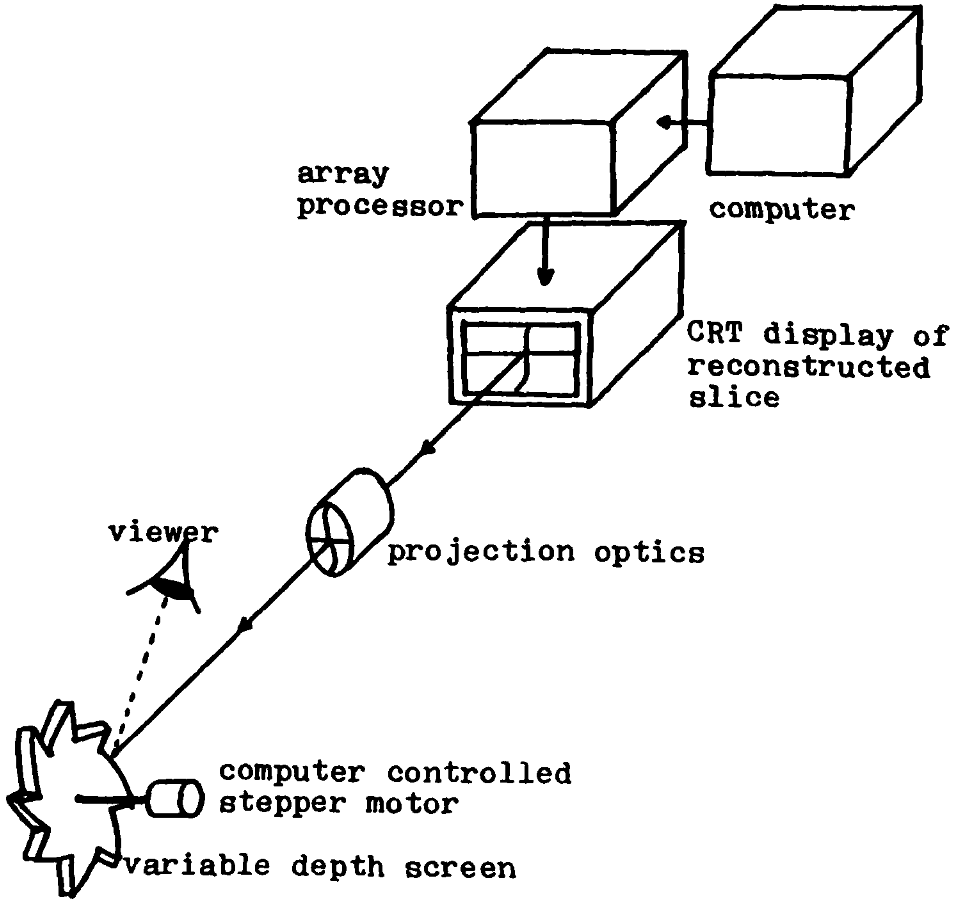

Fig. 21. 3-D image reconstruction and display procedure employing digital Fourier transform.

transformation of the resulting projection holograms is carried out also digitally. The 3-D object detail is then tomographically reconstructed in parallel or central slices. The slices can be displayed individually on a CRT monitor for examination or presented collectively in a perspective view or displayed sequential in rapid succession on the monitor where they can be imaged stroboscopically as shown in Fig. 21 on a volumetric display device such as the toothed wheel described and utilized in our work [12],[40],[45]. This approach requires the use of a powerful array processor to carry out the 2-D FT rapidly. A nonflickering 3-D image consisting of N slices requires a slice frame rate of 33N/s. Thus for example for N=10 the frame rate would be 330/s. This means that the array processor should be able to carry out a 2-D FT of a single projection hologram data in about 3 ms. Current array processing technology permits a 1024 complex point FFT in about this time. Thus 2-D projection holograms formats are limited to about 32x32 pixels. This poses a severe limitation. For example the projection holograms of the simple 8 point scatterer test object employed in our work [12],[40],[45] results in projection holograms containing at least 1600 complex data points. Slightly larger and more complex shaped objects such as the B-52 test model would therefore involve handling larger data formats which lead to excessive computing requirements. Future high speed array processors employing gigahertz logic presently under development will undoubtedly resolve this problem in the future. In fact we believe that tomographic 3-D image reconstruction and display could become one logical application for the next generation of high speed array processors whose current designers and developers are constantly seeking potential areas of application.

Optical information processing is known for its speed and ability to perform 2-D Fourier transforms almost instantaneously at the speed of light employing the simple lens action in coherent light. For this reason we undertook a study of coherent and incoherent hybrid (opto-digital) computing which has the potential for carrying out the 3-D image reconstruction and display operation in real-time even for complex objects. Two coherent optical computing schemes were studied in detail and demonstrated. One is based on the widely known 2-D real Fourier transforming (RFT) property of the convergent lens in coherent laser light and the other on the less widely known concept of the virtual FT (VFT). Both of these methods employ digital pre-processing for generating the required projection holograms as hown in Fig. 22 and space-time multiplexing to form a true 3-D image display tomographically in parallel slices. Both involve photographic storage of the computer generated projection holograms. Space-time multiplexing is shown also to furnish an important advantage. It allows the storage of a large amount of 3-D image information using relatively low resolution film by division of the data over several lower resolution transparencies (projection holograms). As a result the resolution of the film needed to store the various projection holograms is considerably lower than the film resolution required to store the equivalent 3-D image information in a conventional Fresnel hologram. In both schemes a hologram bearing wheel is used for mounting the individual projection holograms and used in the interrogation step. The above relaxation of resolution requirement permits the use of ordinary transparency film and in particular the recently introduced Kodak 4000 Disc camera film [49] which has a 15 exposure disc film that happens to be perfectly compatible with the 3-D image reconstruction and display schemes under study in this task.

The space-time multiplexing feature of these two schemes has the advantage of presenting the 3-D image tomographically as a series of parallel 2-D slices in time. Because of the serial nature of this slice by slice display, interference between the coherent light forming the various slices cannot occur

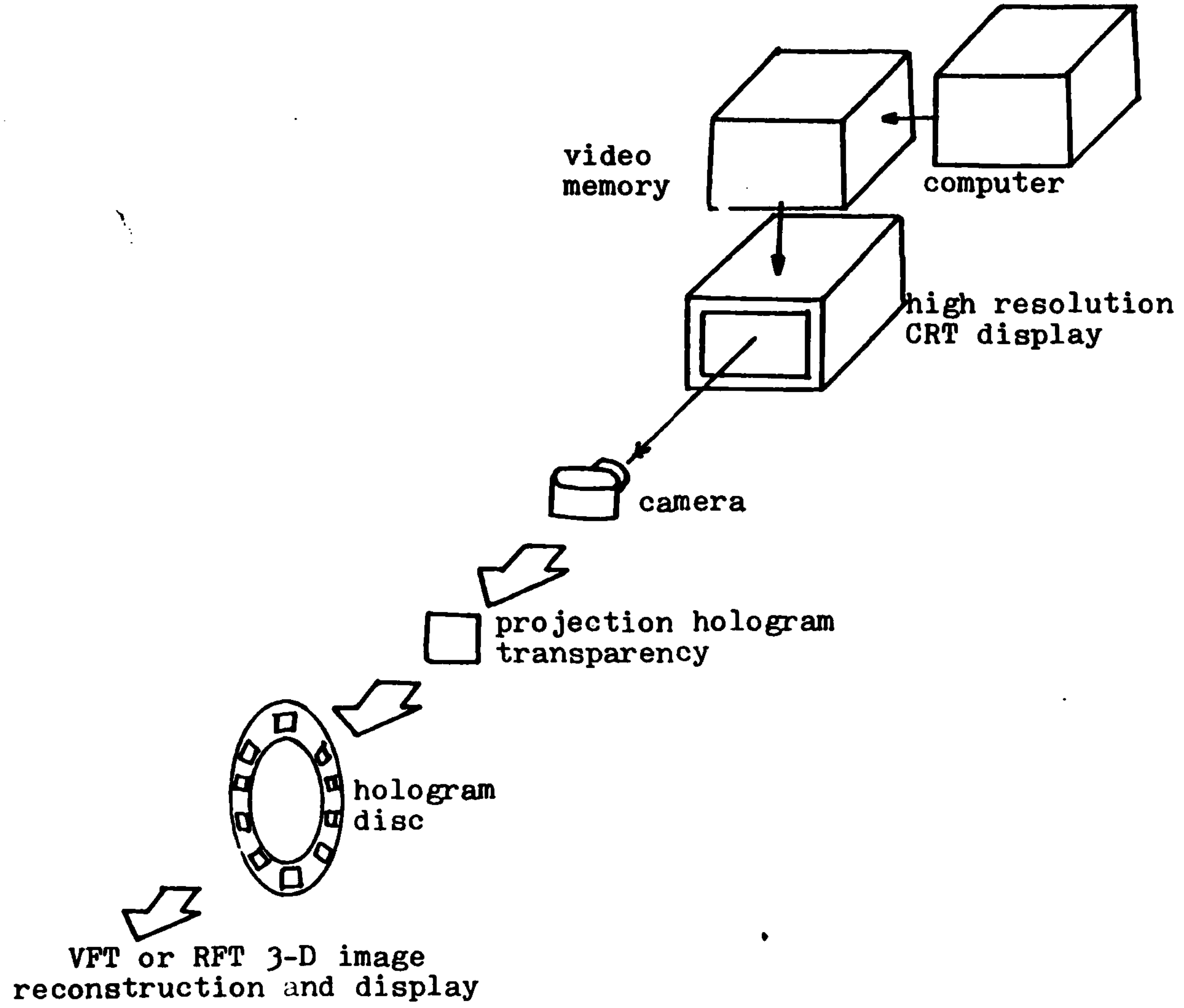

Fig. 22. 3-D image reconstruction and display procedure employing VFT or RFT

avoiding thereby image degradation which could result if the slices were to be reconstructed simultaneously. A volumetric display of a few centimeter cube has been realized in our verifications of the two schemes [12],[40],[45], [46]. The display volume can easily be increased in size to about 10 cm x 10 cm x 10 cm through the use of larger display wheels of light weight material. It is expected that the current state-of-the-art of high speed stepper motors would allow something of the order of N=10,000/33 = 330 slices per second can be produced if each stepping of the motor is accompanied by the introduction of a new projection hologram in the interrogating beam and moves the projection surface one step in depth (normal to the optical axis) by the proper amount.

An important practical feature of the RFT scheme is that the retrieved 3-D image can be observed by more than one observer. This is a distinct advantage over the VFT scheme where only one observer at a time can view the tomographically reconstructed and displayed virtual 3-D image. A further important practical feature of both of these coherent 3-D tomographic image reconstruction and display schemes is their relative ease of implementation and economy.

In certain applications, where one cannot tolerate the time delay associated with photographic data storage, real-time 3-D image reconstruction and display is required. For this reason we have studied the feasibility of replacing the photographic process with a rapidly recyclable spatial light modulator (SLM). Of the variety of commercially available SLM's, the Pockle's Readout Optical Modulator (PROM) based on the optically induced electro-optic effect in a biased Bismuth Silicon Oxide crystal has the shortest specified cycle time.* As such it offers potential for fast frame rates compatible with direct addressing from

---

* Advances in liquid crystal materials and their activation may lead to liquid-crystal-photoconductor SLM with 1 msec frame time.

a blue CRT display of the projection holograms. Recent careful examination (not reported here) of the capabilities of this device, when direct optical addressing from a blue CRT display of the weighted projection holograms of the slices of an N-slice object at a frame rate of 33N/sec, shows that the resulting exposures are inadequate when conventional high resolution blue p-11 phosphor CRT's (such as the Tektronix 606) is employed. One way for enhancing exposure and exploit the high frame rates of the PROM proposed and investigated in our work is PROM intensification. This involves proximity coupling of the PROM crystal to the fiber optic window of an image intensifier with blue phosphor with the intensifier viewing the computer display directly. This approach has the advantage of spectral conversion where any color CRT display can now be used to address the PROM indirectly.

A radiometric analysis of proximity coupling the PROM crystal to a Varo 3603-1 second generation image intensifier containing a microchannel plate was therefore carried out. The results of this analysis showed that exposure levels adequate for a frame rate of 1000/sec are feasible. This frame rate coincides with the highest known cycling rate of the PROM in the superprimed mode [H1]. Although the theoretically predicted frame rate of the intensified PROM approaches 1000/sec, the results obtained with the intensified PROM assembled and evaluated in our work fell short of this mark (5 frames/sec). While the PROM irradiance as a result of proximity coupling was higher than conventional (projection lens) optical coupling it was not sufficient to produce adequate exposure beyond a few frames/sec.

The arrangement used in evaluating the intensified PROM performance is shown in Fig. 23 and in the pictorial view of Fig. 24. Figure 25 shows the results obtained when the intensified PROM was addressed by a grating-like

AD-A134 101 HIGH RESOLUTION 3-D TOMOGRAPHIC IMAGING BY WAVELENGTH 2/2
AND POLARIZATION DI..(U) MOORE SCHOOL OF ELECTRICAL
ENGINEERING PHILADELPHIA PA ELECTR.. N H FARHAT
UNCLASSIFIED 05 JUL 83 EO/MO-6 AFOSR-TR-83-0797 F/G 14/5 NL

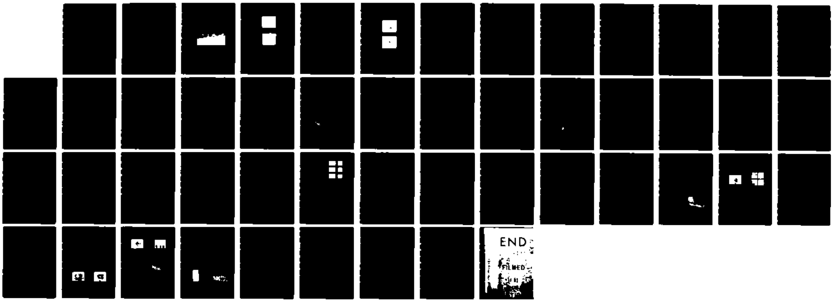

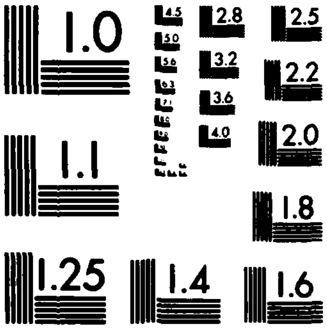

MICROCOPY RESOLUTION TEST CHART
NATIONAL BUREAU OF STANDARDS-1963-A

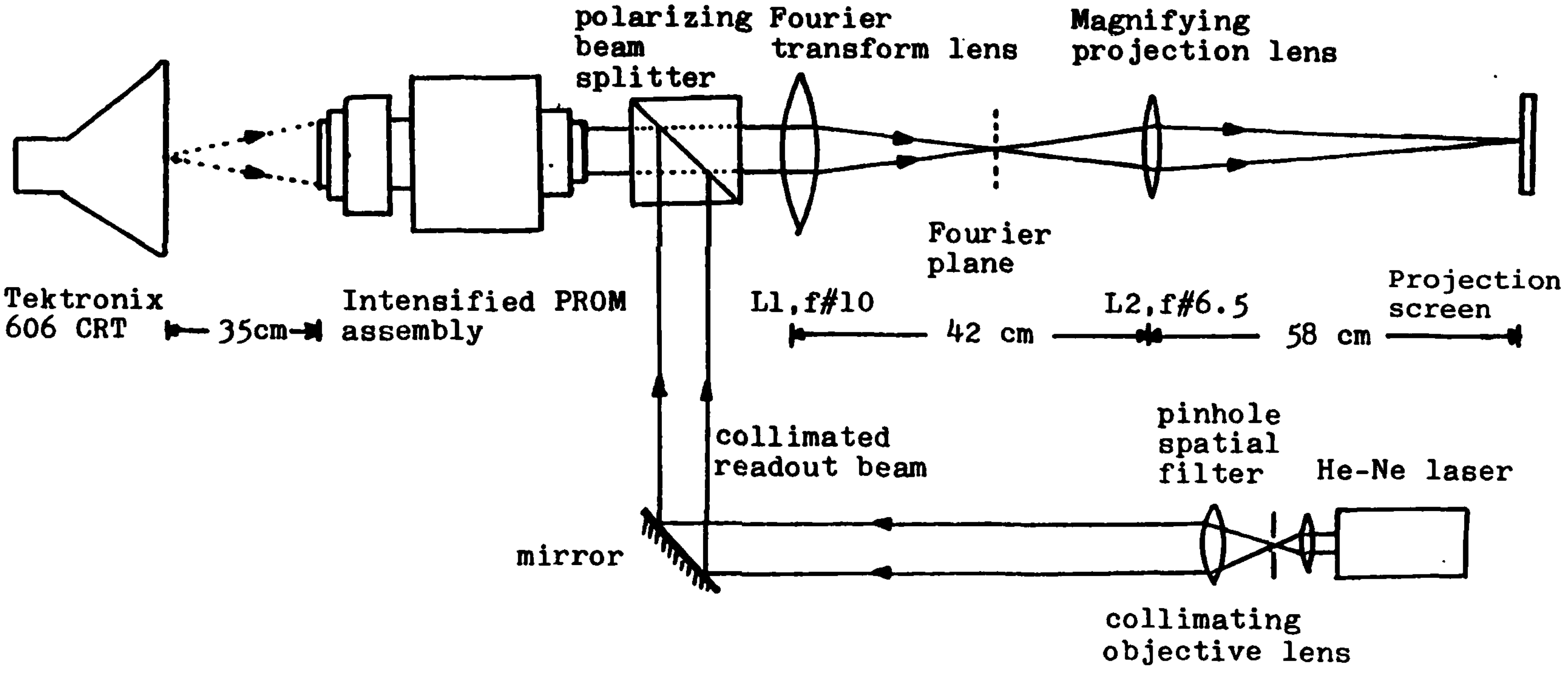

Fig. 23. Image reconstruction and display employing the intensified PROM assembly

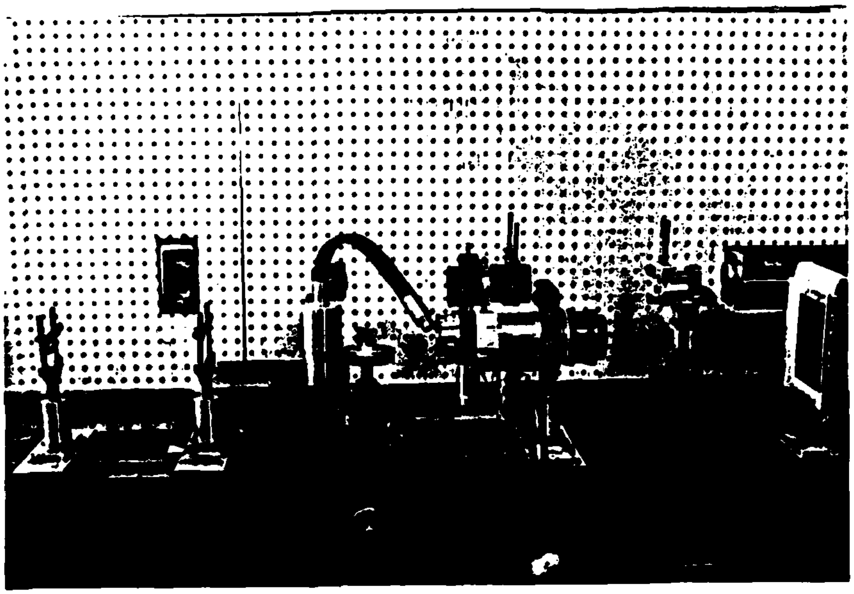

Fig. 24. The pictorial view of the optical bench arrangement of the intensified PROM assembly with objective lens facing the CRT display.

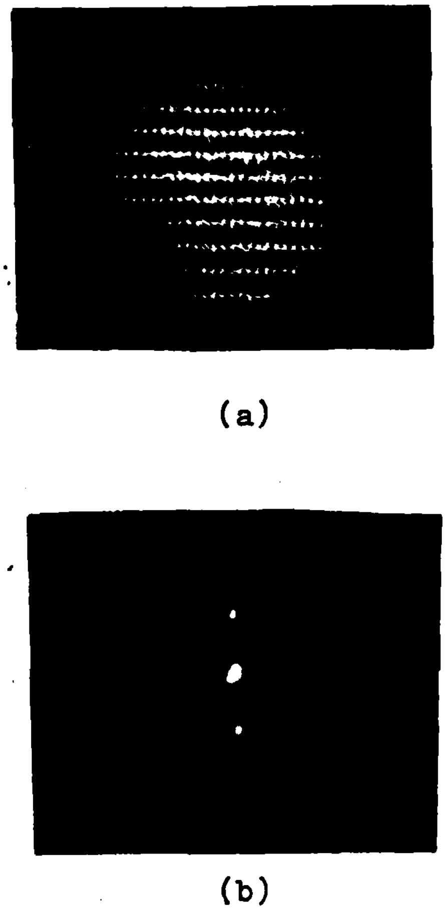

Fig. 25. (a) Image readout from the proximity coupled intensified PROM with a magnifying lens, (b) The Fourier diffraction pattern of (a) recorded in plane of the projection screen in Fig. 24.

array of dots displayed on the CRT at up to 33 frames/sec. Figure 26(a) shows the result observed when the PROM is used in an imaging mode at 5 frames/sec. This pattern essentially represents the spatial activation pattern in the PROM caused by optical addressing. The corresponding Fourier diffraction pattern is shown in Fig. 25(b) where the expected diffraction orders are clearly visible. The results of a similar experiment when the pattern displayed on the CRT was a weighted projection hologram corresponding to the central slice of the eight point test object used in our studies is shown in Fig. 26. Although the image of the 3-dot object corresponding to the addressing projection hologram is discernible, the quality in general is low and enhancement in the performance of the proximity coupled PROM is required. For example the use of higher brightness blue phosphor screen as the intensifier output and the use of a lower numerical aperture fiber optic window are expected to produce the required improvement resulting in a compact and sensitive intensified PROM which can be used in 3-D image reconstruction and display as for example in the scheme shown in Fig. 27. For example a fiber window with numerical aperture of .5, instead of 1 used in the present unit, will according to our calculations reduce the divergence of the proximity coupled image pixels enhancing thereby PROM irradiance. An increase in the localized irradiance by a factor of 36 is predicted. This improvement, together with a better match of the spectral response of a high brightness blue phosphor to the PROM spectral response are expected to increase the irradiance of the proximity coupled PROM by two to three orders of magnitude enabling frame rates of the order of a few hundred to a thousand per second.

It is worth noting that integration of the electro-optic crystal into the image intensifier envelope where it can be subjected to direct electronic charge addressing from the microchannel plate is also possible. Indeed this concept has been under active investigation elsewhere [48] and is expected to furnish

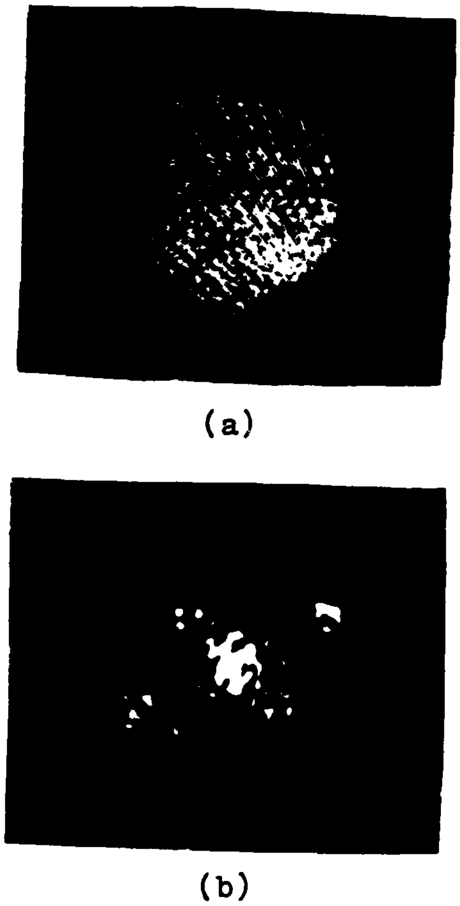

Fig. 26. (a) Image readout from the intensified PROM addressed by a projection hologram of a 3-dot object displayed on the CRT, (b) the Fourier diffraction pattern of (a) recorded in the plane of the projection screen in Fig. 24.

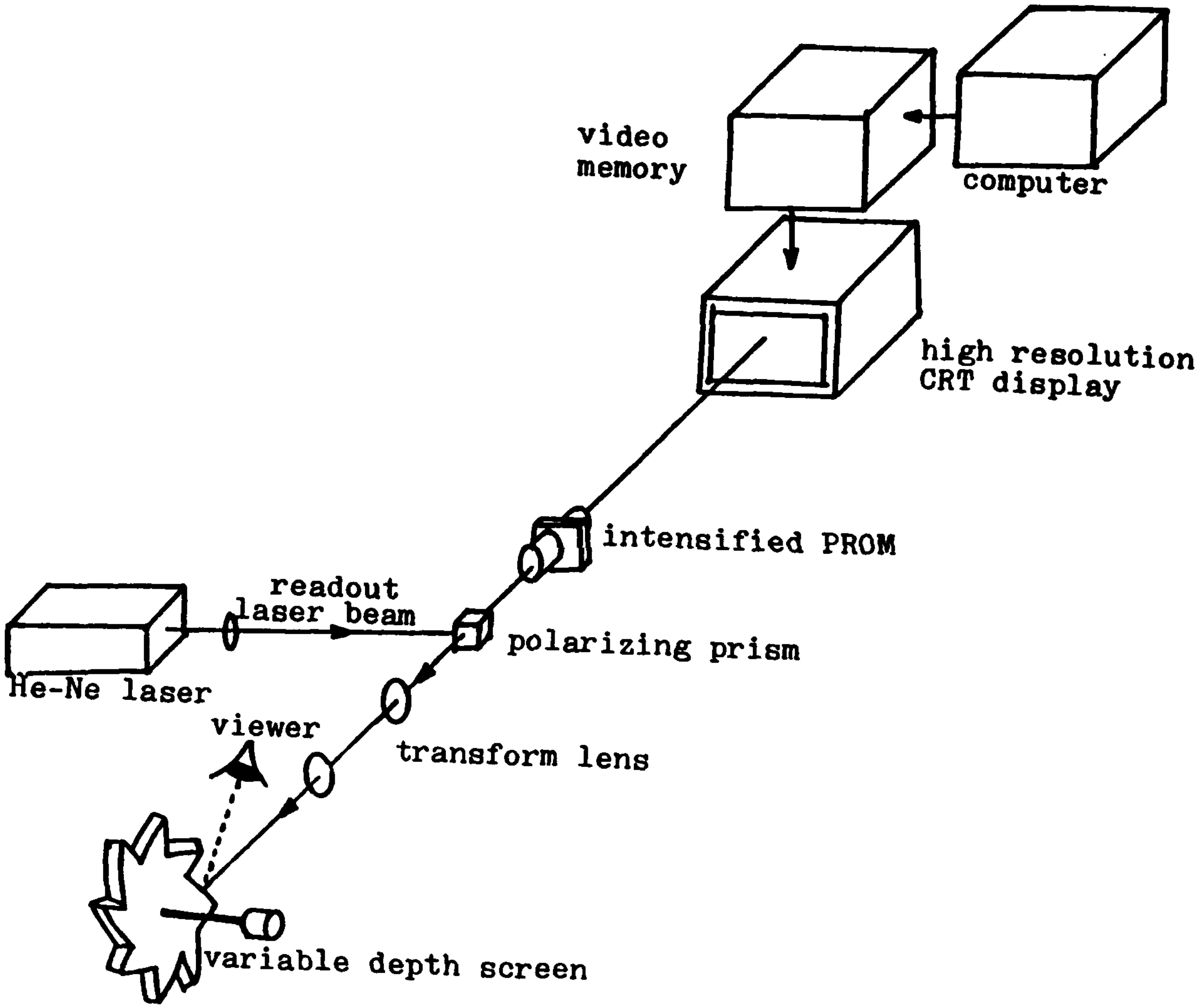

Fig. 27. Real time 3-D image reconstruction and display employing intensified PROM

extremely high frame rates. Ongoing commercial development of high speed SLMs and unintensified SLMs at Hughes and elsewhere is expected to enable eventually the viewing of true 3-D images tomographically using the concepts being developed in our work.

As pointed out at the start of this section our research effort in this task also includes the investigation of high frame-rate incoherent 2-D Fourier transformation methods capable of producing the 2-D Fourier transform of the Fourier domain projection or slice holograms presented on the computer CRT display directly. The scheme receiving most attention is opto-electronic in nature [40]. It also makes use of the projection-slice theorem. During the preceeding period, our efforts in this subtask have focused on the design of the output segment of the processor to put it into a format suitable for readout by a self scanned detector array. This task is now being completed. The work in this subtask has been reported in several publications (see Section 5 - List of Publications).

5. LIST OF PUBLICATIONS AND THESIS

During the current period the following papers have been prepared:

1. N.H. Farhat, "Projection Theorems and Their Applications In 3-D Tomographic Image Reconstruction and Display", Poster Session paper presented at the Gordon Research Conference on Holography and Optical Data Processing, Plymouth, N.H., June 1982.

2. N.H. Farhat, "Tomographic and Projective Reconstruction of 3-D Image Detail in Inverse Scattering", Presented at the *1983 URSI Meeting*, Jan. (5-7), Boulder, Colorado.

3. N.H. Farhat, "Inverse Scattering Reconstructions From Incomplete Fourier Space Data", Presented at and published in the Technical Digest of the OSA/AFOSR 1983 Topical Meeting on *Signal Recovery and Synthesis with Incomplete Information and Partial Constraints*, Jan. 12-14, Lake Tahoe, Nev.

4. N.H. Farhat, C. Yi Ho, and Li Szu Chang, "Projection Theorems and their Applications in Multidimensional Signal Processing", Presented at the Conference on *Advances in Optical Signal Processing* at the SPIE LA/'83 Meeting, Jan. 1983, Also to be published in the Conference Proceeding.

5. N.H. Farhat, C.L. Werner and T.H. Chu, "Microwave Projection Imaging with Near Optical Resolution", Accepted for Presentation at the 1983 International Optical Computing Conference on "Unconventional Imaging and Unconventional Transformations", Boston April 1983. To be published in Conference proceedings.

6. N.H. Farhat, C.L. Werner and T.H. Chu, "Prospects for 3-D Tomographic Imaging Radar Networks", Accepted for presentation at the *1983 International URSI Meeting*, Santiago De Compostela, Spain.

7. N.H. Farhat, D. Jaggard, T.H. Chu, D.B. Ge and S. Mankoff, "Microwave Tomographic and Projective Imaging of Dielectric Bodies", Accepted for presentation at the 1983 International IEEE APS/URSI Meeting, May 23-26, Houston, TX.

Also during this period the following Ph.D. Dissertations dealing with research work supported by this grant have been completed:

1. C. Yi Ho, "Three-Dimensional Tomographic Image Reconstruction and Display", August 1982.

2. T.H. Chu, "Optimal Methodologies in Inverse Scattering", March 1982.

6 . REFERENCES

1. N.H. Farhat, "Longwave Holography" in *Holography in Medicine,* P. Gregnss (Ed.), IPC Science and Technology Press, Richmond (England), 1975.

2. N.H. Farhat, e. al., "Real-Time Microwave Holography - A Feasibility Study", University of Pennsylvania Report - Prepared for University Science Center Inc., Oct. 1972.

3. N.H. Farhat and C.K. Chan, "Three-Dimensional Imaging by Wave-Vector Diversity", Presented at the 8th Int. Symp. on Acoust. Imaging, Key Biscayne, Fla., 1978 and published in *Acoustical Imaging,* Vol. 8, A. Metherell (Ed.), pp. 499-516, Plenum Press, New York 1980.

4. C.K. Chan and N. Farhat, "Frequency Swept Tomographic Imaging of Three-Dimensional Perfectly Conducting Objects", IEEE Trans. on Ant. and Prop., Special Issue on Inverse Methods in Electromagnetics, Vol. AP-29, pp. 312-319, March 1981.

5. N.H. Farhat, W.I. Landauer and W.E. Wallace, "Computer Assisted Naval Applications of Holography", Computer Command and Control Co., Report No. 132-4, prepared for Naval Analysis Programs, Office of Naval Research under contract No. N0014-69-C-0167, February 1973.

6. N. Farhat, C.K. Chan and T.H. Chu, "A Target Derived Reference Technique for Frequency Diversity Imaging", North American Radio Science Meeting, Quebec, 1980.

7. N. Bojarski, "Inverse Scattering", Naval Air Command Final Report N000 19-73-C-0312F, Feb. 1974.

8. R.M. Lewis, "Physical Optics Inverse Diffraction", IEEE Trans. on Ant. and Prop., Vol. AP-17, pp. 308-314, May 1969.

9. G.T. Ruck, et. al., *Radar Cross Section Handbook,* G.T. Ruck (Editor), Plenum Press, New York 1970, Chapter 2, Vol. 1.

10. J.A. Stratton, *Electromagnetic Theory,* McGraw Hill, New York, (1941), Section 8-14.

11. J.D. Jackson, *Classical Electrodynamics,* John Wiley and Sons, Inc., New York (1962) Section 9.6.

12. N.H. Farhat, "High Resolution 3-D Tomographic Imaging by Wavelength and Polarization Diversity", Univ. of Pennsylvania Proposal, submitted to the Air Force Office of Scientific Research, April, 1981.

13. N.H. Farhat and C.Y. Ho, "The Virtual Fourier Transform and its Application to Three-Dimensional Display", in *Optics in Four Dimensions,* M.A. Machado and L.M. Marducci (Eds.), American Institute of Physics publications, New York (1981), pp. 341-354.

References (cont'd)

14. J. Radon "über die Bestimmung von Fonktionen Durch ihre Integraldwerte Längs Gewisser Mannigfaltigkeiten" Ber. Saechs. Akad. Wiss. (Leipzig), Vol. 19, pp. 262-278, 1917.

15. R.N. Bracewell, "Strip Integration in Radioastronomy", Australian J. of Phys., Vol. 9, pp. 198-217, 1956.

16. G. Stroke and M. Halioua, "Three-Dimensional Reconstruction in X-ray Crystallography and Electron Microscopy by Reduction to Two Dimensional Holographic Implementation", Trans. Amer. Crystal. Assoc., Vol. 12, pp. 27-41, 1976.

17. H.H. Barrett and W. Swindle, *Radiological Imaging: Theory and Image Formation, Detection and Processing*, Academic Press, New York 1982.

18. Y. Das and W.M. Boerner, "On Radar Shape Estimation Using Algorithms for Reconstruction From Projections", IEEE Trans. on Ant. and Prop., Vol. AP-26, pp. 274-279, March 1978.

19. A.J. Rockmore, R.V. Denton and B. Friedlander "Direct Three-Dimensional Image Reconstruction", IEEE Trans. on Ant. and Prop., Vol AP-27, pp. 239-241, March 1979.

20. J.W. Goodman, *Introduction to Fourier Optics*, McGraw Hill, New York, 1968.

21. D. Gabor, "Light and Information" in *Progress in Optics*, Vol. 1, E. Wolf (Ed.), pp. 109-133, North Holland Publishing Co., Amsterdam, 1961.

22. J. Winthrop, "Structural Information Storage in a Hologram", IBM J. of Res. and Dev., Vol. 14, pp. 501-507, Sept. 1971.

23. T. Jannson, "Impulse Response and Shannon Number of Holographic Optical Systems", Optics Comm., Vol. 10, pp. 232-237, March 1974.

24. J.C. Dainty (Ed.) *Laser Speckle*, Springer-Verlag Berlin, (1975).

25. Special Issue on Speckle in Optics, Journal of the Optical Society of America, Vol. 66, November 1966.

26. J.D. Blackwell and N.H. Farhat, "Image Enhancement in Longwave Holography by Electronic Differentiation", Optics Comm., Vol. 20, pp. 76-80, Jan. 1977.

27. R.L. Hartman, "Submillimeter Systems for Imaging Through Inclement Weather", Digest of Second Int. Conf. and Winter School on Submillimeter Waves and their Applications, IEEE Cat. No. 76 CH 1152-8MTT, Dec. 1976.

28. D. Gabor, "Laser Speckle and its Elimination", IBM J. of Res. and Dev., Vol. 14, pp. 509-514, Sept. 1970.

References (cont'd)

29. N. George and A. Jain, "Speckle Reduction Using Multiple Tones of Illumination", App. Optics, Vol. 12, pp. 1202-1212, June, 1973.

30. H. Fuju and T. Asakura, "Effect of Surface Roughness on the Statistical Distribution of Speckle Intensity", Optics Comm., Vol. 11, pp. 35-38, May, 1974.

31. J.S. Lim and H. Nawab, "Techniques for Speckle Noise Removal", Optical Engineering, Vol. 20, pp. 472-480, May/June, 1981.

32. V.J. Corcoran, "Speckle and Specular Effects in Submillimeter Imaging", in Reference 27.

33. J.W. Goodman, "Some Fundamental Properties of Speckle (see ref. 24).

34. D.C. Champeney, *Fourier Transforms and Their Physical Applications*, Academic Press, London (1973), p. 52.

35. N.H. Farhat and C.L. Werner, "An Automated Microwave Measurement Facility for Three Dimensional Tomographic Imaging by Wavelength Diversity", presented at the 1981 Intern. IEEE AP-S Symp./National Radio Science Meeting, L.A., June 1981.

36. G.T. Ruck *Radar Cross Section Handbook*, Plenum Press, New York 1970.

37. N.H. Farhat, "High Resolution Longwave Frequency Swept Holographic Imaging", 1975 Ultrasonics Symposium Proc., IEEE Cat #75CH0994-4S.

38. R.M. Mersereau and A.V. Oppenheim, "Digital Reconstruction of Multidimensional Signals From their Projections", Proc. IEEE, Vol. 62, pp. 1319-1338, October 1978.

39. N.H. Farhat and C.K. Chan, "Super-resolution by Wavelength Diversity in Longwave Imaging", in Optica Hoy Y Mañana Proc. ICO-11 Conference J. Bescos et. al. (Eds.), Inst. De Optica-Sociedad Española De Optica, Madrid 1978.

40. N.H. Farhat, "High Resolution 3-D Tomographic Imaging By Wavelength and Polarization Diversity", University of Pennsylvania Research Proposal, Sumitted to Air Force Office of Scientific Research, March 16th, 1982.

41. B.P. Hildebrand, "Acoustical Holography by Sector Scanning", J. Opt. Soc. Am., Vol. 63, pp. 1393-1348, Nov. 1973.

42. K. Yamane and M. Matsou, "Microwave Holography by Rotational Scanning", IEEE Trans. on Ant. and Prop., Vol. AP-26, pp. 280-281, March 1978.

43. R.W. Cribbs and B.L. Lamb, "Resolution of Defects by Microwave Holography", Proc. of the Engineering Applications of Holography Symposium, conducted for ARPA by TRW Systems Group, Los Aneles, Feb. 1972.

References (cont'd)

44. C.E. Shannon, "Communication in the Presence of Noise", Proc. IRE, Vol. 37, p. 10, 1949.

45. N.H. Farhat, C. Yi Ho and Li Szu Chang, "Projection Theorems and Their Applications in Multidimensional Signal Processing", presented at the Conference on *Advances in Optical Signal Processing* at the SPIE LA/'83 Meeting, Jan. 1983. Also to be published in the Conference Proceeding by SPIE.

46. N.H. Farhat and C-Yi Ho, "The Virtual Fourier Transform and its Application in Three-Dimensional Display", in *Optics in Four Dimensions*, M.A. Machado and L.M. Narducci (Eds.), Am. Inst. of Phys. publication, New York, (1981), pp. 341-354.

47. B.A. Horwitz, "IDES - The Image Detail Enhancement System", Itek Technical Report.

48. C. Ward, "Performance Limitations of the Microchannel Spatial Light Modulator", Proc. 1980 European Conference on Optical Systems and Applications, Utrecht, The Netherlands, Sept. 1980.

49. "Innovative Disc Camera Clicks for Kodak", Optics News, Vol. 9, pp. 6-8, January/February 1983.

50. "Vector Measurements of High Frequency Networks", Hewlett Packard Co., Sept. 1978.

51. C.B. Chitteneni, "Frequency Domain Optimal Inverse Convolution Filtering of Noisy Data", Private comm. Conoca Inc. Report and also Digest of OSA/AFOSR Topical Meeting on "Signal Recovery and Synthesis with Incomplete Information and Partial Constraints", Incline Village 1983.

52. N.S. Nahman, "Some Results using Guillaume-Nahman Automated Deconvolution Methode", Tech. Digest, URSI-National Radio Science Meeting, Jan. 5-7, 1983, Boulder, CO.

53. B. Paruk and S.M. Riad, "Performance Evaluation of Frequency Domain Deconvolution Techniques", Tech. Digest, URSI - National Radio Science Meeting Jan 5-7, Boulder, Colo., 1983.

54. J.P. Burg, "Maximum Entropy Spectral Analysis", Paper presented at the 37th Annual International Meeting, Soc. of Explor. Geophys., Oklahoma City, Oklahoma, (1967).

55. T. Thorvaldsen, "Maximum Entropy Spectral Analysis in Antenna Spatial Filtering", IEEE Trans. on Ant. and Prop., Vol. AP-28, July 1980.

References (cont'd)

56. J.C. Ables, "Maximum Entropy Spectral Analysis", Astron. Astrophys., Supp. 15, pp. 383-393, 1974.

57. B.R. Frieden and D.C. Wells, "Restoration with Maximum Entropy...", J. Opt. Soc. Am., Vol. 68, pp. 91-103, 1978.

58. Digest of the OSA/AFOSR Topical Meeting On "Signal Recovery and Synthesis with Incomplete Information and Partial Constraints", Jan. 1983. Incline Village, Nev.

59. J. Skilling, "Maximum Entropy Image Reconstruction From Phaseless Fourier Data", in ref. 58.

60. R.W. Gerchberg, "Super-Resolution Through Error Energy Reduction", Optica Acta, Vol. 21, pp. 704-720, 1974.

61. A. Papoulis, "A New Algorithm on Spectral Analysis and Bandlimited Extrapolation", IEEE Trans. on Circuits and Systems, Vol. CAS-22, pp. 735-742, Sept. 1975.

62. G.B. Feldkamp and J.R. Fienup, "Noise Properties of Images Reconstructed From Fourier Modulus", Proc. 1980, International Optical Computing Conference, SPIE, Vol. 231. Book II, IEEE Cat. No. 80CH1548-7.

63. R.J. Marks, II, and D.K. Smith, "Iterative Coherent Processor for Band-Limited Signal Extrapolation", SPIE Vol. 231, Book II, IEEE Cat. No. 80CH1548-7.

64. Y. Yamakoshi and T. Sato, "Iterative Image Restoration From Data Available in Multiple Restricted Regions", in ref. 58.

65. S.J. Howard, "Method for Continuing Fourier Spectra Given by the Fact Fourier Transform", J. Opt. Soc. Am., Vol. 71, pp. 95-98, Jan. 1981.

66. H.P. Baltes, ed. *Inverse Scattering in Optics*, Springer-Verlag, New York, 1978.

67. H.P. Baltes, ed. Inverse Scattering Problems in Optics, Springer-Verlag, New York, 1980.

68. J.R. Fienup, "Phase Retrieval in Astronomy", in ref. 58.

69. R.W. Gerchberg and W.O. Saxton, "A Practical Algorithm for the Determination of Phase From Image and Diffraction Plane Pictures", Optik, Vol. 35, pp. 237, 1972.

70. W.A. Saxton, *Computer Techniques for Image Processing in Electron Microscopy*, Academic Press, New York, 1978.

References (cont'd)

71. M.A. Fiddy, B.J. Brames and J.C. Dainty, "Sufficient Condition For Phase Retrieval in Two Dimensions", in ref. 58.

72. A. Tikhonov and V. Arsenine, *Solutions of Ill-Posed Problems*, J. Wiley and Sons, Inc., New York, 1977.

73. A.V. Sergeev, "Uniqueness of the Values of the Wavefield Reconstructed by Inverse Diffraction Methods", Sov. Phys. Acoust., Vol. 26, pp. 507-509, Dec. 1980.

74. A.J. Devaney, "Non Uniqueness in the Inverse Scattering Problem," J. Math. Phys., Vol. 19, pp. 1526-1531, July 1978.

75. W. Perry, "Approximate Solution of Inverse Problems with Piecewise Continous Solutions", Radio Science, Vol. 12, pp. 637-642, Sept.-Oct., 1977.

76. A. Papoulis, *Signal Analysis*, McGraw Hill, New York (1977), pp. 191-196.

77. A.V. Oppenheim and R.W. Schafer, *Digital Signal Processing*, Prentice Hall, Englewood Cliffs, 1975.

78. W.A. Proatt, *Digital Image Processing*, J. Wiley, New York, 1978.

79. J.R. Fienup, "Reconstruction of an Object From Modulus of its Fourier Transform", Optics Letters, Vol. 3, pp. 27-29, July 1979.

80. C.H. Papas, "A Note on the Inverse Scattering of Electromagnetic Waves," Unpublished Technical Note, CALTECH, 1976.

81. L.I. Schiff, *Quantum Mechanics*, 3rd Edition, McGraw-Hill, New York, 1955.

82. A.W. Joshi, *Elements of Group Theory for Physicists*, 2nd Edition, J. Wiley and Sons, New York, 1973.

83. D.L. Jaggard, A.R. Mickelson and C.H. Papas, "On Electromagnetic Waves in Chiral Media", App. Phys. (Springer-Verlag), Vol. 18, pp. 211-217, 1979.

84. G.E. Heath, "Bistatic Reflection Asymmetry, Polarization Reversal Asymmetry and Polarization Reversal Reflection Symmetry", IEEE Trans. Ant. and Prop., AP-29, pp. 429-434, 1981.

85. W.M. Boerner, et. al., "Polarization Dependence in Electromagnetic Inverse Problems," IEEE Trans. Ant. and Prop., Vol. AP-29, pp. 262-270, 1981.

86. C.P. Miles and D.L. Jaggard, "The Use of Optical Fourier Transforms to Diagnose Plemorphism, Size and Chromatic Clumping in Nuclear Models", Anal. Quant. Cyt., Vol. 13, pp. 149-156, 1980.

References (cont'd)

87. J.W. Crispen and K.M. Siegel, *Methods of Radar Cross-Section Analysis*, Academic Press, New York, 1968.

7. APPENDICES

APPENDIX I

THE PROJECTION-SLICE THEOREM

APPENDIX I

THE PROJECTION-SLICE THEOREM

We consider a 3-D object function $\gamma(\bar{r})$ of limited extent and its 3-D Fourier transform $\Gamma(\bar{p})$, $\bar{r}$ and $\bar{p}$ being 3-D position vector in object and Fourier space respectively. Then referring to Fig. 1 of this appendix we let Σ be an arbitrarily chosen *projection plane* in object space defined by $\bar{\rho}\cdot\bar{n} = 0$ where $\bar{\rho}$ is a 2-D position vector of a point on Σ and $\bar{n}$ is the unit normal to Σ defining also the direction of projection lines or integration of $\gamma(\bar{r})$.

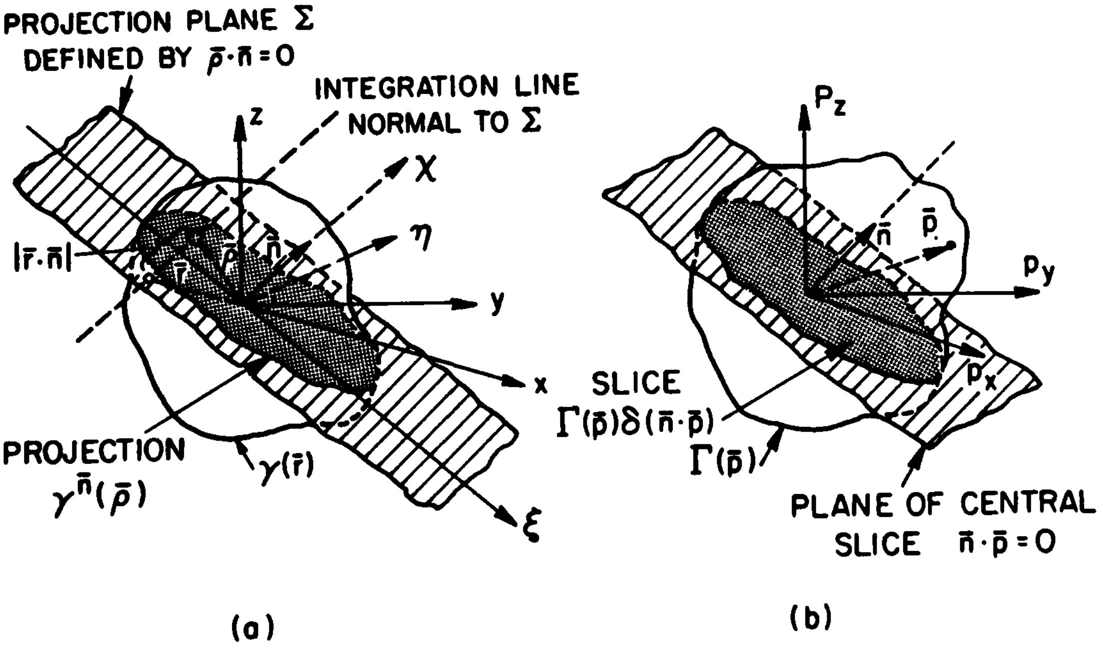

Fig. 1. Geometry referred to in the derivation of the projection slice theorem.

The equation of any line normal to Σ is,

$$\begin{aligned} \bar{r} &= \bar{\rho} + (\bar{n}\cdot\bar{r})\bar{n} \\ &= \bar{\rho} + \chi\,\bar{n} \end{aligned} \qquad (1)$$

where χ is the distance from Σ measured in the direction of $\bar{n}$. Equation (1) allows us to express $\gamma(\bar{r})$ in the alternate form namely $\gamma(\bar{\rho} + \chi\bar{n})$. Now the projection of $\gamma(\bar{r})$ on Σ can be defined as,

$$\gamma^{\bar{n}}\ (\bar{\rho}) = \int_{-\infty}^{\infty} \gamma(\bar{\rho} + \chi\bar{n})\ d\chi \qquad (2)$$

where the superscript $\bar{n}$ is used to designate the direction of projection.

Using the 3-D Fourier transform relation between $\gamma(\bar{r})$ and $\Gamma(\bar{p})$, that is,

$$\gamma(\bar{r}) = \int_{-\infty}^{\infty} \Gamma(\bar{p})\ e^{-j\bar{p}\cdot\bar{r}}\ d\bar{p} \qquad (3)$$

in (2), we obtain,

$$\gamma^{\bar{n}}\ (\bar{\rho}) = \int_{-\infty}^{\infty} \{ \int_{-\infty}^{\infty} \Gamma(\bar{p})\ e^{-j\bar{p}\cdot(\bar{\rho} + \chi\bar{n})}\ d\bar{p}\ \}\ d\chi \qquad (4)$$

$$= \iint_{-\infty}^{\infty} \Gamma(\bar{p})\ e^{-j\bar{p}\cdot\bar{\rho}}\ e^{-j(\bar{n}\cdot\bar{p})\chi}\ d\chi\ d\bar{p} \qquad (5)$$

$$= \int \Gamma(\bar{p})\ \delta(\bar{p}\cdot\bar{n})\ e^{-j\bar{p}\cdot\bar{\rho}}\ d\bar{p} \qquad (6)$$

where the last step is obtained by virtue of the fact that the integration with respect to χ in eq. (5) yields the delta "function" $\delta(\bar{n}\cdot\bar{p})$. The presence of $\delta(\overline{n}\cdot\overline{p})$ in the integrand of (6) confines the values of $\overline{p}$ to those lying in the plane $\overline{p}\cdot\overline{n} = 0$ i.e., the plane of the *central slice* of the $\overline{p}$-space that lies parallel to the projection plane Σ in object space. Accordingly eq. (6) can be written in the equivalent form,

$$\gamma^{\overline{n}}(\overline{\rho}) = \int \Gamma(\overline{q})\, e^{j\,\overline{q}\cdot\overline{\rho}}\, d\overline{q} \tag{7}$$

where $\overline{q}$ is a 2-D position vector in the plane of the central slice $\overline{p}\cdot\overline{n} = 0$ in $\overline{p}$-space or Fourier space.

Equation (7) says that the 2-D projection $\gamma^{\overline{n}}(\overline{\rho})$ of the 3-D object function $\gamma(\overline{r})$ on a plane normal to $\overline{n}$ and the central slice data $\Gamma(\overline{q})$ of the 3-D Fourier transform $\Gamma(\overline{p})$ lying on the plane $\overline{p}\cdot\overline{n} = 0$ are 2-D Fourier transform pairs. By altering the orientation of $\overline{n}$ one can reconstruct $\Gamma(\overline{p})$ as series of central slices obtained by Fourier transforming the projections of $\gamma(\overline{r})$ in the chosen direction of $\overline{n}$.

The same procedure used in the above derivation can be repeated to show that projections of $\Gamma(\overline{p})$ in $\overline{p}$-space in direction $\overline{n}$ and slices $\gamma(\overline{r})$ in central planes $\overline{n}\cdot\overline{r} = 0$ are also 2-D Fourier transform pairs.

This completes a formal proof of the projection slice theorem used extensively in our research work in the processing of multi-dimensional signals and 3-D image understanding.

APPENDIX II

RESOLUTION, STRUCTURAL DEGREES OF FREEDOM, SNR, AND INFORMATION CONTENT

APPENDIX II

RESOLUTION, STRUCTURAL DEGREES OF FREEDOM, SNR, AND INFORMATION CONTENT

The classical Rayliegh resolution limit of an incoherent imaging system is solely determined by wavelength and geometry in accordance to

$$\delta \approx \frac{\lambda}{D} d \qquad (1)$$

where referring to Fig. 1 of this appendix, D is the aperture size, λ is the mean wavelength and d equals d_1 or d_2 depending on whether resolution in object space or image space is being considered and δ is the minimum spacing between two incoherent object points.

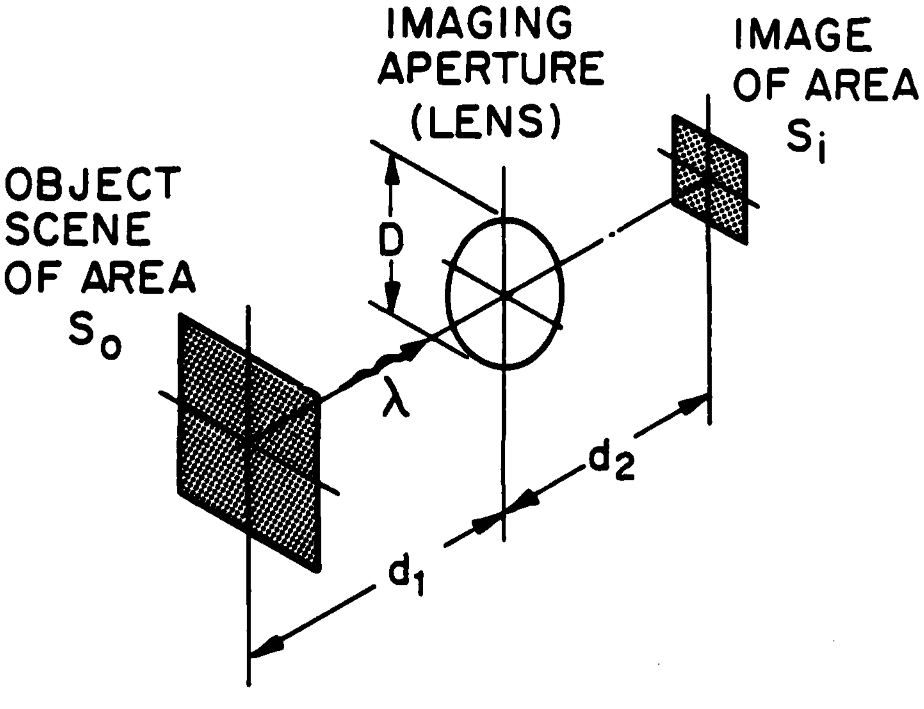

Fig. 1. Simplified imaging geometry.

The limitations of this formula become evident when one considers monochromatic illumination or becomes concerned with the effect of noise on resolution. It is well known [20] that with monochromatic illumination the ability to resolve two adjacent object points in the arrangement of Fig. 1 depends on their relative phases and ratio of amplitudes. Resolution better or worse than the classical incoherent limit of eq. (1) can result. Daily experience in photography or everyday TV watching tells us that the ability to resolve fine detail of a scene depends on the SNR. The higher the noise level present in a picture the coarser will be the detail that can be discerned by the observer. It is clear from these brief general observations that the "quality" or "figure of merit" of an imaging system, as represented by the "quality" of the image formed by it, cannot be determined solely by the classical incoherent resolution of eq. (1).

A more complete description that can treat the imaging system as a communication channel operating between object space and image space in Fig. 1 would be more helpful in accounting for the role of SNR. The *information content* of the formed image can be used then as a more complete measure of image quality and system performance [21]-[23]. This would provide a more realistic measure than geometrical resolution. A systematic formulation of such a description is presented next.

Structural Degrees of Freedom

The number of *degrees of freedom* of a signal whether temporal or spatial equals the number of independent real parameters needed to describe the signal fully. Let us examine the number of degrees of freedom in the image formed by the imaging system of Fig. 1. Taking the image area to be S_i, the number of resolvable elements or resolution cells (pixels) within it in the absence of noise (random or speckle) is

$$N = \frac{S_i}{\delta^2} = \frac{S_i D^2}{\lambda^2 {d_2}^2} = \frac{S_i \Omega}{\lambda^2} \tag{2}$$

where $\Omega \approx \frac{D^2}{d^2}$ is the solid angle subtended by the imaging system aperture at the image plane. Noting that in the limit as $\Omega \to 0$ the number of resolution elements on the object must reduce to 1 we find that we must modify the above formula to,

$$N = 1 + \frac{S_i \Omega}{\lambda^2} \tag{3}$$

Each of these image pixels can be distinguished by its amplitude and phase and by its state of polarization (when electromagnetic radiation is involved). Since the state of polarization of the observed field at each pixel can be fully determined by measuring the amplitude and phase of two transverse orthogonal field components, the total number of real parameters needed to completely describe the image is

$$\mathcal{F} = (2)\mathrm{x}(2)\mathrm{x}\ (1 + \frac{S\Omega}{\lambda^2}) \tag{4}$$

where the first factor of two is due to polarization and the second is because amplitude and phase are measured. Because this number of degrees of freedom is derived from purely geometrical considerations it is referred to as the number of *structural degrees of freedom* of the image or of the wavefield collected or intercepted by the imaging system.

The number of structural degrees of freedom is an invariant of the imaging system, i.e. it is not altered by lossless propagation. This invariance can be appreciated by computing $\mathcal{F}$ in terms of object space rather than image space considerations. Since the geometrical resolution in object space is $\delta = \lambda d_1/D$, the number of resolution cells or resolvable elements (pixels) on the object is,

$$N = \frac{S_o}{\delta^2} = \frac{S_o D^2}{\lambda^2 d_1{}^2} = \frac{S_i D^2}{\lambda^2 d_2{}^2} = \frac{S_i \Omega}{\lambda^2} \qquad (5)$$

where we have used the relation

$$S_o = (\frac{d_1}{d_2})^2 \quad S_i$$

with (d_2/d_1) being the magnification of the imaging system of Fig. 1. Thus eq. (4) is an invariant of the imaging system.

The quantity $S\Omega/\lambda^2$ appearing in eq. (1) is equal to the *space-bandwidth product* of the imaging system as can be verified by determining the spatial frequency cut-off of the system. This cut-off equals the highest spatial frequency component in the image. If the size of the finest resolvable detail in the image is $\delta = \lambda d_2/D$, then the spacing between two resolvable cells is δ and the maximum spatial frequency is $1/\delta = D/\lambda d_2$. The space-bandwidth product of the image assuming it is of square boundary is $S(1/\delta)^2 = SD^2/\lambda^2 d_2{}^2 = S\Omega/\lambda^2$. Thus another form of eq. (4) is

$$F = (2)x(2)x(1 + \text{space bandwidth product}) \qquad (6)$$

Equation (6) can also be written in yet another form,

$$F = (2)x(2)x(1 + \text{object size x sixe of Fourier space accessed by the system}) \quad \text{.........} \qquad (7)$$

The expressions in eqs (6) and (7) are useful since they can be viewed as general and therefore generalized to be considered applicable to 3-D objects and their 3-D Fourier space.

Channel Capacity

Considering that each resolution cell or pixel in image space corresponds to a distinct resolution cell in object space on a one-to-one basis, we can view each pair as the terminal points of an independent communication channel to which we can apply the well known Shannon channel capacity formula [44] to each pixel. However because the amplitude, phase, or polarization properties can be involved in the transmission of information (conveying information in each pixel) the number of independent communication channels equals the number of degrees of freedom. The capacity of each channel capacity is [44],

$$C = \beta T \log(1 + \frac{P_s}{P_n}) \quad [\text{bits}] \tag{8}$$

where β is the available bandwidth, T is the time duration or observation time, P_s and P_n are the signal and noise powers respectively corresponding to signal and noise amplitudes that are assumed to be Gaussian distributed. C is thus the maximum amount of information that can be measured in [bits] that can be transmitted over a communication channel of bandwidth β[Hz] in a time duration T [sec] with a mean SNR of P_s/P_n.

It follows from the above discussion that the information content of the image is,

$$C_i = FC = F\beta T \log\,(1 + \frac{P_s}{P_n}) \qquad [\text{bits}] \tag{9}$$

where P_s and P_n are now taken as the mean SNR in the image.

Equation (9) is the final result of this analysis. When used with eqs. (4), (6) or (7) it gives a measure of the maximum information content in the image. It provides therefore a measure of the performance of an imaging system that is more realistic than the classical resolution limit. Equations (4),(6), (7) and (9) describe clearly the roles of SNR, aperture size (through Ω), polarization discrimination, coherent detection, and also the advantage of using *sophisticated signals* (or illumination in our context) for which the temporal time-bandwidth product, $T\beta$, is greater than unity as compared to the monochromatic signaling or CW illumination case for which $\beta T = 1$. Also evident in these results is the advantage of using shorter wavelengths.

APPENDIX III

INVERSE SCATTERING RECONSTRUCTION FROM INCOMPLETE FOURIER-SPACE DATA

(Preprint of Paper Presented at the 1983 OSA/AFOSR Winter Topical Meeting on Signal Recovery and Synthesis - Incline Village, Nevada.)

Inverse Scattering Reconstructions From Incomplete Fourier Space Data

N.H. Farhat
University of Pennsylvania
Electro-Optics and Microwave-Optics Laboratory
The Moore School of Electrical Engineering
200 S. 33rd St., Philadelphia, Pa. 19104

ABSTRACT

We show that 3-D tomographic inverse scattering reconstruction of a scattering object is obtainable from data lying on a curved surface, rather than within a volume, of its accessed Fourier space as would ordinarily be required.

I. Introduction

It is known from inverse scattering theory [1]-[4], that multiaspect *monostatic* or *bistatic* coherent measurement of the far field scattered by a plane-wave illuminated conducting or non-dispersive object under conditions that satisfy the *physical optics* and Born approximations can be used to access the 3-D Fourier space $\Gamma(\bar{p})$ of the object *scattering function* $\gamma(\bar{r})$. Here $\bar{r}$ is a 3-D position vector in object space measured relative to a common origin in the object or its vicinity and $\bar{p} = k(\bar{1}_R - \bar{1}_i)$ is a 3-D position vector in Fourier space or $\bar{p}$-space with $\bar{1}_R$ and $\bar{1}_i$ being unit vectors in the directions of observation and incident illumination respectively and k is the wavenumber of illumination. The scattering function $\gamma(\bar{r})$ represents the 3-D geometrical distribution and strengths of those visible *scattering centers* or *differential scattering cross-sections* of the body that give rise to the measured field. Correction of the field measured in practice in this fashion for range-phase, clutter, and system response [5],[6] leads to accessing $\Gamma(\bar{p})$ over those values of $\bar{p}$ employed in the measurement. We will designate the measured data manifold by $\Gamma_m(\bar{p})$ and assume without further elaboration here that the values of $\bar{p}$ utilized always sample the $\bar{p}$-space in a manner satisfying the Nyquist criterion to avoid aliasing in the reconstruction. The size and shape of the accessed Fourier region depends on geometry and on the extent of the spectral and angular apertures utilized i.e., on the values k and $(\bar{1}_R, \bar{1}_i)$. It is possible then as shown by computer simulation in [3] and [4] to retrieve tomographically a *diffraction and noise limited* version $\gamma_d(\bar{r})$ of the object scattering function through application of the *Projection-Slice Theorem* derivable from the multi-dimensional Fourier transform [7]-[10].

The aim of this paper is to show that high resolution reconstruction of $\gamma_d(\bar{r})$ is possible by measuring $\Gamma_m(\bar{p})$ over a curved surface in $\bar{p}$-space rather than within a volume as would ordinarily be required for the retrieval of 3-D detail of $\gamma_d(\bar{r})$. Because, for a given fixed spectral range, the number of angular observation points needed to adequately sample the $\bar{p}$-space over a volume is considerably higher than the number needed to access the outer surface of the volume or a portion of it, a sizable reduction in the number of coherent sensors or receivers is achieved. In practice this translates into a proportionate reduction in the projected cost of high resolution wavelength diversity imaging apertures and would for example, open the way for cost-effective implementation of envisioned [11] giant *imaging radar networks*.

II. Theoretical Considerations

Let $H(\bar{p})$ be a Fourier space sampling function describing the values assumed by the vector $\bar{p} = k(\bar{1}_R-\bar{1}_i)$ during data acquisition. We can express then the Fourier space data manifold accessed by measurement as,

$$\Gamma_m(\bar{p}) = \Gamma(\bar{p})\, H(\bar{p}) \tag{1}$$

which can be regarded as a *3-D Fourier transform hologram* of the scattering object. A diffraction and noise limited version $\gamma_d(\bar{r})$ of the object function $\gamma(\bar{r})$ can be obtained by Fourier inversion of eq. (1). That is (within a constant $1/(2\pi)^3$),

$$\gamma_d(\bar{r}) = \int \Gamma(\bar{p})H(\bar{p})\, e^{-j\bar{p}\cdot\bar{r}}\, d\bar{p} = \gamma(\bar{r}) *** h(\bar{r}) \tag{2}$$

where

$$h(\bar{r}) = \int H(\bar{p})\, e^{-j\bar{p}\cdot\bar{r}}\, d\bar{p} \tag{3}$$

is the 3-D *impulse response* or *point spread function* of the system and the triple asterisks denote a 3-D convolution. Clearly, because $H(\bar{p})$ (which can be now identified also as a *3-D transfer function* of the system) is dependent on recording geometry through $\bar{p} = k(\bar{1}_R-\bar{1}_i)$, the impulse response here, in contrast to conventional monochromatic imaging systems, is *spatially variant*. A valid question then is the identification of favorable recording geometries for which a narrow $h(\bar{r})$ is realized for a wide range of object bearings utilizing a minimum number of observation and/or illuminating points i.e., $(\bar{1}_R,\bar{1}_i)$ values in order to keep to a minimum the number of broadband coherent receivers and transmitters employed in the recording geometry. To provide an answer to this question we apply the projection-slice theorem to eq. (3). There are two forms of this theorem. One states that a projection (central slice) in Fourier space and a central slice (projection) in object space are a Fourier transform pair. The second form establishes a similar relationship between parallel *weighted projections* and parallel slices in the two domains [3],[9]. In the context of this analysis, the first version means that the 2-D Fourier transform of the projection of $H(\bar{p})$ on an arbitrarily oriented plane in $\bar{p}$-space is a central slice through $h(\bar{r})$ oriented parallel to the projection plane. This immediately suggests that desirable recording geometries are those for which the projection of their $H(\bar{p})$ in any direction cover always extended areas whose 2-D Fourier transform will necessarily be concentrated in a narrow region indicating an $h(\bar{r})$ with central slices exhibiting peak amplitudes of narrow extent. If all central slices of $h(\bar{r})$ possess peaks of narrow extent the 3-D impulse response $h(\bar{r})$ will consequently be narrow. With this condition established, we consider next the two bistatic recording geometries shown in Fig. 1. In one (a) a randomly or regularly sampled circular recording aperture of diameter D is used to access a truncated conical volume in $\bar{p}$-space with the truncation being set by the initial and final values of the range of wavenumbers k utilized in the measurement. In the second geometry (b), a number of random or equally spaced sampling points or coherent receivers distributed in a circle of diameter D are employed to access an identically shaped hollow truncated cone. Both geometries assume a centrally located coherent transmitter or illuminator T. The sampling functions $H(\bar{p})$ realized in both cases will coincide over the sidewalls of the truncated cones. A brief study of the two cases reveals that the shape and extent of the areas covered by nearly all projections of the solid truncated cone and the hollow truncated

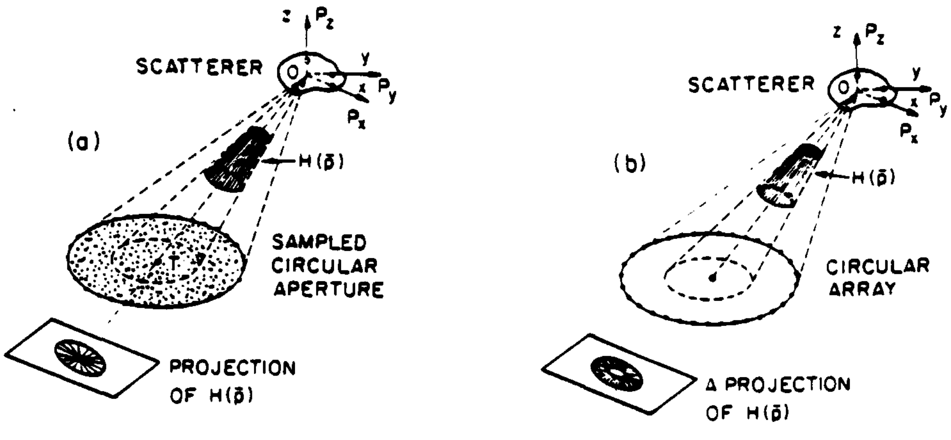

Fig. 1. Geometries for accessing the Fourier space of a 3-D scatterer. (a) with a sampled 2-D circular aperture, (b) with a circular array of sampling points.

cone are the same except for a few projections in those directions forming a small solid angle surrounding the OT Line where the hollow nature of $H(\bar{p})$ in (b) will be evidenced by a missing central region. This difference is illustrated by the two projection examples included in Fig. 1. However, because the outer boundaries of comparable projections of $H(\bar{p})$ in (a) and (b) are identical, the associated Fourier transforms representing the slices of $h(\bar{r})$ for both geometries are expected to possess central peaks of the same extent. The amplitude and shape of side-lobe structure in the outlying regions surrounding the central peaks will however differ somewhat because of the different number and distribution of data points in the comparable projections. It can be concluded therefore that the 3-D resolutions obtained with data accessed over a volume of $\bar{p}$-space and with data accessed over the outer surface of the volume are nearly the same. Verification of this conclusion is found in the results of a numerical simulation of microwave wavelength diversity imaging [3] which are presented in Fig. 2. A semi-circular array of sampling points consisting of 50 equally spaced receivers distributed over an arc of 130° as depicted in Fig. 2(a) is assumed. A 3-D test object consisting of two adjoining 1m diameter conducting spheres arranged as shown and centered at a distance R directly above the transmitter T is chosen. A spectral range of (2-4) GHz and a ratio of $R/D = 1$ are assumed in computing $\Gamma_m(\bar{p})$. The far field scattered by the two spheres was computed using the Mie series formulation [12]. Weighted parallel projections in the direction p_z of the accessed $\bar{p}$-space data manifold lying on a truncated semi-conical surface represented by $H(p)$ in Fig. 2(a) were obtained by multiplying $\Gamma_m(\bar{p})$ by the complex factor $\exp j(\alpha p_z)$, $\alpha = 0$, -30cm, -40cm, before computing the projections. This yields three weighted projection holograms shown to the left in Fig. 2(b) that correspond from top to bottom to parallel horizontal slices through the object in Fig. 2(a) at $z = 0$, -30cm and -40cm. The optically retrieved images from these projection holograms are shown to the right in Fig. 2(b). These demonstrate clearly the 3-D tomographic imaging capability from the limited p-space data accessed by the geometry of Fig. 2(a).

III. Acknowledgement

This research was supported by the Army Research Office under contract DAAG-29-80-K-0024P02 and by the Air Force Office of Scientific Research, Air

Force Systems Command under grant AFOSR-81-0240B.

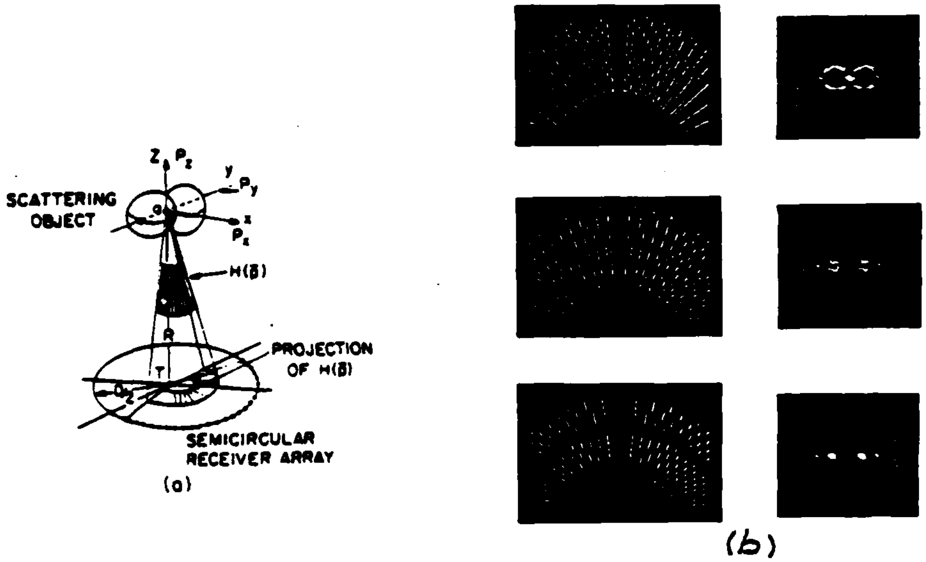

Fig. 2. Details of numerical simulation of 3-D tomographic image reconstruction from limited Fourier space data. (a) Recording geometry (b) Weighted projection holograms (left) and retrieved images of three slices through the illuminated portion of the two spheres.

References

1. N. Bojarski, Naval Air Command Final Report, N00019-73-C-0312F, Feb. 1974.
2. R.M. Lewis, IEEE Trans. on Ant. and Prop., Vol. AP-17, pp. 308-314, May 1969.
3. C.K. Chan and N. Farhat, IEEE Trans. on Ant. and Prop., Vol. AP-29, pp. 312-319, March 1981.
4. N.H. Farhat and C.K. Chan, "Three-Dimensional Imaging by Wave-Vector Diversity", Presented at the 8th Int. Symp. on Acoust. Imaging, Key Biscayne, Fla. 1978, and published in *Acoustical Imaging*, Vol. 8, A. Metherell (Ed.), pp. 499-516, Plenum Press, New York 1980.
5. N.H. Farhat and C.L. Werner, "An Automated Microwave Measurement Facility For Three-Dimensional Tomographic Imaging by Wavelength Diversity", Presented at the 1981 Intern. IEEE AP-S Symp./Nat. Radio Science Meeting, L.A., June 1981.
6. N.H. Farhat, C.L. Werner and T.H. Chu, "Microwave Projection Imaging With Near Optical Resolution", Submitted for publication, IEEE Trans. on Ant. and Propagation.
7. J. Radon, Ber. Saechs. Akad. Wiss. (Leipzig), Vol. 19, pp. 262-278, 1917.
8. R.N. Bracewell, Australian J. of Phys., Vol. 9, pp. 198-217, 1951.
9. G. Stroke and M. Halioua, Trans. Amer. Crystal. Assoc., Vol. 12, pp. 27-41, 1976.
10. H.H. Barrett and W. Swindle, "*Radiological Imaging: Theory and Image Formation, Detection and Processing*, Acad. Press, New York, 1982.
11. N.H. Farhat, W.I. Landauer and W.E. Wallace, "Computer Assisted Naval Applications of Holography", Computer Command and Control Co., Report No. 132-4, prepared for the Naval Analysis Program, Office of Naval Research, under contract N0014-69-C-0167, Feb. 1973.
12. R.F. Harrington, "*Time Harmonic Electromagnetic Fields*, McGraw-Hill, 1961.

APPENDIX IV

THE SCALING PROPERTY OF THE 3-D FOURIER TRANSFORM AND ITS IMPLICATION IN ANGULAR AND SPECTRAL SAMPLING OF $\Gamma(\overline{p})$

APPENDIX IV

THE SCALING PROPERTY OF THE 3-D FOURIER TRANSFORM AND ITS IMPLICATION IN ANGULAR AND SPECTRAL SAMPLING OF $\Gamma(\bar{p})$

As in the one dimensional Fourier transform a change of scale in 3-D object space by factor m results in a change of scale by factor 1/m in 3-D Fourier space. This is readily seen by starting with the 3-D Fourier transform relation,

$$\int \gamma(\bar{r})\, e^{j\bar{p}\cdot\bar{r}}\, d\bar{r} = \Gamma(\bar{p}) \tag{1}$$

between the object function $\gamma(\bar{r})$ and its corresponding Fourier space data $\Gamma(\bar{p})$. Then by changing $\bar{r}$ to $m\bar{r}$ in $\gamma(\bar{r})$ we uniformly scale the object by a factor m. Magnification occurs for $m < 1$ and minification for $m > 1$. The Fourier transform of the scaled object is,

$$\begin{aligned} \int \gamma(m\bar{r})\, e^{j\bar{p}\cdot\bar{r}}\, d\bar{r} &= \frac{1}{m} \int \gamma(m\bar{r})\, e^{j\frac{1}{m}\bar{p}\cdot(m\bar{r})}\, d(m\bar{r}) \\ &= \frac{1}{m} \int \gamma(\bar{\xi})\, e^{j\frac{1}{m}\bar{p}\cdot\bar{\xi}}\, d\xi \qquad (2) \\ &= \frac{1}{m}\, \Gamma\!\left(\frac{1}{m}\bar{p}\right) \end{aligned}$$

where $\xi = m\bar{r}$.

Equation (2) can be written in abbreviated form,

$$\gamma(m\bar{r}) \overset{F\cdot T}{\leftrightarrow} \frac{1}{m}\, \Gamma\!\left(\frac{1}{m}\bar{p}\right) \tag{3}$$

Changing the scale of the 3-D object function by a factor m results therefore in scaling its 3-D Fourier space manifold by 1/m. Note when $m < 1$

and $\gamma(m\bar{r})$ is therefore a magnified version of the object $\gamma(\bar{r})$, that $\Gamma(\frac{1}{m}\bar{p})$ represents a minified version of $\Gamma(\bar{p})$. This means that increasing the object size m times while keeping fixed all other parameters of the imaging experiments conducted in our work, will lead to a proportionate contraction of the Fourier pattern Γ. This means that tighter angular and spectral sampling intervals of the scattering pattern of the object would be required as compared to that before scaling if undersampling and undesired aliasing are to be avoided. This conclusion is important for scaling the results of imaging studies carried out in our anechoic chamber facility, with reduced scale models of test objects of interest, to imaging the original objects themselves. Further discussion of the effect of scaling on the angular sampling requirement based on the scaling property in eq. (2) is given in Section 4.5.

APPENDIX V

PROJECTION THEOREMS AND THEIR APPLICATION IN MULTIDIMENSIONAL SIGNAL PROCESSING

(Reprint of paper presented at the 1983 SPIE Technical
Symposium on Advances in Optical Information Processing,
L.A., Jan. 1983)

388-19

Projection theorems and their application in multidimensional signal processing

N.H. Farhat, C. Yi Ho and Li Szu Chang

University of Pennsylvania, Electro-Optics and Microwave-Optics Laboratory
The Moore School of Electrical Engineering, Philadelphia, PA., 19104

Abstract

Several sophisticated imaging methods are based on measurements that lead to accessing a finite volume of the 3-D Fourier domain of an interrogated object and subsequent retrieval of 3-D image detail by 3-D Fourier inversion. Examples are found in *inverse scattering, integral holography, x-ray and radio-emission imaging, crystalography*, and *electron microscopy*. This paper examines a unified approach to all these methods, namely through reduction of dimensionality based on the *projection-slice* property of the multidimensional Fourier transform. We describe two hybrid (opto-digital) computing schemes, one employing coherent light and the other incoherent light, that can be used with these techniques to reconstruct and display true 3-D image detail tomographically. Reduction of dimensionality is shown to provide flexibility in hybrid (opto-electronic) computing by permitting trade-off between the degree of parallel and serial processing employed. It leads to new architectures capable of enhanced throughput and dynamic range and extends the domain of optical computing beyond one and two dimensional signals.

1. Introduction

Inverse methods involve inferring information about the geometrical and material properties of an object by remote probing with electromagnetic, acoustic, or particle beams. Several inverse methods for example in optics [1]-[8], microwaves [9]-[13], crystallography and electron microscopy [14], computerized axial tomography [15], ultrasonics [16] and integral holography [17] lead to accessing a finite volume in the 3-D Fourier space of the object and subsequent retrieval of 3-D image detail via 3-D Fourier inversion. The required 3-D Fourier transform can naturally be carried out digitally by means of a 3-D fast Fourier transform algorithm. This approach may not be fast enough for certain applications even with the fastest array processors available today especially when one is dealing with the large amounts of data associated with complicated objects. This can prevent real-time image reconstructions and display. Furthermore the inherent two dimensionality of present day computer displays precludes true 3-D image display limiting the presentation of 3-D image detail to perspectives, individual slices or cross-sectional outlines.

To overcome these limitations several techniques for 3-D display of television and computer generated signals have been proposed and demonstrated [18]-[20].

In this paper we consider a new approach to true 3-D image reconstruction and display. Two methods that employ hybrid (opto-digital) computing and do not require viewing aids are described. Both methods are based on reducing a 3-D Fourier space manifold into a series of 2-D *projection holograms* each corresponding to a different parallel slice of the object and on using the optical 2-D Fourier transform in a space-time multiplex scheme to retrieve rapidly and sequentially images of the various slices. The reconstructed slices are displayed on an oscillating screen in the proper sequence to form the 3-D image *tomographically*. One method employs coherent optical computing to perform the required 2-D Fourier transforms while a novel incoherent opto-electronic computing scheme based on spatial domain projections is employed in the other.

The processing of multi-dimensional signals by reduction of dimensionality via projection was first considered by Radon [21]. Since then projection methods have been employed in the processing of 2-D radio-astronomical data by Bracewell [22],[24] and in hybrid (opto-digital) processing of 3-D data by Stroke, Halioua, and co-workers [14],[16],[24] in the context of crystallography, electron microscopy and ultrasonics and by Farhat and Chan [12],[13] and Das and Boerner [41] in the context of 3-D microwave imaging and radar shape estimation.

Comprehensive treatments and applications of multidimensional signals processing via projections has been given by Mersareau and Oppenheim [25] in the context of digital signal processing and more recently by Barrett [26]-[28] and Farhat [29] in the context of optical data processing.

2. The projection-slice theorem

The principle underlying the two hybrid 3-D image reconstruction and display techniques discussed in this paper is the *projection-slice theorem* associated with the multidimensional Fourier transform [22],[23]. Given a multidimensional object function and its Fourier transform the projection-slice theorem states that a projection (slice) in Fourier space and a "parallel" slice (projection) in object space are a Fourier transform pair. In other words projections in object space correspond, in the Fourier transform sense, to "parallel" slices in Fourier space taken in planes parallel to the projection planes and visa versa, i.e., projections in Fourier space correspond in the Fourier transform sense to "parallel" slices in object space.

There are two forms of the projection-slice theorem. One form deals with *meridional* or *central* slices and corresponding projections on planes parallel to them, while the second form deals with weighted parallel projections made always on the same plane and corresponding slices at different depth all parallel to the one projection plane.

A derivation of the two forms of the projection-slice theorem is given in Appendix I in terms of a 3-D object function $\gamma(\bar{r})$ and its 3-D Fourier transform $\Gamma(\bar{p})$ where $\bar{r}$ and $\bar{p}$ designate position vectors in object space and Fourier space respectively. The object characteristic function $\gamma(\bar{r})$ can represent the object attenuation function as in x-ray imaging, or surface reflectivity as in integral holography and microwave imaging of reflecting objects, or refractive index distribution or velocity distribution as in electromagnetic and acoustic inverse scattering. Thus for example in x-ray tomography, projections of the object function $\gamma(\bar{r})$ are obtained by transmission measurements of absorbed x-rays while in integral holography photographs of the object taken from different aspect angles represent the set of projections. The projection-slice theorem is invoked then to obtain either by digital or optical means central slices of the Fourier domain $\Gamma(\bar{p})$ extending over a finite region of the Fourier space of the object.

In inverse scattering, complex (amplitude and phase) measurements involving wave-vector diversity (i.e., angular and spectral diversity) are used to determine $\Gamma(\bar{p})$ directly over a finite volume of Fourier space [9]-[13].

Thus the measurements performed and the subsequent data preprocessing in all of these methods aim at accessing a finite volume of the 3-D Fourier space of the object represented by $\Gamma(\bar{p})$. Once $\Gamma(\bar{p})$ has been determined, 3-D image detail representing a finite resolution version of $\gamma(\bar{r})$ can be retrieved as pointed out earlier via a 3-D inverse Fourier transform. In the following section we will describe two hybrid techniques for tomographic image reconstruction and display of the 3-D object function $\gamma(\bar{r})$ in which the required 3-D inverse Fourier transform is carried out optically as a series of 2-D Fourier transforms of projection holograms employing either coherent light or incoherent light.

3. Tomographic image reconstruction and 3-D display

Both coherent and incoherent optical computing can be used to carry out sequentially and rapidly the 2-D Fourier transforms of a series of weighted projection holograms corresponding to parallel equally spaced slices or cross-sectional outlines of the object in order to visualize its 3-D image tomographically.

Coherent scheme:

One such scheme employing the virtual Fourier transform has been described earlier [30]. The disadvantage of this scheme was that only one observer at a time can view the displayed virtual 3-D image. To overcome this limitation the arrangement shown in Fig. 1 was considered. This arrangement makes use of the real optical Fourier transform to project the reconstructed images of the various slices of the object rapidly and in proper sequence on an axially oscillating projection surface. The 3-D image reconstructed tomographically in this fashion can be viewed simultaneously by several observers from different directions. The arrangement consists of a convergent laser beam produced by a long focal length lens. The beam interrogates sequentially and rapidly a series of projection holograms mounted as shown on a rotating hologram bearing wheel. The axially oscillating projection surface is pro-

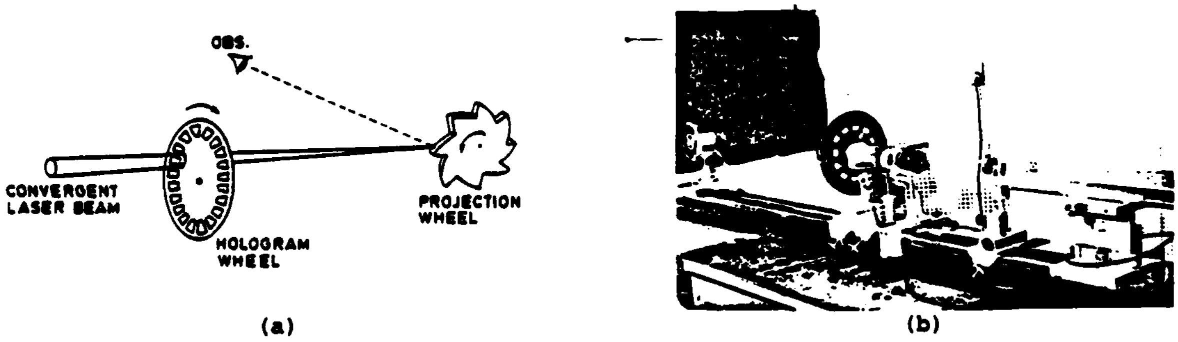

(a) (b)

Fig. 1. Scheme for 3-D image reconstruction and display from a sequence of projection holograms. (a) Principle, (b) Pictorial view of system showing laser source to the right, hologram bearing wheel in the center and projection wheel to the left. Projection wheel is 25 cm in diameter and contains 24 windows for mounting the projection holograms.

duced by rotating a suitably shaped projection wheel. The realization of a rapidly oscillating projection surface with this wheel is based on the eccentric rotation of a cylindrical surface. If a cylinder rotates eccentrically about an axis parallel to but displaced from the axis of the cylinder an observer will see the surface of the cylinder moving back and forth at the same rate of rotation. When a number, say eight, of such cylinders or cylindrical segments of the same radius are arranged together as shown in the projection wheel of Fig. 1(a) with their centers spaced evenly on the circumference of a circle centered on the axis of rotation, the same oscillating surface effect is observed but at eight times the rotation rate [31]. This permits the achievement of higher rates of projection surface displacement using reasonable rotation speeds that can be furnished by ordinary stepper motors. A pictorial view of the projection wheel used is shown in Fig. 2. Both the hologram bearing wheel and the projection wheel are driven by computer controlled stepper motors to maintain synchronization. Examples of the true 3-D image reconstruction and display achievable with this arrangement are shown in Fig. 3. Photographs of two views of the displayed 3-D image taken from two different aspect angles are shown in (a) and (b). The projection holograms used in the experiment were those of the eight point scatterer test object used in our earlier work [30]. Two identical views of a model of the test object are shown in (c) and (d) of Fig. 3 for comparison.

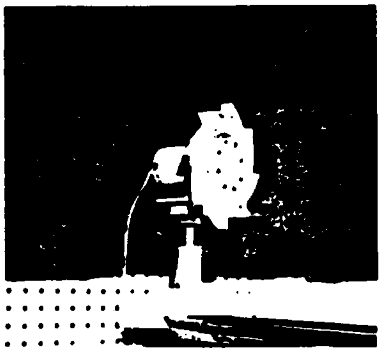

Fig. 2. Pictorial view of projection wheel used to realize an axially oscillating projection screen. A volumetric display region of 1.8 cm x 1.8 cm x 1.8 cm is provided.

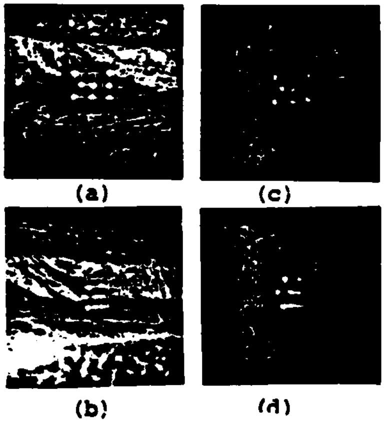

Fig. 3. Two views (a) and (b) of the tomographically reconstructed 3-D image of an eight point test object and identical corresponding views (c) and (d) of a model of the test object.

Incoherent scheme:

The second optical 3-D image reconstruction and display scheme studied is based on performing the required 2-D Fourier transforms directly on weighted projection holograms displayed in spatially incoherent light. This approach enables direct 2-D Fourier transformation of the CRT computer displays of weighted projection holograms corresponding to the different slices of the object. Being opto-electronic in nature the scheme permits displaying the image slices obtained by Fourier inversion in rapid succession on a second CRT display. A 3-D tomographic display of the displayed image slices can be realized employing a projection lens and the oscillating projection screen idea used in the preceeding scheme.

Several methods for incoherent 2-D Fourier transformation appear in the literature. These include shadow casting techniques using a two Fresnel zone masks as a Fourier analyzer [32], [33], achromatization [34], and opto-electronic methods utilizing optical multiplication by sine and cosine masks followed by electronic detection of the spatially integrated products [35]-[37]. A major advantage of these techniques is their freedom from speckle noise which is a known limitation of coherent optical processing. There are disadvantages however. Major among them is the complexity of carrying out complex operations and the low Fourier plane contrast in the Fresnel zone shadow casting scheme. There is also the "dynamic bias" problem identified in [38] and [39]. To handle complex data and increase throughput the use of color multiplexing or wavelength diversity in opto-electronic schemes has been considered [40].

The opto-electronic scheme described below combines *spatial domain projections* and *wavelength or color diversity* to perform Fourier transform operations on 2-D complex functions representing for example projection hologram data displayed on a color CRT monitor. In addition the scheme has the advantage of overcoming the dynamic bias problem. It differs from all other previously studied schemes in its novel use of the *spatial domain projection* theorem in a two color wavelength diversity scheme and in its potential to execute 2-D discrete Fourier transforms of large data formats approaching 1000 X 1000 pixels at high speeds. Another important practical advantage is the compatibility with a color CRT as the input device with its high brightness and precise color pixel locations.

The *Spatial Domain Projection Theorem* (see Appendix I) was first introduced in radio astronomy by Bracewell [22]. Its use in the present scheme is discussed next.

Consider a complex spatial function f(x,y) with its 2-D Fourier transform $F(\omega_x,\omega_y)$, ω_x and ω_y being spatial frequency variables. Thus,

$$f(x,y) \leftrightarrow F(\omega_x,\omega_y) \tag{1}$$

designate a Fourier transform pair, where,

$$f(x,y) = \int_x \int_y F(\omega_x,\omega_y) e^{j(\omega_x x + \omega_y y)} d\omega_x d\omega_y \tag{2}$$

and

$$F(\omega_x,\omega_y) = \frac{1}{(2\pi)^2} \int_x \int_y f(x,y) e^{-j(\omega_x x + \omega_y y)} dxdy \tag{3}$$

The spatial projection of f(x,y) on the x-axis is defined as

$$f_p(x) \triangleq \int_y f(x,y)\, dy \tag{4}$$

or by using (2),

$$f_p(x) = \int_y \{(\int_{\omega_x} \int_{\omega_y}) F(\omega_x,\omega_y)\, e^{j(\omega_x x + \omega_y y)} d\omega_x d\omega_y\}\ dy \tag{5}$$

Carrying out the integration with respect to y first we obtain

$$f_p(x) = \int_{\omega_x} \int_{\omega_y} F(\omega_x,\omega_y)\, e^{j\omega_x x}\, \delta(\omega_y)\, d\omega_x\, d\omega_y \tag{6}$$

or by the "sifting" property of the δ function,

$$f_p(x) = \int_{\omega_x} F(\omega_x,0)\, e^{j\omega_x x}\, d\omega_x \tag{7}$$

i.e., in abbreviated form,

$$f_p(x) \leftrightarrow F(\omega_x,0) \tag{8}$$

This final result, known as the *spatial domain projection theorem*, states that the spatial projection $f_p(x)$ of f(x,y) and a central slice of its 2-D Fourier transform along a central line $\omega_y = 0$ are Fourier transform pairs. This suggests that the transform $F(\omega_x,\omega_y)$ can be obtained by a repeated application of the following three step process: (1) Rotate the object function f(x,y) in the x-y plane, by an angle $n\Delta\theta$ (n=1,2....N) relative to the x axis where $\Delta\theta = \frac{180°}{N}$, (2) form the projection on the x axis, and (3) one dimensional Fourier transform the projection to obtain the value of $F(\omega_x,\omega_y)$ along a central line passing through the origin of the ω_x-ω_y plane and making an angle $n\Delta\theta$ with the ω_x axis. By repeating the process for all the values of n=1,2 ... N = 180°/Δθ one can construct the transform $F(\omega_x,\omega_y)$ on a spoked format of radial lines of angular spacing Δθ. Obviously this three step procedure can be implemented entirely digitally to provide a new discrete Fourier transform algorithm. Alternately the one dimensional Fourier transform required in the third step can be carried out with an analog CCD or SAW device [42]. Here an arrangement for performing the three step procedure opto-electronically is presented.

The arrangement is sketched in Fig. 4. The complex function f(x,y) is displayed on a color CRT or TV screen. Two of the three available primary colors, (red, blue and green) are assigned to the real part $f_r(x,y)$ and the imaginary part $f_i(x,y)$ of f(x,y) with the third color left unused or possibly reserved for use in an error correction scheme for enhancing the accuracy of the processor. The color display is imaged on the input face of an idealized tapered coherent fiber bundle C.F.B. 1 which performs the required projection operation by integrating or fusing the image in the vertical direction into a line image while reserving detail horizontally furnishing thus the projection $f_p(x)$ at its sharp edge. The complex nature of $f_p(x)$ is preserved in a two color display at this end. Image rotation is achieved by rotating the dove prism in the projection and image rotating segment which merely acts as a rotating image coupler. The C.F.B. 2 and C.F.B. 3 spread $f_p(x)$ vertically in the y direction while preserving detail in the horizontal x direction. Note that this does

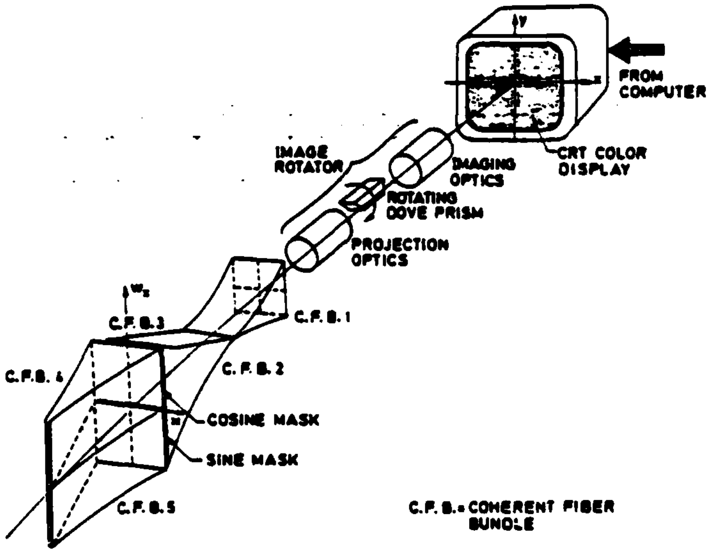

Fig. 4. High throughput incoherent 2-D complex fourier transformer based on the spatial domain projection theorem.

not restore the function f(x,y) but merely smears or "back-projects" the two colored $f_p(x)$ in the vertical direction uniformly. Later we shall see how the vertical projection operation and the vertical smearing or back-projection operation can be implemented simultaneously with a single anamorphic optical system.

In accordance to eq. (7) we seek the transform,

$$F(\omega_x,o) = \int f_p(x)\, e^{j\omega_x x}\, dx$$

$$= \int\{f_p^{\,r}(x) + j\, f_p^{\,g}(x)\}\{\cos \omega_x x + j\sin\omega_x x\}\ dx \tag{9}$$

$$= \int\{f_p^{\,r} + jf_p^{\,g}(x)\}\ \cos \omega_x x\, dx$$

$$+ \int\{jf_p^{\,r}(x) - f_p^{\,g}(x)\}\ \sin \omega_x x\, dx \tag{10}$$

Thus we need to multiply the complex function $f_p(x) = f_p^{\,r}(x) + jf_p^{\,g}(x)$ (where the real part is say coded in red and the imaginary part in green) by cos $\omega_x x$ and sin $\omega_x x$ and integrate the multiplication results with respect to x all this while preserving color discrimination. In practice this can be accomplished by placing at the input faces of C.F.B. 4 a cosine mask and at the input face of C.F.B. 5 a sine mask. The cosine and sine masks are neutral density transparencies that influence both colors equally. In practice the transmittance of the sine/cosine masks which are computer generated is positive real given by (1 + cos $\omega_x x$) respectively. Similarly because the functions $f_p{}^r(x)$ and $f_p{}^i(x)$ are to be represented as spatial intensity variations of incoherent light, one say with red light the other with green, bias terms must be added to handle negative values. Therefore in practice equation (10) assumes the form,

$$F(\omega_x,0) = \int\{[b^r + f_p^{\,r}(x)] + j\ [b^g + f_p^{\,g}(x)]\}(1 + \cos\omega_x x)\ dx$$

$$+ \int\{j[b^r + f_p^{\,r}(x)] - [b^g + f_p^{\,g}(x)]\}\ (1 + \sin\omega_x x)\ dx \tag{11}$$

$$= \int[b^r\ (1+ \cos\omega_x x) - b^g\ (1 + \sin\omega_x x)]\ dx + j\int[b^g(1 + \cos\omega_x x)$$

$$+\ \ b^r\ (1 + \sin\omega_x x)]\ dx + \int[f_p^{\,r}(x) - f_p^{\,g}(x)]dx + j\int[f_p^{\,r}(x) + f_p^{\,g}(x)]\ dx$$

$$+ \int[f_p^{\,r}(x) + j\ f_p^{\,g}(x)]\ \cos\omega_x x\ dx + \int[jf_p^{\,r}(x) - f_p^{\,g}(x)]\ \sin\omega_x x\ dx \tag{12}$$

where b^r and b^g are constant bias terms that enable us to represent the bipolar functions $f_p{}^r$ and $f_p{}^g$ by positive real red and green light intensities respectively. In eq. (12) the first and second integrals represent constant d.c. bias terms appearing in the output of the processor. This d.c. bias which has the effect of reducing contrast can eventually be removed by electronic filtering. The third and fourth integrals represent a signal dependent *dynamic bias* term. The fifth and sixth integrals are those of eq. (10) which represent the desired Fourier transform output. While electronic filtering of the d.c. bias term is a straight forward matter, it is not easy to remove the dynamic bias term because of its signal dependent nature. The presence of this term is undesirable since it behaves as noise signal that limits the dynamic range of the processor. A method for eliminating this bias term will be described below. The location of the two transparencies or masks together with the direction of the x and ω_x axis are shown in Fig. 4. Note that because of their neutral density (black and white) nature the screens will spatially modulate the two colors of $f_p(x)$ equally. That is the real and imaginary parts of $f_p(x)$ are each multiplied by the required cosine and sine kernels in accordance to eq. (10). The function of the idealized C.F.B. 4 and 5 is to perform the required integration in the x direction called for in eq. (10) after the multiplications in the integrand. The output data at the sharp vertical edge of C.F.B. 4 will therefore consist of two colors with the data in the two colors corresponding to the real and imaginary parts of the cosine transform of $f_p(x)$. Similarly the vertical distribution of the two colors appearing at the sharp edge of C.F.B. 5 will correspond to the real and imaginary parts of the sine transform of $f_p(x)$. Suitable color selective detection of the outputs of C.F.B. 4 and C.F.B. 5 for example with a color T.V. camera or by imaging the outputs on 4 self-scanned line detector arrays through a dispersive prism would yield four electronic signals representing the terms in eq. (11). These can be combined appropriately to obtain separately the real part and the imaginary of $F(\omega_x,o)$ and the process repeated as the image is rotated in steps. A high precision absolute angle encoder coupled to the rotating prism is used to provide signals that can be employed in displaying the transform line at the correct angle $n\Delta\theta$ relative to the ω_x axis on a CRT display providing thus $F(\omega_x,\omega_y)$ in successive central slices. Because of the high brightness of present day color displays, the flexibility of digital video processors that can be used to address them, the minimization of diffraction effects that give rise to cross-talk through the use of fiber optics technology and the high bandwidth of self-scanned detector arrays and their time integrating features we expect this 2-D optical D.F.T.* approach to yield high throughputs.For example a conventional color CRT such as the RCA RG511 provides 800 x 800 color pixels. This means that at the customary frame rate of 30/sec we can introduce 800 x 800 x 30 = $1.92\ 10^7$ complex data points/sec in the processor. The actual time required to perform a 2-D complex D.F.T. on the 800 x 800 complex data points would be determined by the rotation rate of the image which equals twice the rotation rate of the dove prism (a well known property of the dove prism).

Several image rotating techniques can be used. These include: digital, electron-optical, and opto-mechanical. Although digital and electron-optical schemes are inertialesss and therefore can offer high image rotation rates, a somewhat slower opto-mechanical scheme was found adequate for the present study and was therefore adopted because of its simplicity and much lower cost. The scheme is based on the well known image rotating property of the dove prism. A dove prism image rotator was therefore designed and constructed. Two pictorial views of the completed dove prism image rotator are shown in Fig. 5. In this design

Fig. 5. Two pictorial views of dove prism image rotator and stepper motor drive.

the dove prism (a Rolyn model 45.030 of dimensions 30xmmx30xxml30mm) is mounted within the inner cylinder of a high precision ball bearing. The center cylinder of the bearing is rotated with respect to the outer part which is held stationary. Rotation was achieved with the aid of precision 1:1 belt drive powered by a computer controlled stepper motor capable of performing up to 20,000 half steps of .9° each per second. Means are furnished for centering and axial alignment of the dove prism within the inner cylinder of the ball bearing with the aid of adjustable screws. An example of the image rotating capability of the

---

*Discrete Fourier transform

image rotator is shown in the top part of Fig. 7. Three rotated images of a test, object shown in Fig. 6, are presented. These correspond to dove prism rotation angles of 0°, 45° and 90° respectively (recall that a dove prism rotation of θ° results in an image rotation of 2θ°).

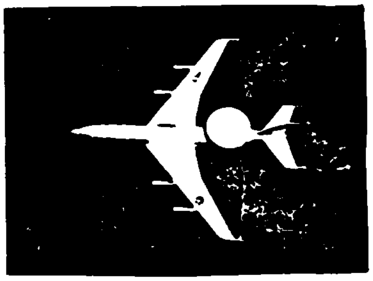

Fig. 6. Test object

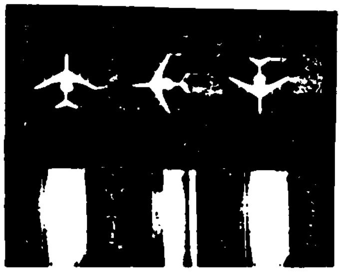

Fig. 7. Three rotated images of test object (top) and their vertically smeared versions (bottom).

Vertical image integration and spreading were to be carried out as originally proposed in Fig. 4 with the aid of tapered coherent fiber bundles CFB1, CFB2 and CFB3. It is clear that specialized and costly techniques are required in the manufacture of such idealized coherent fiber bundles with the required property. In practice a simple anamorphic optical system shown in Fig. 8, can be used to perform the function of the coherent fiber bundles CFB 1,2 and 3. The arrangement shown in Fig. 8 makes use of a single cylindrical lens to vertically smear the image i of any object scene 0. This smearing operation replaces the required vertical integration (spatial projection) and vertical spreading operations at the same time. Obviously this approach is more realistic and much less costly than the one calling for coherent fiber bundles and is therefore more attractive. In the scheme shown, spherical lens L_1 images the object scene 0 onto the image plane with a magnification $m = S_2/S_1 = h'/h$. The object scene 0 in Fig. 8 represents the rotated image furnished by the dove prism image rotator and its imaging optics (see Fig. 4). The cylindrical lens L_2 is added to smear the image vertically. The height h' of the vertically smeared image depends on the values of S_1, S_2, S_3 and the focal lengths F_1 and F_2 and on the height h of the original scene. The lower part of Fig. 7 is a pictorial record of the vertically smeared versions of the three rotated images shown in the upper part of the figure. These were obtained with the arrangement of Fig. 8 with the following parameter values: $S_1 = 40$ cm, $S_2 = 14.5$ cm, $S_3 = 5$ cm, $F_1 = 10.5$ cm, $F_2 = 4.1$ cm, and $h = 5.5$ cm. Excellent uniformity of the smeared image in the vertical direction is achieved. In the scheme of Fig. 4 a vertically smeared image similar to those shown in Fig. 7 would be projected onto the sine/cosine mask to perform the multiplication required in the integrands of eq. (10). In this fashion the vertical projection (integration) and spreading of the image rotated by the dove prism in Fig. 4 are accomplished simultaneously by the anamorphic optical system of Fig. 8 resulting in great simplification of the input portion of Fig. 4.

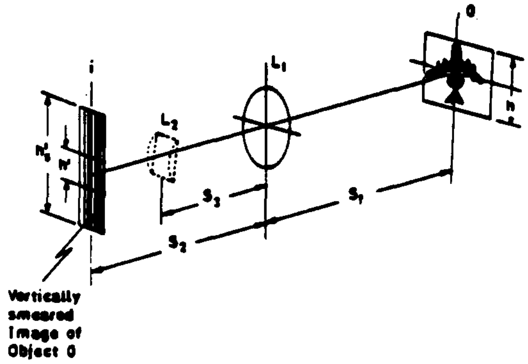

Fig. 8. Anamorphic optical system for vertical image smearing.

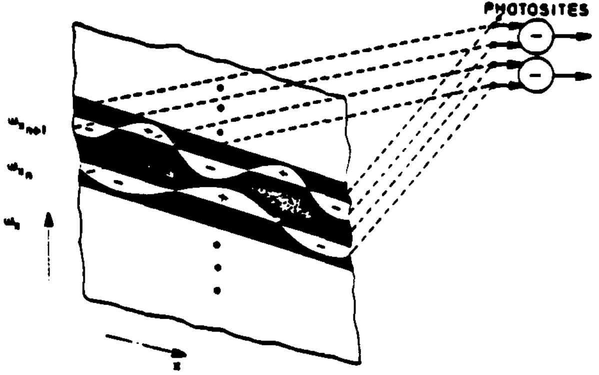

Fig. 9. Detail of transmission pattern on sine/cosine screen capable of eliminating dynamic bias problem.

Generation of the required sine and cosine masks was achieved with the aid of a DEC Modular Instrumentation Computer (MINC) 11/2 and a high resolution Tektronix model 606A CRT display. A novel scheme was employed in the generation of the sine and cosine mask patterns which has the significant potential for eliminating the *dynamic bias problem* known to be a limiting factor in the operation of incoherent Fourier transform schemes [38],[39]. This approach to elimination of the dynamic bias problem takes advantage of the vertical uniformity of the smeared image projected on the sine/cosine mask to synthesize the equivalent of a negative transmittance with incoherent light. The scheme is opto-electronic in nature since it involves differential readout of the linear photodetector output shown in Fig. 4 in order to synthesize the negative transmittance. The *dynamic bias problem* stems directly from the fact that, aside from its spectral content, incoherent light can be represented by its intensity only which is positive real. Similarly the transmittance of any photographic transparency (such as the sine/cosine masks in our scheme) in incoherent light is also positive real. Therefore to represent a bipolar function that can assume negative values bias terms must be added as discussed earlier. The addition of these bias terms in the treatment above has been shown (see eq. (12)) to lead in the transform $F(\omega_x,0)$ to a d.c term, which can easily be filtered out in an electronic readout scheme, plus an undesirable signal dependent, dynamic bias term, which can not be excluded from the output without resort to complicated adaptive filtering. The presence of this undesirable signal dependent term can be considered as noise and will therefore limit the dynamic range of any incoherent optical processor. It's elimination would increase dynamic range and enhance performance. Our method for the elimination of the dynamic bias term is represented in Fig. 9 which shows the cosinusoidal transmittance of a portion of the sine or cosine masks at two adjacent frequencies ω_{x_n} and $\omega_{x_{n+1}}$. The black areas represent opaque portions. As the vertically smeared version of the rotated image in Fig. 8 is caused to impinge on such a screen the transmittance at each value of x will be proportional to the height of the cosinusoidal aperture at that value of x. By focusing the light emerging from the positive half cycles and the negative half cycles of each spatial frequency ω_{x_n} (as depicted symbolically in Fig. 9 by the dashed lines) on adjacent photosites of the self scanned linear detector array (or arrays) reading the output $F(\omega_x,0)$ of the processor and subtracting the output of the detectors at these sites we essentially make the transmittances of the upper and lower half cycles of each spatial frequency of opposite sign realizing thereby a bipolar transmittance in incoherent light opto-electronically. It is indeed fortunate that many linear self scanned detector arrays marketed today (e.g. Reticon's and Fairchild's) lend themselves for use in this scheme because normally the even numbered photosites are read-out with one shift register while the odd numbered photosites by another. By substracting the outputs of the two shift registers, instead of adding them as done in normal use, the above output readout scheme can be realized immediately.

Figure 10 is an example of a sine/cosine mask that makes use of the above encoding concept. This particular mask was produced on our high resolution computer display for use with a 256 element detector array. The sine and cosine portions of the mask each contain spatial frequencies extending from -34 to +34. Each frequency requires the use of two detector photosites for dynamic bias suppression.

Fig. 10. Computer generated sine/cosine mask.

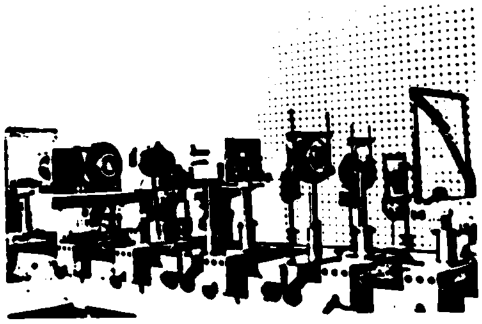

Fig. 11. Pictorial view of incoherent fourier transformer. From left: object scene, dove prism image rotator, imaging lens, cylindrical lens for vertical image smearing and sine/cosine screen, followed by output part consisting of anamorphic spherical/cylindrical lens system.

The preceeding discussion suggests a modified version of the scheme of Fig. 4 for implementing the spatially incoherent Fourier transform. This modified version is shown in

Fig. 12 and in the pictorial view of Fig. 11. The output portion of the modified arrangement comprised of components downstream from the sine/cosine mask, makes use of a second anamorphic optical system consisting of a spherical lens L_3/cylindrical lens L_4 combination, instead of the coherent fiber plugs CFB4 and CFB5 in the original configuration of Fig. 4, to horizontally integrate light emerging from the positive and negative half cycles of each spatial frequency component in the masks onto pairs of adjacent photosites in the output self scanning detector arrays D_G and D_R. The dispersive prism (or alternatively a dichroic beam splitter) is used to separate the two colors (red and green) onto the self scanning detector arrays. In this anamorphic output segment of the processor, spherical lens L_3 images the output of the sine/cosine mask on the plane of the output detectors while the addition of the cylindrical lens power in the horizontal direction only focuses the image detail horizontally over a width equal to the width of the detector. Selection of lenses L_1 and L_2 and the various spacing between components can be made by referring to the anamorphic system representation of Fig. 13. Figure 13 also suggests that detector arrays with the largest available width w' are desirable since a large w' relaxes both the focusing requirement from the horizontally integrating lens and the horizontal demagnification of the system. The widest commercially available w' is that of Reticon S-series (Spectroscopic) self scanning detectors with w'=2.5mm. This family of detectors also has separate odd/even shift register output capability permitting dynamic bias elimination and have a wide bandwidth and dynamic range which makes them ideal for this application.

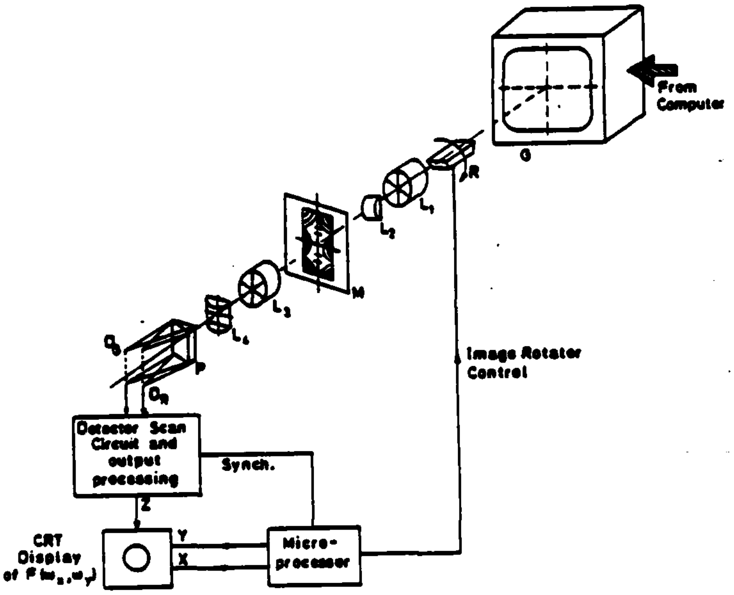

Fig. 12. Incoherent fourier transform scheme employing spatial domain projections and color diversity to perform complex transforms.

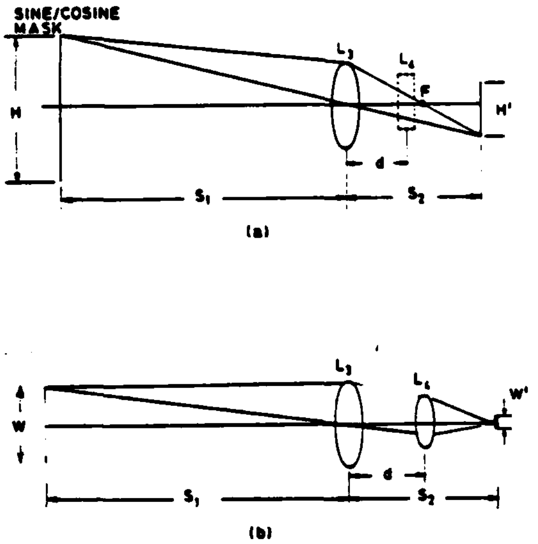

Fig. 13. Anamorphic optical system for use in the output part of Fig. 12.

4. Discussion and conclusions

Optical computing is inherently suited for processing of one dimensional or two dimensional signals. Optical processing of multi-dimensional signals becomes possible through the application of projection theorems. This paper demonstrates the utility of the projection-slice theorem stemming from the multi-dimensional Fourier transform in optical computing particularly in 3-D tomographic image reconstruction and display.

Two hybrid (opto-digital) processing schemes for true 3-D image reconstruction and display were described. Both schemes employ space-time multiplexing to display 3-D images tomographically in parallel slices. The space-time multiplex feature also allows considerable relaxation of the resolution capability of the recording device (photographic film for instance) used to store the projection hologram as compared to conventional holographic 3-D imaging.

In the one scheme employing coherent optical processing, a 3-D volumetric display, few centimeters cube in size, is demonstrated. Unaided viewing of the 3-D image is possible by several observers simultaneously. The fidelity of the retrieved 3-D image is found to be quite good despite the slight curvature of the oscillating projection surface. It is worth noting that the disc film format of the newly introduced Kodak Disc 4000 camera with its 15 circularly distributed exposure cites is perfectly suited for use as the hologram bearing wheel in this scheme. Replacement of the photographic storage used in this scheme by a fast recyclable spatial light modulator (SLM) would allow its use with a computer display of projection holograms directly to realize overall real-time operation.

The second scheme employing incoherent light has the advantage of being able to accept a color CRT or computer graphic video display as the input format directly. It performs the required 2-D Fourier transform of a projection hologram displayed by the computer as a series of one dimensional incoherent opto-electronic Fourier transforms through the use of a spatial domain projection theorem. The scheme can handle complex data by color coding. It can suppress the dynamic bias problem and has the potential for high throughput. For example the use of four self scanning detector arrays of 1024 elements each at 5MHz clock rate in this scheme would permit carrying out a complete 2-D complex Fourier transform of 100 radial lines each containing 612 frequency points in about 10 msec. This indicates a throughput of $6.12\ 10^4$ operations per msec which is about two order of magnitudes faster than a digital array processor. The required dove prism rotation rate then is 6000 RPM. The rotation period of the prism and the persistance of the color CRT display must however be matched.

Tradeoff between serial and parallel processing in the scheme of Fig. 12 is possible. This can be achieved by using N processors of the type shown in Fig. 12 to view the CRT display (or object scene) in parallel simultaneously with each processor handling a different set of the $180°/\Delta\theta$ radial lines of the fourier transform $F(\omega_x,\omega_y)$. This would have the advantage of reducing the processing time by a factor N.

To date characterization of the various parts of the scheme such as the image rotation subsystem, the integration and image spreading subsystem, and the sine/cosine masks has been completed. Evaluation of the output segment is underway. Overall performance evaluation is expected in the near future.

5. Acknowledgement

This work was sponsored in part by the Air Force Office of Scientific Research, Air Force Systems Command under Grant No. AFOSR-81-0240 and by the Army Research Office under Contract No. DAAG-29-K-0024.

References

1. E. Wolf, Optics Comm., Vol. 1, 153, Sept/Oct. 1969.
2. E. Wolf, J. Opt. Soc. Am., Vol. 60, 18-20, Jan. 1970.
3. R. Dandliker and K. Weiss, Optics Comm., Vol. 1, 323-328, Feb. 1970.
4. W.H. Carter, J. Opt. Soc. Am., Vol. 60, 306-314, March 1970.
5. W.H. Carter and P-C Ho., App. Optics, 13, 162-172, Jan. 1974.
6. A.J. Devany, J. Math. Phys., Vol. 19, 1526-1531, July 1979.
7. A.F. Fercher, et. al., Appl. Optics, Vol. 18, 2427-2439, July 1979.
8. A. Jain, App. Phys. Letters., Vol. 28, 451-453, April 1976.
9. R.M. Lewis, IEEE Trans. on Ant. and Prop., Vol. AP-17, 108-314, May 1969.
10. N. Bojarski, Report under contract B0019-73-C-0316, Naval Air Syst. Command, Feb., 1974.
11. IEEE Trans. on Ant. and Prop. - Special Issue on Inverse Methods in Electromagnetics, W. Boerner, A.K. Jordan and I. Kay (Eds.), Vol. AP-29, March 1981.
12. N.H. Farhat and C.K. Chan, in *Acoustical Imaging*, Vol. 8, A. Metherell (Eds.) Plenum Press, 499-515, New York (1980).
13. C.K. Chan and N.H. Farhat, IEEE Trans. on Ant. and Prop., Vol. AP-29, 312-319, March 1981.
14. G.W. Stroke and M. Halioua, Trans. Am., Cryst. Assoc., Vol. 12, 27-41, (1976).
15. W. Swindell and H. Barrett, Physics Today, Vol. 30, 32-41, Dec. 1977.
16. G. Baum and G.W. Stroke, Science, Vol. 189, 994-995, Sept. 1975.
17. D.L. Vickers, Lawrence Livermore Laboratory, Report No. UCID-17035, Feb. 1976.
18. T. Okoshi, *Three-Dimensional Imaging Techniques*, Academic Press (1976).
19. T. Okoshi, "Three-Dimensional Displays", Proc. IEEE, Vol. 68, 548-564, May 1980.
20. T. Walters and W. Harris, Byte, Vol. 3, 16-30, May 1978.
21. J. Radon, "Uber die Bestimmung von Funktionen durch ihre integralwerte langs gewisser Mannigfaltigkeiten", Ber. Saechs. Akad. Wiss. (Leipzig), Vol. 69, pp. 262-278, (1917)
22. R.N. Bracewell, Aust. J. of Phys., Vol. 9, 198-217, (1956).
23. R.N. Bracewell and S.J. Werneke, J. Opt. Soc. Am., Vol. 65, 1342-1346, Nov. 1975.
24. G. Stroke, et. al., Proc. IEEE, Vol. 65, 39-62, Jan. 1977.
25. R.M. Mersereau and A.V. Oppenheim, Proc. IEEE, Vol. 62, 1319-1338, Oct. 1974.
26. H.H. Barrett, Optics Letters, Vol. 7, June 1982, pp. 248-250.
27. H.H. Barrett, "Three-Dimensional Image Reconstruction from Planar Projections, with Applications to Optical Data Processing", in *Transformations in Optical Signal Processing*, W.T. Rhodes, J.R. Fienup and B.E.A. Saleh (Eds.). SPIE, Bellingsham 1982, (To be published).
28. H. Barrett, "The Radon Transform and its Applications", to be published in Progress in Optics.

388-19

29. N. Farhat, "High Resolution 3-D Tomographic Imaging by Wavelength and Polarization Diversity", University of Pennsylvania Proposal submitted to AFORS, May 14, 1981

30. N.H. Farhat and C-Yi Ho, in Optics in Four Dimensions, M.A. Machado and L.M. Narducci (Eds.). Am. Inst. of Phys., New York (1981), 341-354.

31. P.R. Bradley-Moore and E.A. Woloshue, Strobosopic Analyzing Monitor, Zyntrax Corp. Report, 135 East 65th St., New York, NY 10021.

32. J.M. Richardson, "Device for Producing Identifiable Sine and Cosine (Fourier) Transforms of Input Signals by Means of Noncoherent Optics", U.S. Patent 3,669,528, June 1972.

33. G.L. Rogers, *Noncoherent Optical Processing*, J. Wiley & Sons, London (1977).

34. G.M. Morris, App. Optics, Vol. 20, 2017-2024, June 1981.

35. J. Goodman and L.M. Woody, App., Opt., Vol. 16, 2611-2612, 1977.

36. J. Goodman, et. al., Optics Letters, Vol. 1, 1978.

37. K. Bromely et. al., "Incoherent Optical Signal Processing Using Charge Coupled Devices (CCD's)", in *Optical Signal and Image Processing*, SPIE, Vol. 118, pp. 118-123, 1977.

38. A.R. Dias, "Incoherent Matrix-Vector Multiplication for High Speed Data Processing", Stanford Electronics Laboratory, Stanford University Technical Report No. L722-4., June 1980.

39. J. Goodman and K. Johnson, "Optical Computing Research", Stanford Electronics Laboratory, Stanford University Technical Report No. L722--6, March, 1981.

40. P. Wiersma, Optics Comm., Vol. 28, 280-282, March, 1979.

41. Y. Das and W.M. Boerner, IEEE Trans. on Ant. and Prop., Vol. AP-26, pp. 274-379, March, 1978.

42. H.J. Whitehouse, "The Role of Charge Coupled Devices and Surface Acoustic Wave Devices in Optical Signal Processing", SPIE, Vol. 118, 1977, pp. 124-131.

Appendix 1

The projection-slice theorem

Let $\gamma(\bar{r})$ and $\Gamma(\bar{p})$ be a Fourier transform pair representing a 3-D object function and its 3-D Fourier transform respectively, i.e.,

$$\Gamma(\bar{p}) = \int_v \gamma(\bar{r})\, e^{-j\bar{p}\cdot\bar{r}}\, d\bar{r} \qquad \text{(A-1)}$$

where v defines the object extent and

$$\gamma(\bar{r}) = \frac{1}{(2\pi)^3} \int \Gamma(\bar{p})\, e^{j\bar{p}\cdot\bar{r}}\, d\bar{p} \qquad \text{(A-2)}$$

where working in cartesian coordinates $\bar{r} = x\,\bar{I}_x + y\,\bar{I}_y + z\,\bar{I}_z$ and $\bar{p} = p_x\,\bar{I}_x + p_y\,\bar{I}_y + p_z\,\bar{I}_z$ are position vectors in object space and Fourier space respectively with $d\bar{r}$ and $d\bar{p}$ being differential elements in $\bar{r}$-space and $\bar{p}$-space.

The projection of $\Gamma(\bar{p})$ on a given plane, for example the $p_x - p_y$ plane, is

$$\Gamma_{proj.}(p_x,p_y) = \int_{p_z} \Gamma(p_x,p_y,p_z,)\, dp_z \qquad \text{(A-3)}$$

Substituting (A-1) in (A-3), we obtain

$$\Gamma_{proj.}(p_x,p_y) = \iiint \gamma\,(x,y,z):\int e^{-j(p_x x + p_y y + p_z z)} dp_z)\, dx\, dy\, dz \qquad \text{(A-4)}$$

If the extent of $\Gamma(\bar{p})$ is sufficiently large the integration of the exponential $e^{-jp_z z}$ with respect to p_z yields approximately a delta function $\delta(z)$ leading to,

$$\Gamma_{proj.}(p_x,p_y) = \iiint_{xyz} \gamma(x,y,z)\,\delta(z)\, e^{-j(p_x x + p_y y)}\, dx\, dy\, dz$$

$$= \iint_{xy} \gamma(x,y)\, e^{-j(p_x x - p_y y)}\, dx\, dy. \qquad \text{(A-5)}$$

where $\gamma(x,y)$ is a central slice through the object $\gamma(\bar{r})$ parallel to the $p_x - p_y$ plane.

It follows from eq. (A-5) by the inverse transform that

$$\gamma(x,y) = \frac{1}{(2\pi)^2} \int_{p_x}\int_{p_y} \Gamma_{proj.}(p_x,p_y)\, e^{j(p_x x + p_y y)}\, dp_x dp_y \qquad \text{(A-6)}$$

which is one form of the required theorem. Accordingly, the projection of the 3-D transform data on a given plane is the Fourier transform of a central or meridional slice through the object oriented parallel to the particular projection plane.

Fourier transform relationships between parallel projections and parallel slices can be obtained by invoking the concept of *weighted projection*. For example let $\Gamma^{\alpha}_{proj.}(p_x,p_y)$ be the weighted projection of $\Gamma(\bar{p})$ defined as,

$$\Gamma^{\alpha}_{proj.}(p_x,p_y) = \int_{p_z} \Gamma(p_x,p_y,p_z)\, e^{j\alpha p_z}\, dp_z \tag{A-7}$$

where α ia a real weighting parameter. Substituting for Γ from eq. (A-4) yields,

$$\Gamma^{\alpha}_{proj.}(p_x,p_y) = \int_{p_z} e^{j\alpha p_z} \int_x \int_y \int_z \gamma(x,y,z)\, e^{-j(p_x x + p_y y + p_z z)}\, dx\, dy\, dz\, dp_z \tag{A-8}$$

Carrying out the integration with respect to p_z first while assuming the extent of $\Gamma(\bar{p})$ in the p_z direction is sufficiently large, the integral with respect to p_z may be approximated by $\delta(z-\alpha)$. Equation (A-8) can then be reduced to,

$$\Gamma^{\alpha}_{proj.}(p_x,p_y) = \int_x \int_y U(x,y,z=\alpha)\, e^{-j(p_x x + p_y y)}\, dx\, dy \tag{A-9}$$

which says that $\Gamma^{\alpha}_{proj.}(p_x,p_y)$ and $\gamma(x,y,z=\alpha)$ are two dimensional Fourier transform pairs. The weighted Fourier domain projection theorem follows from the inverse transform

$$\gamma(x,y,z=\alpha) = \frac{1}{(2\pi)^2} \int_{p_x} \int_{p_y} \Gamma^{\alpha}_{proj.}(p_x,p_y)\, e^{j(p_x x + p_y y)}\, dp_x\, dp_y \tag{A-10}$$

Accordingly parallel slices of the object can be reconstructed from the weighted projection $\Gamma^{\alpha}_{proj.}(p_x,p_y)$ computed for different values of the weighting parameter α.

Because of the symmetrical nature of the Fourier transform the above treatment can be repeated by starting with projections in object space rather than projections in Fourier space to show that projections of $\gamma(\bar{r})$ and slices of $\Gamma(\bar{p})$ form Fourier pairs.

Finally it is worth noting that 2-D projections in Fourier space can be regarded as proposed in [14] and [21] as *projection holograms*.